Estimation of Path Delays, TEC and Faraday Rotation from SAR Data

Dissertation

zur

Erlangung der naturwissenschaftlichen Doktorwürde
(Dr. sc. nat.)

vorgelegt der

Mathematisch-naturwissenschaftlichen Fakultät

der

Universität Zürich

von

Michael Jehle

aus

Deutschland

Promotionskomitee

Prof. Dr. Michael Schaepman (Vorsitz)
Prof. Dr. Alain Geiger
Prof. Dr. Robert Weibel
Dr. Erich Meier
Dr. David Small

Zürich, 2009

Mathematisch-naturwissenschaftliche Fakultät
der Universität Zürich

Dissertation
Estimation of Path Delays, TEC and Faraday Rotation from SAR Data

Author

Michael Jehle
Remote Sensing Laboratories
Department of Geography
University of Zurich
Winterthurerstrasse 190
CH-8057 Zurich
Switzerland

`http://www.rsl.ch`

Prepared with $\LaTeX\,2_\varepsilon$

To my parents

Abstract — Spaceborne synthetic aperture radar (SAR) systems are used to measure geo- and biophysical parameters of the Earth's surface, e.g. for agriculture, forestry and land subsidence investigations. Recently launched and upcoming spaceborne SAR satellites continue the trend of measuring these parameters on a global scale from space with continually higher accuracies. Larger frequency modulated chirp bandwidths and increased spatial resolution allow for new and additional information with higher geometric resolution. One dares to hope that in the near future space borne radar remote sensing will be the able to contribute to monitoring for earthquake precursors. The use of large bandwidths, however, causes signal degradation within the ionosphere. Under high solar activity conditions and at low carrier signal frequency, ionosphere-induced path delays and Faraday rotation (FR) become significant for SAR applications. The influence of the troposphere becomes relevant given geolocation accuracy requirements of less than 1 m as obtained e.g. with TerraSAR-X by the German Aerospace Center (DLR).

By means of an in-depth analysis from radar signal propagation through the atmosphere and within a standard SAR system model, this dissertation shows possibilities for measuring, extracting and correcting propagation effects of the two layers most relevant to accurate spaceborne SAR measurement: the troposphere and ionosphere. In order to test and crosscheck both measurements and models, data obtained from TerraSAR-X along with differential GPS position measurements of corner reflectors (CR) at different altitudes were processed for the tropospheric investigations. Measured data from the Japanese Phased Array L-band Synthetic Aperture Radar (PALSAR), onboard the Advanced Land Observing Satellite (ALOS), and simulated data from a potential P-band system were used to examine and simulate the ionospheric effects and to establish space borne methods for the extraction of ionospheric total electron content (TEC) and FR from SAR data. Concluding propositions evaluate possible SAR sensor and signal modifications to facilitate corrections.

Zusammenfassung — Weltraumgestützte Radarsysteme mit synthetischer Apertur (SAR) werden zur Messung von geo- und biophysikalischen Parametern auf der Erde benutzt. Beispiele dafür sind die Beobachtung der Erdkruste oder die Messung von Oberflächenveränderungen im agrar- und forstwirtschaftlichen Bereich. Kürzlich gestartete sowie in naher Zukunft geplante Sensoren zeigen einen Trend in Richtung globaler Messung dieser Parameter vom Weltraum aus. Mit immer höheren Bandbreiten versucht man zusätzliche Informationen und Verbesserungen in der geometrischen Auflösung zu erhalten. Man hofft sogar, in Zukunft mittels der Radarfernerkundung einen Beitrag zur Früherkennung von Erbeben leisten zu können. Große Bandbreiten führen jedoch innerhalb dispersiver Medien wie der Ionospähre zu einer Signalverschlechterung. Bei hoher Sonnenaktivität und niedrigen Frequenzen können ionosphärische Effekte wie Laufzeitverzögerungen und Faraday Rotation (FR) für SAR Anwendungen kritisch werden. Der Einfluss der Troposphäre muss berücksichtigt werden, wenn Lokalisierungsgenaugkeiten von unter einem Meter gefordert sind, wie das beispielsweise bei Produkten von TerraSAR-X des Deutschen Zentrums für Luft- und Raumfahrt (DLR) der Fall ist.

Diese Dissertation zeigt Möglichkeiten zur Messung, Extraktion und Korrektur von Ausbreitungseffekten in den für weltraumgestützte SAR Anwendungen massgebenden Schichten der Atmosphäre, der Troposhäre und der Ionosphäre. Die Grundlage dafür bilden eine ausführliche Analyse der Ausbreitung von Radarsignalen durch diese Medien und ein Standard SAR Modell. Um sowohl die Messungen als auch ein Modell bezüglich der Troposphäre zu testen und zu verifizieren, wurden TerraSAR-X Daten zusammen mit differentiellen GPS Messungen von Corner Reflektoren (CR) in verschiedenen Höhenlagen ausgewertet. Zur Extraktion des Elektronengehaltes der Ionosphäre (TEC) und der FR aus SAR Daten und zur Simulation ionosphärischer Effekte und Methoden wurden reale Daten des japanischen Phased Array L-band Synthetic Aperture Radar (PALSAR) an Bord des Advanced Land Observing Satellite (ALOS) und simulierte Daten eines potentiellen weltraumgestützten P-band SAR Systems verwendet. Dazu werden Vorschläge hinsichtlich einer einfachen SAR Sensor - und Signalmodifikation ausgearbeitet und zusammenfassend evaluiert.

Foreword

The dissertation at hand started out of the blue. What began as a one year research project of tropospheric and ionospheric influences on geometric errors of synthetic aperture radar — a work starting with electrons and trying to reach outer space — gave way to the evolution of this dissertation. The inherent atmosphere thereby was the Remote Sensing Laboratories at the University of Zurich.

However, the initial project soon reached a higher energy level when I realized the potential of regarding the ionosphere not as a sinister foe to radar signals but as a powerful friend. The understanding of interaction between radar waves and ionosphere allows the measurement of electron content, the explanation of polarimetric distortion, and its exploitation towards sharper radar images. From this arises better polarimetric object categorization, measurement of the earth's magnetic field, and possibly — as some dare to hope — even prediction of earthquakes and tsunamis.

Accurate radar signal processing combined with classical and quantum physical effects is interdisciplinary and requires bounds and constants to limit such a project to healthy levels avoiding a high rate of ionization. Such a constant was Erich Meier. He offered my ideas an orbit at the SARLab and provided a stable environment to my electrons with interesting research questions and access to data from the most sophisticated radar satellites available. Together, we thought of intensive simulations and extensive experimental setups.

A second constant I discovered early on was the Daniel Nüesch coefficient. He acted as both an advisor and a driver to this dissertation. When my electrons threatened to lose spin, he lashed them on again. When a photon was bringing light to a problem, he was there to celebrate.

Close-bound project details were governed by the Dave Small factor, guiding me with many helpful hints and advice, while the universitarian laws of nature were overseen by Klaus Itten, accepting me as his doctoral student. When Klaus Itten handed the sceptre to Michael Schaepman while I was on the home stretch, both granted me an interference-free dusk orbit. Together, they set the limits wherein this dissertation could grow and reach its full potential.

To fully describe the processes and developments this dissertation has seen, perturbation theory is needed. I choose to describe it as the SARLab effect — an environment of individuals highly curious and strongly free-spirited, working together in an atmosphere of mutual helping and an ionosphere of academic freedom. Whether during scientific discussions or immature jokes, we were spinning at a strong momentum. On the various electron shells, there were Maurizio, Oti, Felix, Dani as well as Christophe, Jörg, Max, Noldi, Schubi and Zubi. In the department, much appreciated atomic links existed to Dubingo and Ben. Total electron content and monetary support was provided by armasuisse and its researchers Peter Wellig and Konrad Schmid, while the complete ionosphere was only held together by cooperation with fellow scientists across the world as well as many unknown or unidentified molecules.

Finally, I would like to mention my atomic nucleus, those closest to me, who kept with me at all times. You know who you are.

Zürich, April 2009

Contents

Chapter 1

Introduction

This dissertation aims to contribute to atmospheric research in combination with radar remote sensing applications. Global observation and measurement of atmospheric parameters help understanding of geophysical processes. A major problem, for example in assessing the global carbon cycle, is the state of understanding of the terrestrial ecosystem. Improvements to understanding are expected in the future from measuring the change of the Earth's biomass in a time series.

One way to possibly measure biomass on a global scale is by Earth observation with satellites. Good estimates of forest biomass can be obtained from synthetic aperture radar (SAR) at lower frequencies [1]. However, the performance of a spaceborne SAR system is often significantly degraded by the effects of the atmosphere. In order to avoid these problems, model, or better yet correct them, it is necessary to estimate the atmospheric state before or during a data take. Methods enabling measurement of the most relevant atmospheric parameters are the subject of this work.

The introduction is meant to provide background knowledge to round out the journal contributions that follow in Chapters 2 to 4. Therefore, it does not claim to entirely cover all propagation effects in the atmosphere. Continuative directions for a more complete overview of atmospheric effects are given in the references listed at the end of each chapter.

1.1 Electromagnetic Wave Propagation and SAR

Operational synthetic aperture radar processing usually does not include consideration and handling of propagation effects caused by atmospheric layers. The recently launched Advanced Land Observing Satellite (ALOS) satellite with the on-board Japanese Phased Array L-band Synthetic Aperture Radar (PALSAR) instrument or the TerraSAR-X (TSX) sensor as well as up-coming sensors show the trend to high-bandwidth or high-resolution SAR systems in space. Atmospheric effects that were negligible earlier become relevant with their increased accuracy requirements.

This chapter deals with the principal basics to derive and correct propagation effects like path delay, Faraday rotation (FR), and ray bending in media like the atmosphere. Estimation of path delays, FR, and ray bending through the atmosphere requires knowledge of the refractive index n of the media in order to assess the propagation velocity and - paths which differ from free space propagation. The most significant propagation effects on radar remote sensing of the Earth are caused mainly by the ionosphere and the troposphere. The derivation of the refractive index for both parts of the atmosphere is based on different physical characteristics and will be discussed in separate chapters.

After a general introduction to the atmosphere, electromagnetic wave propagation therein, derivation of the refractive index, and models that can be used for a simulation of these effects are outlined. Other major propagation effects like attenuation and noise sources are shortly summarized at the end of the chapter.

1.2 Structure of the Atmosphere

Electromagnetic waves propagating through the atmosphere experience modification of their signal velocity and direction. The extent of these delays depends on the characteristics of the atmosphere's layer. In general, the atmospheric layers can be divided into troposphere, stratosphere, mesosphere and ionosphere. The following exosphere forms the transition to outer space and the magnetosphere keeps the ionised gases located around the Earth.

Fig. 1.1a) and b) illustrate the location and some characteristics of the most important layers. The troposphere is the lowest part of the atmosphere and stretches up to a height of about 11 km. The local temperature in the troposphere decreases nearly linearly at a rate of 6.5° C per kilometer to a minimum of about -50° C. Following the troposphere, the stratosphere extends to an altitude of about 50 km where the temperature rises to +50° C. In the mesosphere, at heights between 50 and 80 km, the temperature decreases to about -120° C followed by the thermosphere where temperature climbs to upward of +1500° C. These spheres are all mainly characterised by their temperature behavior.

The area where the *ionosphere* is located is at heights between 80 and 1200 km and is characterised by the number of ionised electrons. The number of free electrons interacting with the traversing signal causes a path delay that depends on the signal's frequency. Frequencies below a critical frequency (cut-off frequency) are, as illustrated in Fig. 1.1a), reflected. The cut-off frequency depends mainly on the density of the ionospheric layers present. Usually, the cut-off frequency is around 30 MHz. This behavior is used by ionospheric radar sounders for tomographic measurements of the lower ionosphere. Data transfer applications use this effect for long distance communications where the radio wave travels in zig-zag form between the Earth's surface and the ionosphere.

Topside sounding of the ionosphere is done by satellites [2]. Frequencies above the cut-off traverse the ionosphere and experience path delays that progressively decrease in magnitude at higher frequencies. This frequency dependent (dispersive) behavior is measured by dual-frequency receivers of the Global Positioning System (GPS) to correct path

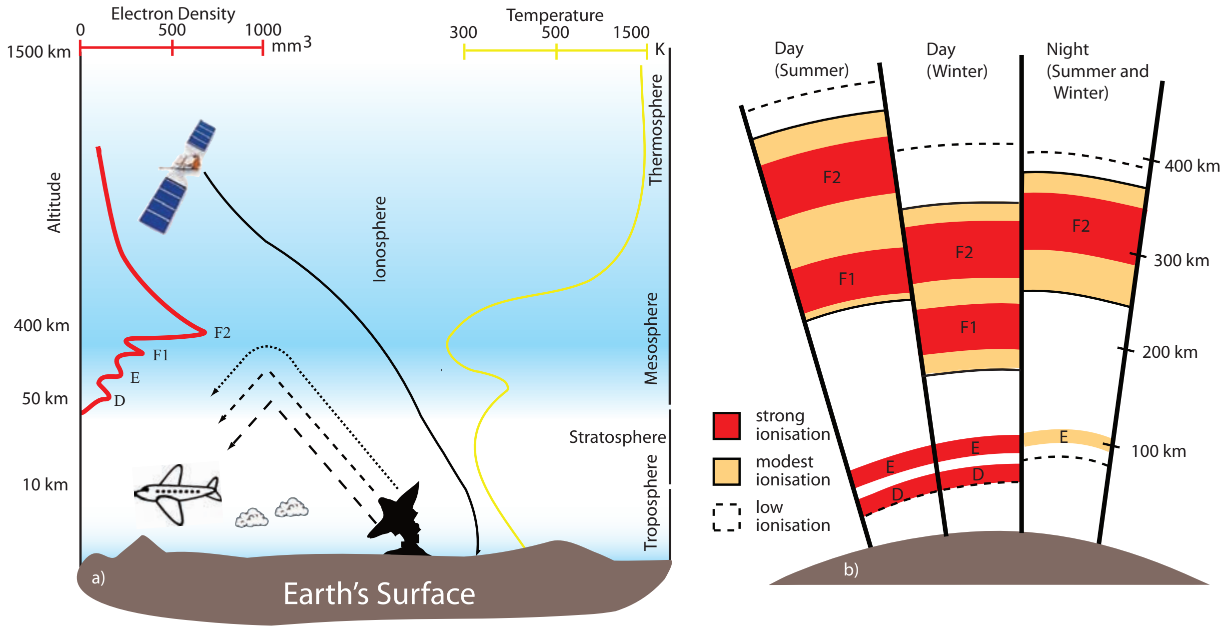

Figure 1.1: Structure of the atmosphere. a) Structure and wave propagation through the atmosphere, b) distribution and density of ionospheric layers during a day and the seasons, modified from [2].

delays and also map global total electron content (TEC) [3]. Due to the inhomogeneity of the layers, the ionosphere is subdivided into the layers D, E, F1, and F2. The layers are successively named and located according to their daytime electron density status. Maximum electron density is in the layer closest to the sun, the F2 layer. At night, the lower D and E layers can completely disappear due to recombination of electrons and ions [4]. Additionally, differences between seasons can be observed. Fig. 1.1b) illustrates this behavior. The following chapters focus on the troposphere and ionosphere, as these layers are most relevant for spaceborne radar applications.

1.3 Waves in Media

Electromagnetic waves propagating through nonconducting media can be described by Maxwell's field equations which formulate the generation of electric and magnetic fields by electric charges and currents and their interactions [5]. They are used to describe the macroscopic behavior of time- and location-dependent fields in dielectric media like the atmosphere. Maxwell's equations are fundamental to retrieval of the refractive index of the atmospheric layers, the radar wave propagation velocity, and the polarisation rotation. The complete set of equations within a continuous medium is listed in Appendix A.1.

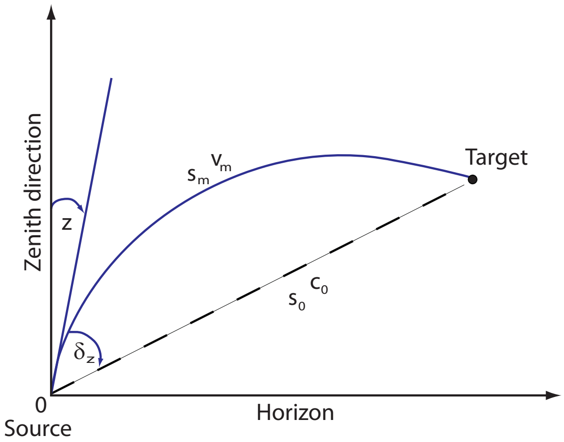

Figure 1.2: Estimation of path delay in the atmosphere. s_0 *describes propagation at vacuum conditions and* s_m *within a medium having refractive index* n*.* δ_z *describes the effects of refraction on the zenith angle* z*.*

1.3.1 Refractive Index

The propagation path of electromagnetic waves in media can also be described by Fermat's principle [6]. A radio wave propagates on the path s that results in a minimal run-time

$$\Delta t = \min \int_{path} dt = \int_{path} \frac{ds}{v} = \min. \tag{1.1}$$

The propagation velocity v can be calculated from

$$v = \frac{c_0}{n} \tag{1.2}$$

where c_0 is the speed of light in vacuum. Using 4.2 in 1.1 produces

$$\Delta t_0 = \frac{1}{c_0} \int_{path} n\, ds = \min. \tag{1.3}$$

Using 1.3, the difference between the propagation path length s_0 in vacuum and the propagation path in a medium s_m caused by refraction can be estimated by multiplying their run-times t_m, t_0 with the vacuum speed and subsequent subtraction. Fig. 1.2 illustrates this situation (for $n = 1$ the path goes directly from 0 to the target). There are two contributions to the path delay. The larger distance the radar waves travels is caused by ray bending, while a further delay is caused by a lower propagation speed. These two contributions are expressed in [6]

$$\begin{aligned} \Delta s &= s_m - s_0 = c_0 \Delta t_m - c_0 \Delta t_0 = \int_{path} n\, ds - \int_0^s ds = \\ &= \underbrace{\int_0^s (n-1)\, ds}_{\Delta \text{ path caused by } \Delta \text{ run-time}} + \underbrace{\left(\int_{path} n\, ds - \int_0^s n\, ds \right)}_{\Delta\text{path caused by ray bending}}, \end{aligned} \tag{1.4}$$

where the first term on the right side of the second line describes the path delay contribution caused by the run-time delay and the second term the contribution caused by ray bending. Estimation of ray bending caused by refraction can be derived using Snell's law and its derivation

$$n \sin z = \text{const.} \tag{1.5}$$

$$\sin z \, dn + n \cos z \, dz = 0. \tag{1.6}$$

where z describes the zenith angle. Using the simplifications $n \approx 1, z \approx 90°$, horizontal refraction $\approx$ 0 and ray bending on a circular path, the angle of refraction δ_z in Fig. 1.2 can be approximated [6] by

$$\delta_z = \frac{k_n}{2R} s, \tag{1.7}$$

where R is the radius of the Earth, $k_n = -R\frac{dn}{dh}$ is the refraction coefficient and h the height of the source. More details on the theory of refraction and ray bending within the atmosphere can be found in [6], [7].

1.3.2 Phase Velocity, Group Velocity and Front Velocity

Spaceborne imaging radar systems used in remote sensing transmit modulated pulses to improve resolution in range at a manageable peak power. The most commonly used method is a linear frequency modulation of the pulse referred to as a chirp. In vacuum, each frequency within the chirp travels at the same speed. Under ionospheric conditions, propagation of the chirp pulse is dependent on the frequency. The propagation speed of the pulse can then be described by the velocities:

front velocity v_{front}: describes the velocity of the travelling wave front (areas of identical amplitudes)

$$v_{\text{front}} = \lim_{k \to \infty} \frac{\omega(k)}{dk},$$

phase velocity v_{phase}: describes the velocity of a constant phase within the pulse

$$v_{\text{phase}} = \frac{\omega}{k},$$

group velocity v_{group}: describes the velocity the envelope of the pulse travels

$$v_{\text{group}} = \frac{d\omega}{dk},$$

where k is the wave number and ω the angular frequency. For illustration, Fig. 1.3 shows a monochromatic wave under regular dispersive conditions $\left(\frac{dv}{d\lambda} > 0\right)$, comparable to the situation in the ionosphere. λ denotes the wavelength of the radar pulse. The red point

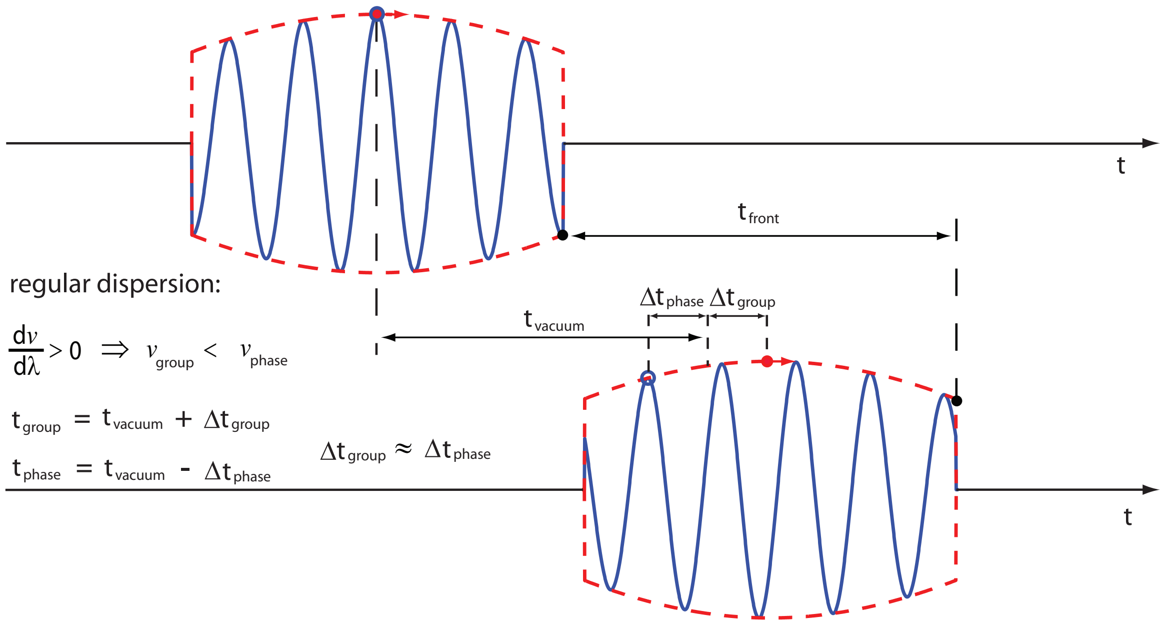

Figure 1.3: Illustration of front, group and phase velocity under regular dispersive conditions for a monochromatic pulse. Information travels with the speed of the envelope. t_{front}*,* t_{phase}*,* t_{group}*, and* t_{vacuum} *denote the runtime of the wave front, phase, its envelope, and under vacuum conditions respectively. Time differences between vacuum propagation and the phase or group delay are denoted* Δt_{phase} *and* Δt_{group} *respectively.*

marks the group velocity and is defined to be at the center of the envelope. The phase velocity, illustrated by the blue circle, returns faster to the state of constant phase compared to vacuum propagation and the propagation of the envelope. For a monochromatic wave, the front velocity corresponds to the group velocity. For a linear frequency modulated pulse, the front velocity depends on the chirp bandwidth and form. This behavior is discussed in Chapter 4 in greater detail.

1.3.3 Ionosphere

The ionosphere is characterized by the existence of free electrons and ions that define the refractive index in this area. Ionisation is caused mainly by solar ultra violet (UV) radiation and X-rays. Therefore, the degree of ionisation varies with local time and solar activity. Fig. 1.4a) shows a typical progression of the daily TEC in winter (for Hailsham in Europe). In 1.4b) an example of a global ionospheric map (GIM) is shown. TEC specifies the number of free electrons in a column of 1 m^2 along the measurement path. TEC units (TECU) are 10^{16} electrons per m^2. Maximum TEC values are usually measured around the geomagnetic equator between 12:00 and 16:00 local time. TEC levels at solar maximum can rise to over 150 TECU. The daily curve progression in summer does not normally have such a distinct maximum. The higher O_2/N_2 concentration in winter could

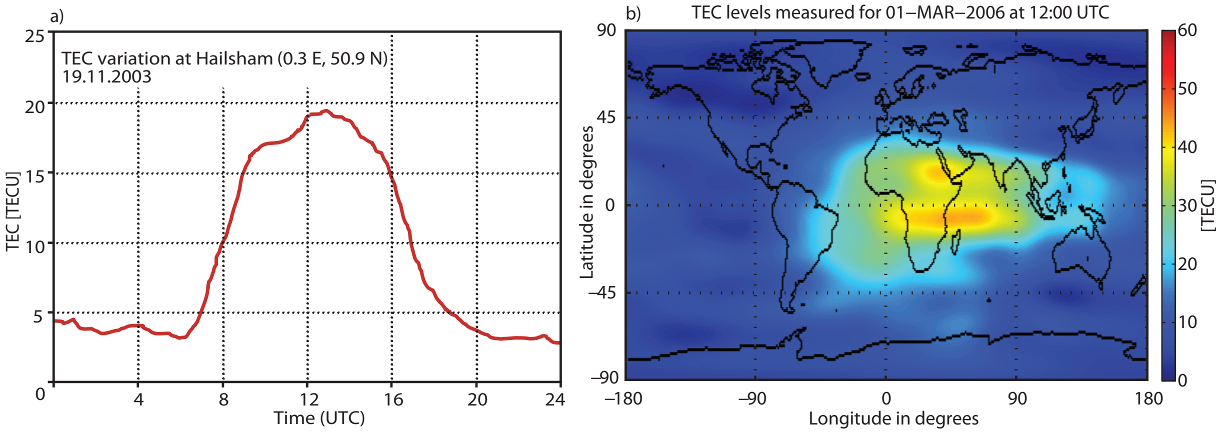

Figure 1.4: Typical progression of a) daily TEC measured at Hailsham, UK on November 2003 and b) global ionospheric TEC map measured on March 2006.

be one reason. More details on possible mechanisms for seasonal variations can be found in [8, 9]. Fig. 1.4b) shows a snapshot at 12:00 UTC in March 2006. Although 2006 was near the minimum of the solar cycle, TEC levels adjacent to the geomagnetic equator rose up to 45 TECU. The notably lower TEC values along the geomagnetic equator itself are a typical observation called equatorial ionisation anomaly (EIA). EIA is a result of a vertical $\vec{E} \times \vec{B}$ drift of ionised electrons in the F-layer followed by a downward diffusion in northern and southern directions along the geomagnetic field (fountain effect). This effect causes regions of higher ionisation at latitudes $\approx \pm 17^\circ$ adjacent to the geomagnetic equator [10–13].

A good indicator for the solar activity is the sunspot number or the solar flux, measuring the solar radio field intensity at the wavelength 10.7 cm (2800 MHz). Fig. 1.5 shows the statistics of sunspot numbers over the last 50 years. The 11-year solar cycle is clearly visible. At the end of 2007, the change from solar cycle number 23 to 24 began. Prediction of future solar cycles is a research topic in its own right. Current estimates predict that solar cycle 24 will be 30% – 50% higher than solar cycle 23 [14]. Spectral analysis of sunspot number time series showed repeating frequencies of 80 years, 22 years, 11 years and 27 days which are caused by the solar rotation [21]. Another typical observation is that the rise time is shorter than the time from solar maximum to solar minimum. A more accurate method for solar activity prediction than counting sunspot numbers is the measurement of UV- and X-ray emissions from the sun. These parameters are usually used by ionospheric models to predict TEC levels in the near future. Not visible in the above figures but also of importance for e.g. GPS measurements are ionospheric scintillation effects that mainly arise from electron density fluctuations in the E and F region or in the solar wind. Other anomalies are reported e.g. 5 days prior to an earthquake [17]. These anomalies also refer to changes in the Earth's magnetic field [18]. Current SAR systems are not sensitive to those magnetic field variations.

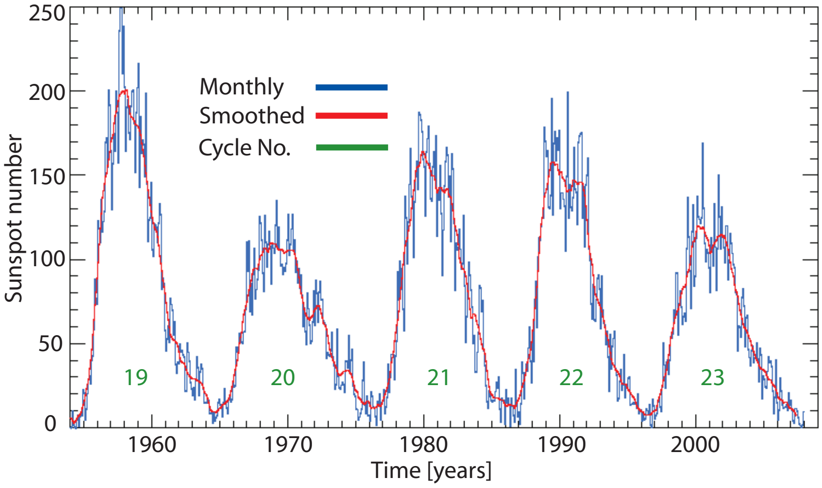

Figure 1.5: Sunspot numbers and maximum TEC values, modified from [16].

Time series of TEC measurements showed that TEC is mainly affected by the periodicity due to the

- solar cycle
- annual variation
- semi annual variation
- lunation cycle
- diurnal variations [21].

Measured global TEC maps are obtained operationally from a global network of over 200 GPS stations. The center for orbit determination in Europe (CODE) generates global TEC maps on a bi-hourly basis. These values have been collected since 1995 and can be downloaded in the IONosphere map EXchange (IONEX) format from the University of Berne [19]. TEC levels are estimated in 0.1 TECU for a vertical line of sight relative to the Earth's surface at a grid spacing of 5° in longitude and 2.5° in latitude. Figure 1.6 juxtaposes yearly TEC maxima and mean TEC with corresponding sunspot numbers. The mean annual maximum took place during 2002, corresponding to the saddle of maximum TEC in 2002. Comparing the mean sunspot numbers to mean TEC at the solar maximum in 2000 shows a ratio of 4.1. The ratio in the other years decreases to 3. Fig. 1.7 to Fig. 1.8 show the yearly mean TEC levels for 1996 to 2007 at 12:00 UTC over a complete solar cycle. One can see how the maximum TEC rises at the equator in the years 2000 to 2002 from 30 TECU to over 150 TECU. Low-frequency radar remote sensing in these areas and under these conditions could experience a complete signal loss. For an in-depth study on TEC statistics the reader is referred to [20, 21].

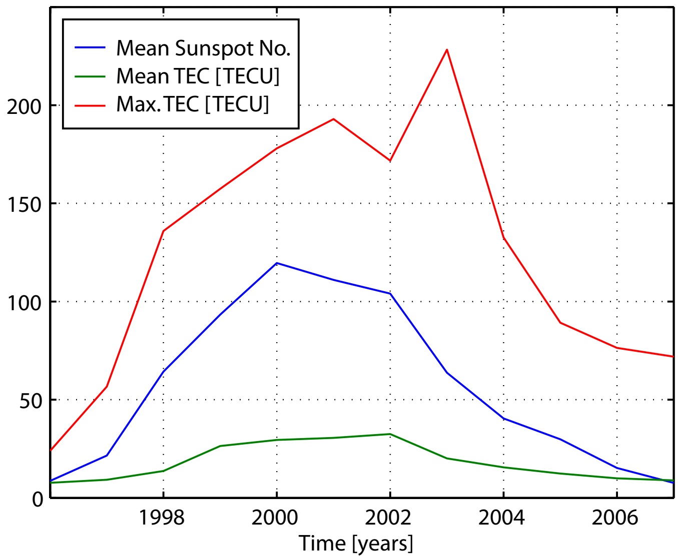

Figure 1.6: Mean sunspot numbers and corresponding TEC values

1.3.3.1 Refractive Index of the Ionosphere

To derive the refractive index, the results of the equation of motion of an electron are compared with Maxwell's equations. The results within the medium are derived for each component of the electric field and can be solved for the refractive index. Within the influence of the Earth's magnetic field, the ionosphere can be treated as an anisotropic medium resulting in birefringent propagation of radar waves. Under these conditions, a starting point for the estimation of the refractive index in the ionosphere according to [21] is the equation of motion of an electron. The equation of motion in this case is composed of contributions from the Coulomb force, the Lorentz force and the frictional force induced by the collision of electrons and heavy particles. After some conversions and simplifications, the equation of motion results in the Appleton-Hartree equation [21, 22]

$$n^2 = 1 - \frac{X}{(1-jZ) - \frac{Y_T^2}{2(1-X-jZ)} \pm \left[\frac{Y_T^4}{4(1-X-jZ)^2} + Y_L^2\right]^{1/2}} \tag{1.8}$$

where

$$\begin{aligned} X &= \frac{\omega_N^2}{\omega^2}, \quad Y = \frac{\omega_H}{\omega}, \quad Z = \frac{\nu}{\omega} \\ Y_L &= \frac{\omega_L}{\omega}, \quad Y_T = \frac{\omega_T}{\omega}. \end{aligned} \tag{1.9}$$

ω_N is the angular plasma frequency, ν the electron collision frequency, ω_L and ω_T are the longitudinal and the transverse components of the angular gyrofrequency of the magnetic field. More details on the conversions and simplifications in order to derive the Appleton-Hartree equation are provided in Appendix A.2.

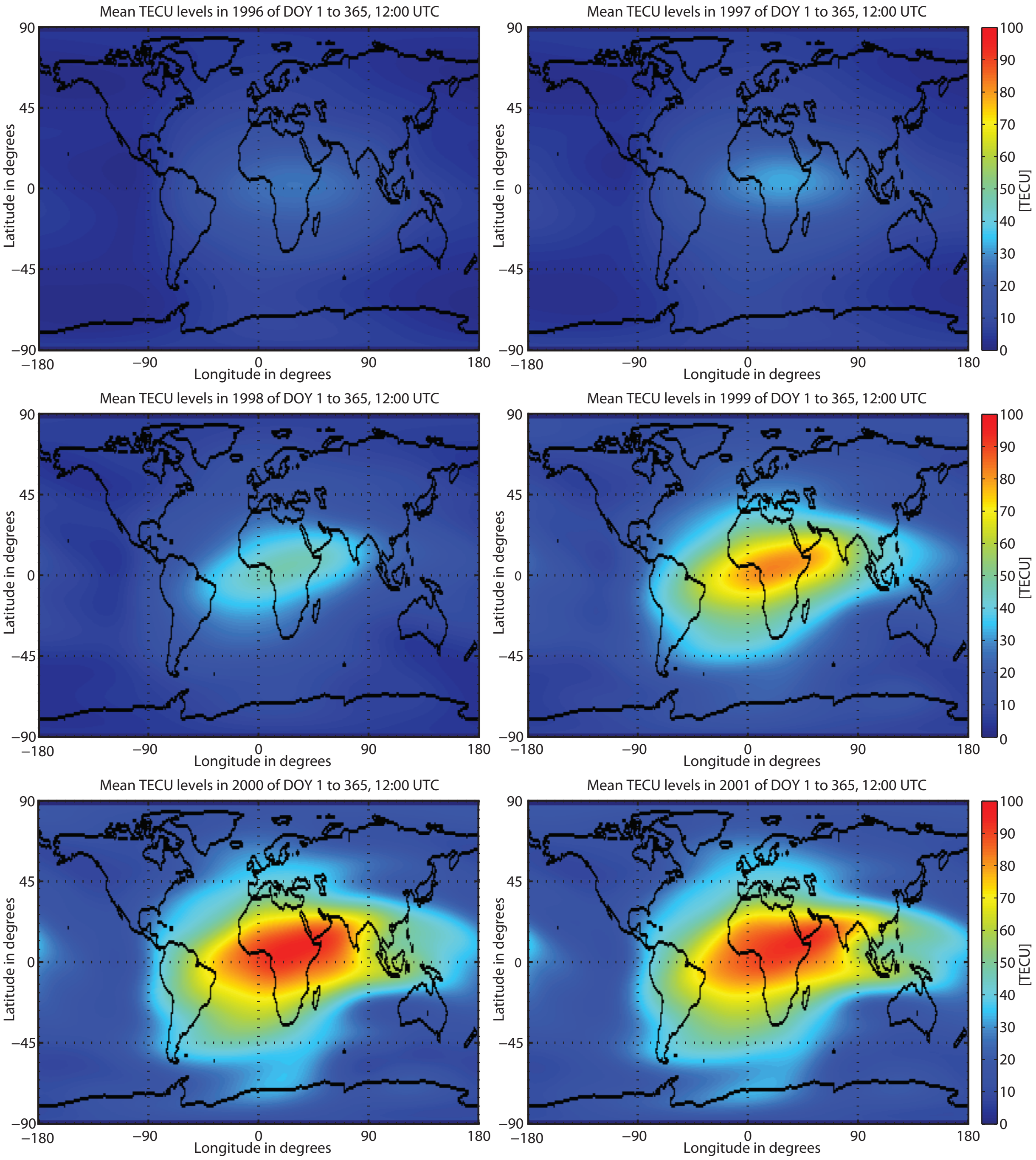

Figure 1.7: First half of complete 11-year solar cycle.

1.3.3.2 Ionospheric Path Delay

The Appleton-Hartree equation approximates the refractive index of the ionosphere. The refractive index is used to estimate ionospheric path delays in comparison to vacuum

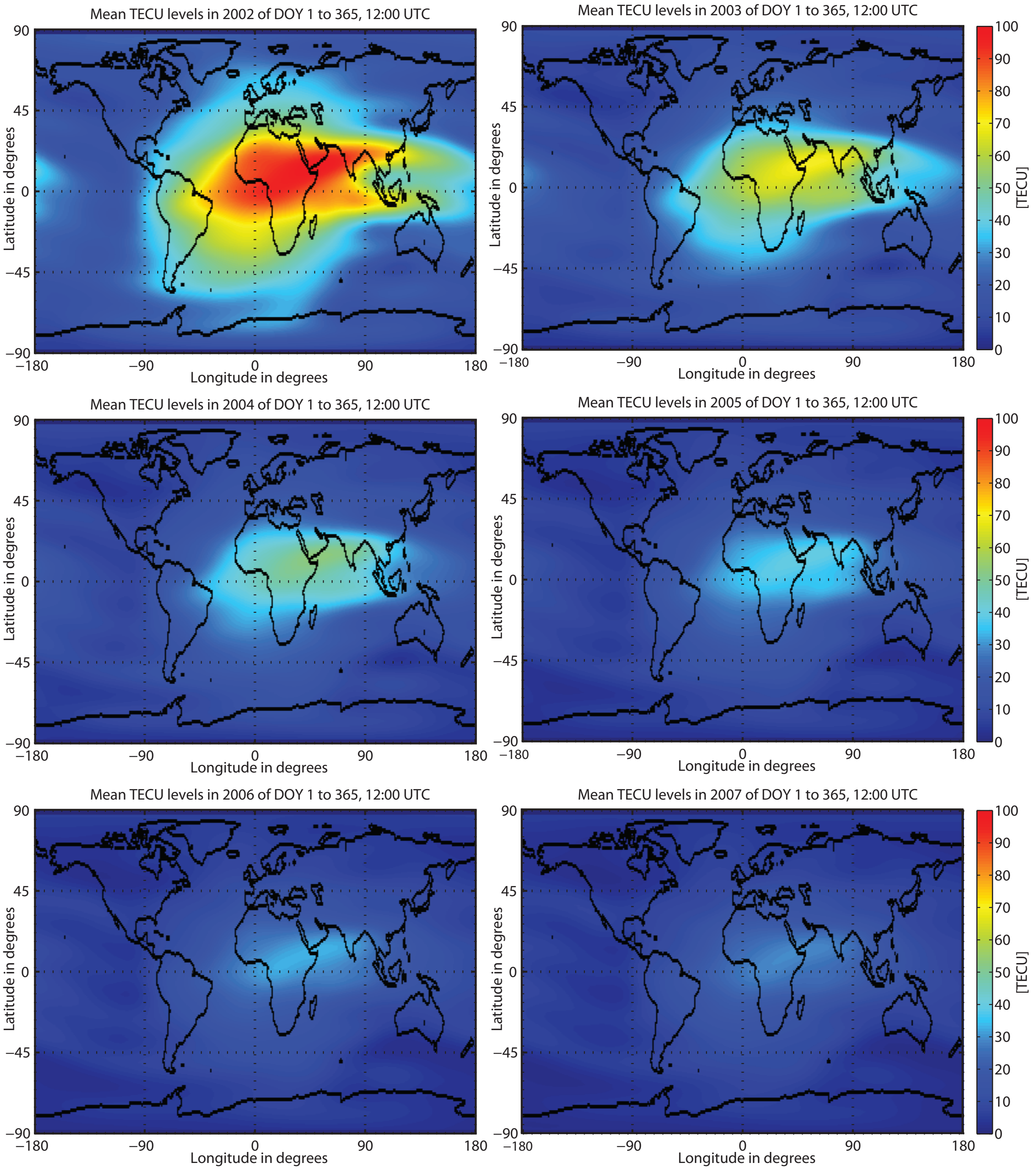

Figure 1.8: Second half of complete 11-year solar cycle.

propagation. A common further simplification is approximation of the quotient electron collision frequency and sensor frequency f with $Z = \frac{\nu}{2\pi f} \approx 0$ and also to neglect the magnetic field components Y_L and Y_T reduces Eq. 1.8 to

$$n = \sqrt{1-X} = \sqrt{1-\frac{f_N^2}{f^2}}, \tag{1.10}$$

where f_N is the plasma frequency which varies using Eq. A.13 after

$$f_N^2 = \frac{N_e e_{el}^2}{4\pi^2 \varepsilon_0 m_e} = 80.56 N_e \quad [\text{electrons/m}^3]. \tag{1.11}$$

e_{el} is the charge of an electron, m_e is the electron mass, ε_0 is the electric permittivity, and N_e is the electron number density. The second term in Eq. 1.10:$\sqrt{1-f_N^2/f^2}$ corresponds to a binomial series with negative exponent of the form:

$$(1 \pm x)^{-m} = 1 \mp mx + \frac{m(m+1)}{2!}x^2 \mp \frac{m(m+1)(m+2)}{3!}x^3 + ... \qquad \text{for } m > 0, \quad |x| < 1. \tag{1.12}$$

Insertion in Eq. 1.10 and neglecting terms of higher order results in the phase refractive index n_{phase}:

$$n_{\text{phase}} = \sqrt{1-\frac{f_N^2}{f^2}} = 1 - \frac{f_N^2}{2f^2} + ... \approx 1 - \frac{f_N^2}{2f^2} = 1 - \frac{40.28}{f^2}N_e. \tag{1.13}$$

The modulated radar wave travels with the group velocity. Therefore also the group refractive index is of interest when estimating the path delay. As illustrated in 1.3.2, the group refractive index differs by the same amount from vacuum propagation as the phase refractive index but with opposite sign, as the envelope travels with a speed lower than light. The group refractive index may be estimated using

$$n_{\text{group}} = 1 + \frac{40.28}{f^2}N_e. \tag{1.14}$$

This approximation of the group refractive index is usually used to estimate the propagation path and velocities through the ionosphere. Differences between the free space propagation are calculated for spaceborne radar applications as a two-way path delay. Using Eq. 1.4 and Eq. 1.14, the ionospheric path delay can be approximated to

$$\begin{aligned}
\Delta s &= \underbrace{\int_0^s (n-1)\,ds}_{\Delta \text{ path caused by } \Delta \text{ run-time}} + \underbrace{\Big(\int_{path} n\,ds - \int_0^s n\,ds\Big)}_{\Delta\text{path caused by ray bending}} \\
&= \frac{40.28}{f^2}\int_0^s N_e\,ds + \Big(\int_{\text{path}} 1 + \frac{40.28}{f^2}N_e\,ds - \int_0^s 1 + \frac{40.28}{f^2}N_e\,ds\Big) \\
&= \frac{40.28}{f^2}\text{TEC}_0 + \Big(s_m + \frac{40.28}{f^2}\text{TEC}_m - (s_0 + \frac{40.28}{f^2}\text{TEC}_0)\Big) \\
&\approx \frac{40.28}{f^2}\text{TEC},
\end{aligned} \tag{1.15}$$

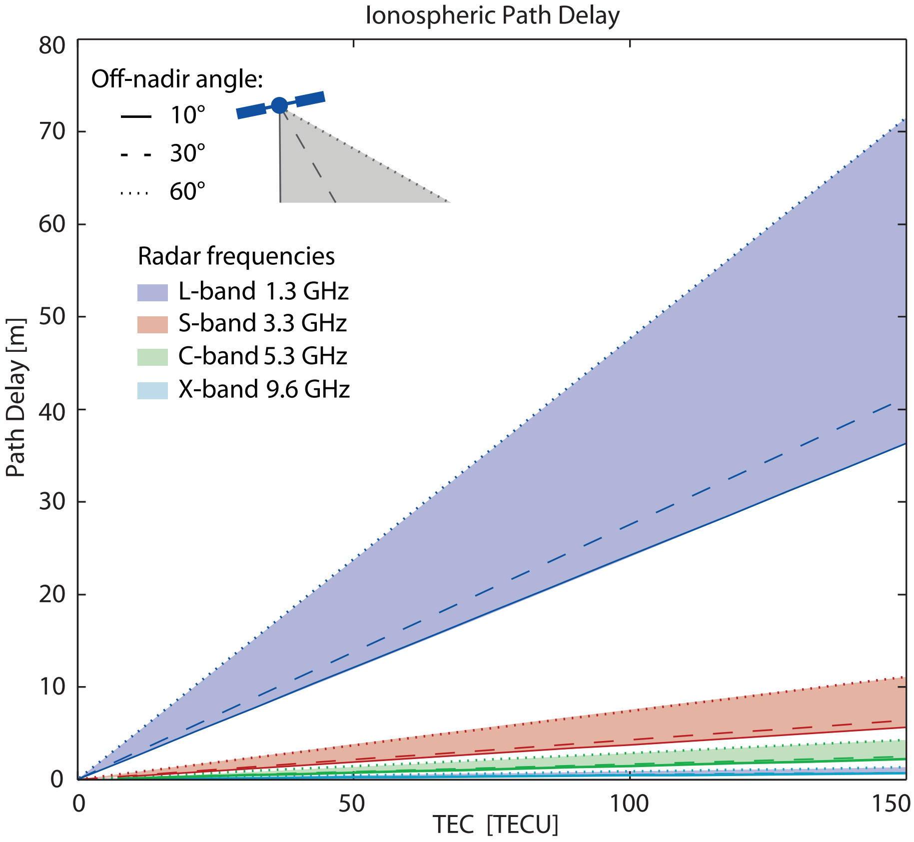

Figure 1.9: Ionospheric path delay depending on radar frequency, modified from [20]. Off-nadir angle contributions are approximated by the factor 1/cos(off-nadir).

where the approximations

$$\mathrm{TEC} = \int_{\mathrm{path}} N_e = \mathrm{TEC}_m \approx \mathrm{TEC}_0 \tag{1.16}$$

for the TEC along the line of sight TEC_0, the TEC along the path in the medium TEC_m and the propagation path

$$s_m \approx s_0 \tag{1.17}$$

were made. The contribution to the path delay resulting from ray bending is therefore usually neglected in these calculations, and TEC along the path is approximated with the TEC along the line of sight. Fig. 1.9 illustrates estimated ionospheric path delays from Eq. 1.15 for typical radar frequencies and off-nadir angles.

1.3.3.3 Derivation of Faraday Rotation

The polarisation rotation of a radar wave in the presence of a magnetic field can be described by splitting up a linearly polarised wave into two circular polarized waves E^+, E^-

rotating in opposite directions. As these waves travel along separate paths each wave sees a slightly different refractive index. The refractive index for each component can be estimated from the Appleton - Hartree equation in Eq. 1.8. In this case, only the Z component and the transverse magnetic field component Y_T can be neglected. The parallel magnetic field component Y_L induces the polarisation rotation. Under these assumptions Eq. 1.8 reduces to

$$n^2 = 1 - \frac{X}{1 \pm Y_L}. \tag{1.18}$$

From Eq. 1.18 it is obvious that there exist two different refractive indices for the two possible directions of rotation. Limiting value examination of both possibilities after [23] showed that the + sign in Eq. 1.18 is related to left-handed counterclockwise rotation along the direction of the wave and the − sign describes the rotation in the opposite direction. Insertion of the refractive index in the electric field components and estimation of the phase derivative $\frac{d\varphi}{dz}$ leads to the polarisation rotation a radar wave experiences along a distance traveled through the ionosphere. The polarisation rotation in the z direction can then be described as

$$\frac{d\varphi}{dz} = \frac{\omega_N^2 \omega_L}{2\omega c_0} = \frac{e_{el}^3 N_e Y_L}{2\varepsilon_0 m_e^2 c_0 \omega^2}. \tag{1.19}$$

For wave propagation through a plasma with electron number density N_e and a parallel magnetic field Y_L, the FR of the wave can be estimated from the difference

$$\Delta\varphi = \varphi_{\text{stop}} - \varphi_{\text{start}} = \frac{e^3}{2\varepsilon_0 m_e^2 c_0 \omega^2} \int_{\text{path}} N_e Y_L dz = \frac{2.365 \cdot 10^4}{f^2} \int_{\text{path}} N_e Y_L dz. \tag{1.20}$$

where φ_{start} and φ_{stop} describe the phase of the electromagnetic wave before entering and after leaving the dispersive medium. A more detailed version of the derivation of the polarisation rotation using the propagation properties of the electric field together with the combined refractive index is shown in Appendix A.3. A more in-depth derivation of FR in the ionosphere can also be found in [21,24]. A good survey of ionospheric effects in space-based radar can be found in [3].

1.3.4 Troposphere

Remote sensing of the troposphere with spaceborne SAR is mainly done using interferometric measurements. The data derived from the difference of two measurements shows the variations in refractivity caused by the atmosphere. At C-band frequencies or higher, and under solar quiet conditions, ionospheric contributions can often be neglected. Path delay differences caused by the refractivity variations then depend mainly on the state of the troposphere. Refractivity variations in the troposphere are caused by spatial heterogeneities in water vapour, variations in liquid water, temperature, and air pressure. Air pressure and temperature variations can be minimized by using acquisitions with short temporal separations. Radar remote sensing can therefore be used to test dynamic troposphere models, especially small-scale water vapour and mesoscale shallow convection

(MSC). From these observations, predictions of cloud development and precipitable water content can be made [24, 26].

1.3.4.1 Refractive Index of the Troposphere

Propagation of electromagnetic waves in the troposphere also depends on the refractive index. As the troposphere is a non-ionized or neutral part of the atmosphere, there is no frequency-dependent behavior of the index caused by interactions with free electrons. The refractive index depends mainly on the parameters air pressure, temperature and water vapour, and is usually divided into a hydrostatic (dry), a wet and a liquid part. Its refractive index can be divided into three components:

$$n_{\text{tropo}} = n_{\text{hyd}} + n_{\text{wet}} + n_{\text{liq}}, \tag{1.21}$$

where n_{hyd} is the hydrostatic component referred to a standard atmosphere in hydrostatic equilibrium. The wet component n_{wet} accounts for the water vapour e in the atmosphere, and the liquid component n_{liq} considers liquid water content including clouds and droplets. These refractive indices are estimated on a semi-empirical basis. In the following, a common transformation $N = (n-1)10^6$ is used for the scaled up refractivity relative to the free space refractivity $n = 1$.

The contribution of the hydrostatic component is the most relevant (according to impact) and depends on the air pressure P [hPa] and the temperature T [K] after

$$N_{\text{hyd}} = k_1 \frac{P}{T}, \tag{1.22}$$

where $k_1 = 77.6$ [K hPa^{-1}] is a refractive constant estimated from measurements [28]. The wet component can be estimated from

$$N_{\text{wet}} = k'_2 \frac{e}{T} + k_3 \frac{e}{T}, \tag{1.23}$$

where $k'_2 = 71.6$ [K hPa^{-1}], $k_3 = 3.75 \cdot 10^5$ [K^{2}hPa^{-1}] are again refractive constants and e [hPa] is the water vapour pressure. The liquid part is estimated from the liquid water content W $[\frac{kg}{m^3}]$ of clouds, the permittivity of water ε_{0w} and the density of liquid water p_{liq} as

$$N_{\text{liq}} = \frac{3W}{2p_{\text{liq}}} \cdot \frac{\varepsilon_{0w} - 1}{\varepsilon_{0w} + 2}. \tag{1.24}$$

The difference in refractivity relative to free space propagation, i.e. is the sum of the three contributions: the tropospheric refractivity N_{tropo}

$$N_{\text{tropo}} = k_1 \frac{P}{T} + k'_2 \frac{e}{T} + k_3 \frac{e}{T} + \frac{3W}{2p_{\text{liq}}} \cdot \frac{\varepsilon_{0w} - 1}{\varepsilon_{0w} + 2}. \tag{1.25}$$

Based on the refractive index, the contribution of the tropospheric path delay is estimated in the following section.

1.3.4.2 Tropospheric Path Delay

The tropospheric path delay is, as its refractive index, divided in the components hydrostatic Ψ_{hyd}, wet Ψ_{wet} and liquid delay Ψ_{liq}. The amount of tropospheric path delay in nadir direction can therefore be written as

$$\begin{aligned}\Psi_{\text{tropo}} &= \int_{path} N_{\text{hyd}} + N_{\text{wet}} + N_{\text{liq}} \quad ds \\ &= \underbrace{10^{-6}\int_{path} k_1 \frac{P}{T} ds}_{\Psi_{\text{hyd}}} + \underbrace{10^{-6}\int_{path} \Big(k_2' \frac{e}{T} + k_3 \frac{e}{T^2}\Big) ds}_{\Psi_{\text{wet}}} + \underbrace{\Psi_{\text{liq}}}_{\sim 1cm}. \qquad (1.26)\end{aligned}$$

[1]Using the ideal gas law $P = \rho R_d T$ with air density ρ, gas constant R_d, the total surface air pressure P_0

$$P_0 = g_m \int_0^{+\infty} \rho(s) ds, \qquad (1.27)$$

and the local gravity g_m the hydrostatic path delay can be estimated as

$$\Psi_{\text{hyd}} = 10^{-6} k_1 \cdot \frac{R_d}{g_m} P_0. \qquad (1.28)$$

For measured surface air pressure, the hydrostatic delay can be predicted with an accuracy of 1 mm [24]. The wet path delay cannot be modelled as well as the hydrostatic delay. A widely used approach for zenithal wet path delay approximates the integral in Eq. 1.26 [30] as:

$$\Psi_{\text{wet}} = 10^{-6} \cdot \Big(\frac{(k_2' T_m + k_3) R_d e_0}{T_0(g_m(\lambda_0 + 1) - \beta_0 R_d)}\Big) \cdot \kappa_{\text{wet}} \qquad (1.29)$$

with

$$\kappa_{\text{wet}} = \Big(1 - \frac{\beta h}{T_0}\Big)^{\frac{(\lambda_0+1)g_m}{R_d \beta_0} - 1}, \qquad (1.30)$$

where $\beta = 6.5 \cdot 10^{-3}$ $[\frac{\text{K}}{\text{m}}]$ is the temperature lapse rate, T_0 [K] the temperature-, e_0 [hPa] the water vapour pressure above sea level, T_m [K] the mean temperature of water vapour, h the target's height and λ [unitless] the average decrease of water vapour. According to [31], wet delay also depends on day of year (DOY), receiver latitude and height; they can be included using the Neill Mapping Function (NMF) as follows. For latitudes ϕ in steps of 15° a look-up table provides mean values for the parameters air pressure, temperature, water vapour pressure, temperature lapse rate, and decrease of water vapour. Each parameter ξ_{mean} is adjusted using a cosine function with an amplitude ξ_{amp} specified in the look-up table to model seasonal variations as

$$\xi'(\phi, t) = \xi_{\text{mean}} - \xi_{\text{amp}} \cdot \cos\Big(\frac{2\pi(\text{DOY} - 28)}{365.25}\Big). \qquad (1.31)$$

---

[1] Using Eq. 1.26, a virtual temperature T_v, that is, the temperature when dry air has the same density as humid air at temperature T, should be used. See e.g. [29]. Due to its small effect this distinction is neglected here.

Tropospheric Path Delay [m]		Summer $h=0$ m	Summer $h=2500$ m	Winter $h=0$ m	Winter $h=2500$ m
Off-nadir: 18.5°	hydro	2.34	1.74	2.35	1.7
	wet	0.18	0.06	0.07	0.03
	tropo	2.52	1.8	2.42	1.73
Off-nadir: 40°	hydro	2.66	1.96	2.67	1.94
	wet	0.2	0.07	0.08	0.03
	tropo	2.86	2.03	2.75	1.97

Table 1.1: Typical tropospheric path delays at mid latitudes.

Table A.1 in Appendix A.5 shows examples of these parameters with respect to latitude. To adjust the parameters with applied seasonal variations for receiver height on the Earth's surface, the individual models listed in Appendix A.4 can be used. In that model, the parameters temperature, air pressure and water vapour pressure are most responsible for changes to the tropospheric path delay. These parameters vary mainly with the receiver's height. Based on these models, Table 1.1 and Fig. 1.10 illustrate one way tropospheric path delays at mid latitudes. Fig. 1.10a) and b) are estimations for summer at an off-nadir angle of 0° in a) and 40° in b). Fig. 1.10c) and d) were calculated for winter condition. While the hydrostatic delay does not show significant seasonal behavior, the wet delay changes noticeably. As expected, larger off-nadir angles produce larger delays and the hydrostatic delay decreases remarkably with altitude. Height differences of 3000 m result in path delay changes of ≈ 1 m. This is why one can clearly see the effect of terrain variations when calculating the tropospheric path delay for a scene. Slant range propagation (sl) is approximated by dividing Ψ_{tropo} by the cosine of the incidence angle α_{inc} as

$$\Psi_{\text{tropo,sl}} = \frac{\Psi_{\text{tropo}}}{\cos \alpha_{\text{inc}}}. \tag{1.32}$$

The tropospheric path delay is usually in the range of 2.3 to 2.7 m for hydrostatic - and 0 to 0.4 m for wet path delay, all one way and zenithal. Fig. 1.11 shows an example of a calculated one way tropospheric path delay for an ENVISAT ASAR image of Lucerne/Zurich. In Fig. 1.11a), only the hydrostatic component is plotted. Fig. 1.11b) shows the complete tropospheric delay. Weak differences are identifiable in the bright areas. The wet delay contribution is mainly a constant with a faintly off-nadir-dependent addition to the hydrostatic delay in a). In addition, it can clearly be seen that at upper elevations in the southeast path delay is about 0.5 m smaller than in flatter areas in the north. It is evident that under constant atmospheric conditions, path delay depends mainly on the surface height [3]. While for precise measured surface air pressure the hydrostatic delay can be predicted to mm accuracy, the wet delay can only be estimated with an average standard deviation of ~ 5 cm [19]. The largest wet delay uncertainty is due to the estimation of water vapour pressure. In general, the troposphere is a non dispersive medium and the path delay depends mainly on the target's altitude and the distance the signal travels through the troposphere. A longer path between the satellite and the receiver (at

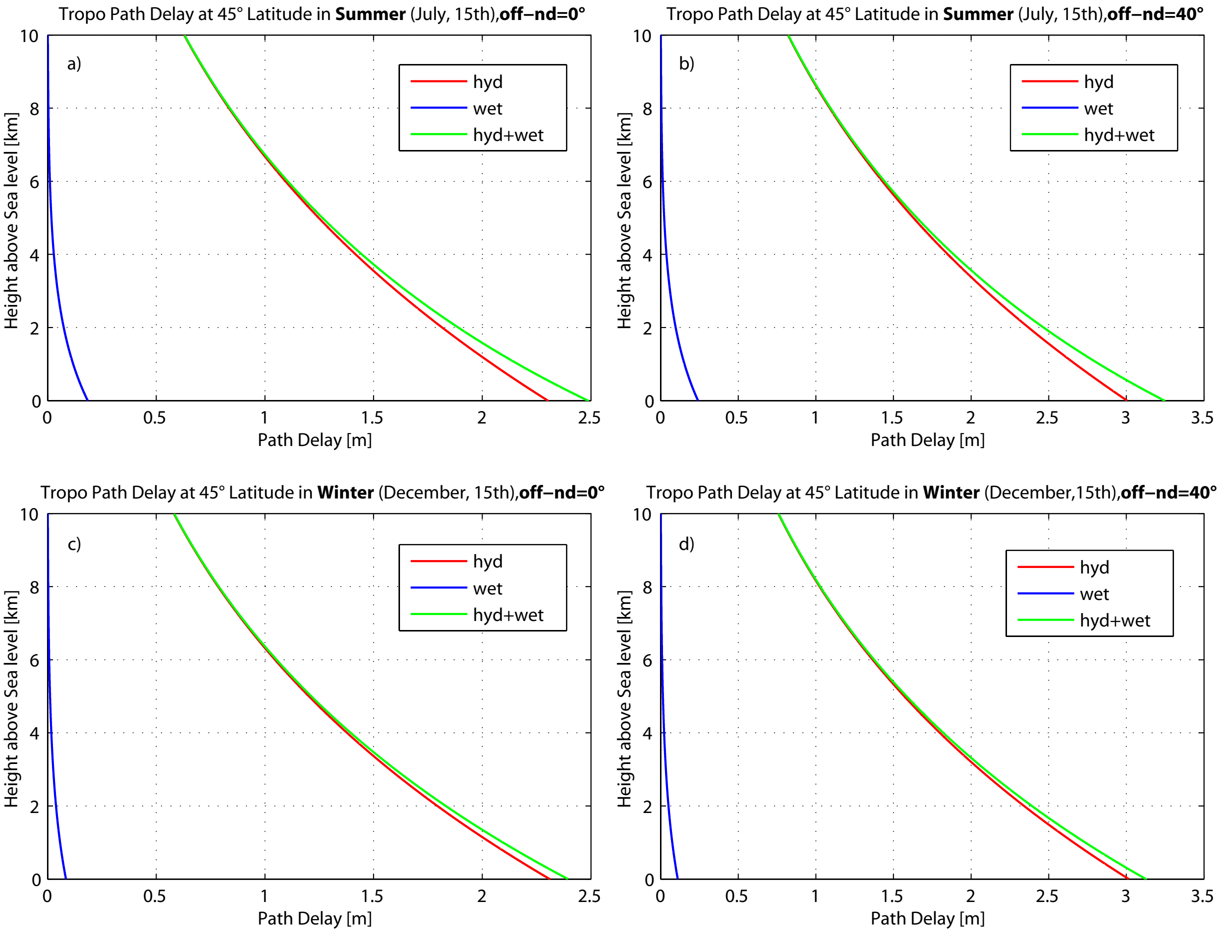

Figure 1.10: Seasonal and off-nadir-dependent tropospheric path delays. a) and b) are estimations for summer at varying off-nadir angles (off-nd). c) and d) were calculated for winter.

comparable altitudes) usually causes a correspondingly longer tropospheric path delay.

1.3.5 Propagation Attenuation through the Atmosphere

Power transmitted by the radar antenna is partially absorbed by the atmosphere and re-emitted as noise. The noise temperature T_a mainly depends on the environmental temperature T_u and the track attenuation L_a after [35]

$$T_a = T_u \cdot (L_a - 1). \tag{1.33}$$

Atmospheric noise increases with attenuation. Atmospheric attenuation therefore increases with increasing incidence angle (relative to the troposphere). The minimum for a given frequency is achieved at nadir ($\alpha_{\text{inc}} = 0°$) propagation, the maximum results from a radiation tangential to the Earth's surface.

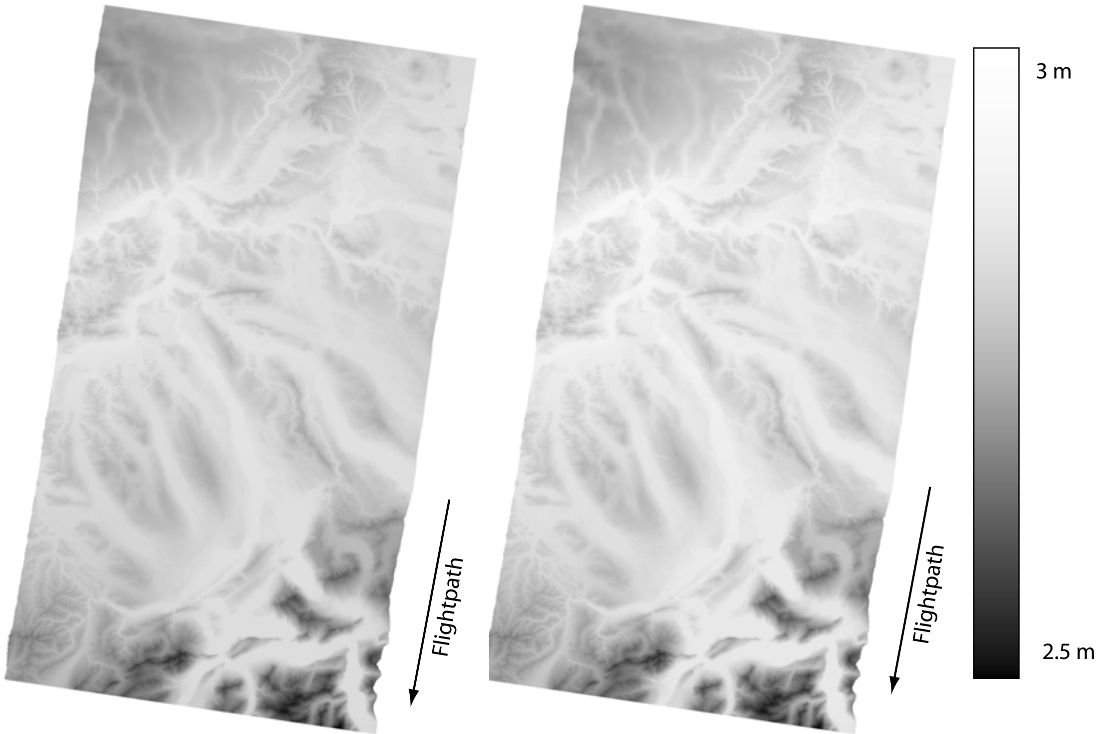

a) Hydrostatic Delay

b) Hydrostatic + Wet Delay

ENVISAT-ASAR Scene
Area of Lucerne / Zurich

Beam: IS 7
Maximum Altitude: 2531 m
Minimum Altitude: 289 m

Mean Altitude: 703 m
Mean range dist.: 833 km
Mean off-nadir: 38°

Figure 1.11: Modeled one way tropospheric path delay over Lucerne/Zurich area. In a) hydrostatic component and in b) complete tropospheric component.

Other attenuation effects are caused by absorption and rain. Fig. 1.12a) shows the attenuation caused by resonance absorption vs. frequency at two different heights. Attenuation through rain is shown in b). In Fig. 1.12a), curve (1) is the expected attenuation along the Earth's surface while curve (2) plots the resonance absorption at a height of 9150 m and horizontal wave propagation. Clearly visible are the local maxima caused by O_2 and H_2O resonances. Attenuations of 4 to 15 dB/km at the oxygen resonance at 60 GHz lowers the attractiveness of this frequency band to spaceborne radar applications. A simplified analytical approximation of the curve of absorption starting at 1 GHz up to 350 GHz is available from the ITU [36]. Attenuation of the radar signal through rain is illustrated in Fig. 1.12b). While frequencies below C-band are largely insensitive to rainfall, frequencies starting at X-band can show strong influences on radar signal propagation within regions subject to heavy rain. The two examples in Fig. 1.13 demonstrate possible effects of atmospheric attenuation and refraction. Fig. 1.13a) shows an example

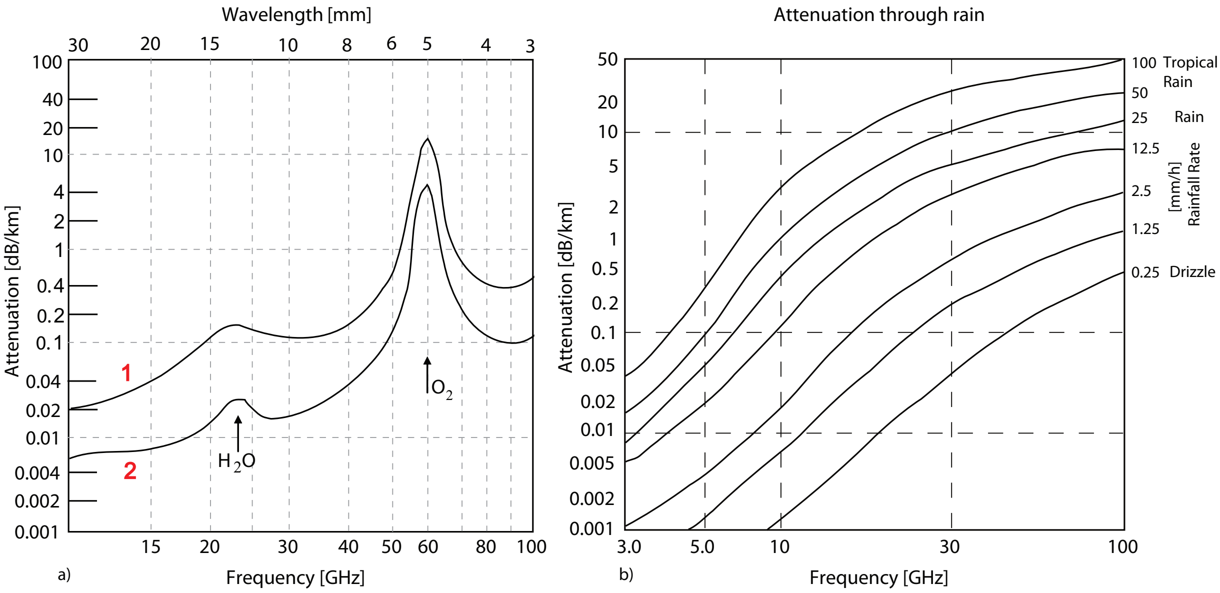

Figure 1.12: a) Mean atmospheric attenuation caused by resonance absorption relative to frequency. Curve (1) is the absorption at the Earth's surface and (2) at $h = 9150$ *m, b) frequency-dependent attenuation caused by rainfall (modified from [34]).*

for a C-band radar. It was recorded by ENVISAT ASAR on June, 18, 2007, over Tanzania. The white and dark areas at the lower left of the image clearly show the impact of refraction and attenuation caused by tropical rain. Fig. 1.13b) became famous as one of the first radar images from the high resolution X-band sensor TerraSAR-X. The image was recorded on June, 19, 2007, west of Volgograd, Russia. Attenuation due to heavy rain is visible at the upper left. Further propagation effects are less relevant to this work (e.g. scintillation-, depolarisation effects). Good overviews of these effects are provided in [3, 34, 37].

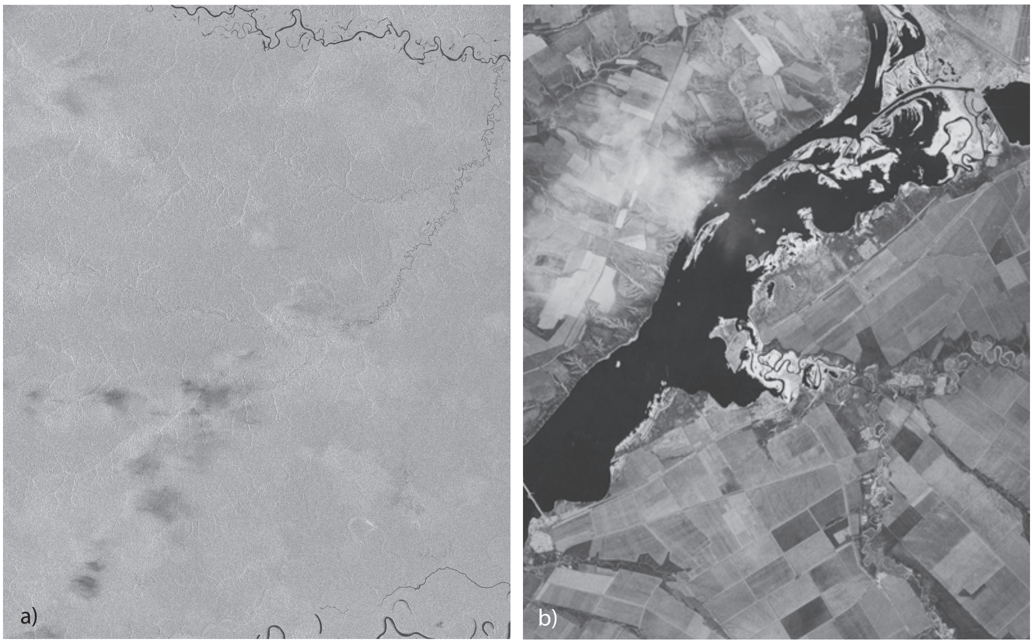

Figure 1.13: Frequency-dependent attenuation caused by rainfall. a) Envisat ASAR radar image over Tanzania in June 2007. Courtesy of P. Meadows (BAE). b) TerraSAR-X radar image over the area west of Volgograd, Russia in June 2007, ©DLR [38].

References

[1] E. J. M. Rignot, R. Zimmermann, and J. J. van Zyl, "Spaceborne applications of P band imaging radars for measuring forest biomass," *IEEE Trans. Geosci. Remote Sens.*, vol. 33, no. 5, pp. 1162–1169, Sept. 1995.

[2] G. Klawitter, *Ionosphäre und Wellenausbreitung.* Meckenheim: Siebel Verlag, 2000, vol. 3.

[3] A. Leick, *GPS Satellite Surveying.* Hoboken, New Jersey: John Wiley and Sons, Inc., 2004, vol. 3.

[4] J. Bremer, "Trends in der Meso- und Thermosphäre," *Deutscher Wetterdienst (DWD)*, 2000.

[5] J. C. Maxwell, *A Treatise on Electricity and Magnetism.* Oxford: Clarendon Press, 1873.

[6] W. Torge, *Geodäsie.* Berlin: Walter de Gruyter, 2002, vol. 2.

[7] M. Schulkin, "Average radio-ray refraction in the lower atmosphere," in *Proceedings of the I.R.E.*, vol. 40, 1952, pp. 554–561.

[8] M. Torr and D. Torr, "The seasonal behaviour of the F2-layer of the ionosphere," *Journal of Atmospheric and Solar Terrestrial Physics*, vol. 35, no. 12, pp. 2237–2251, 1973.

[9] C. Wu, C. Fry, J. Liu, K. Liou, and C. Tseng, "Annual TEC variation in the equatorial anomaly region during the solar minimum: September 1996 to August 1997," *Journal of Atmospheric and Solar Terrestrial Physics*, vol. 66, no. 3, pp. 199–207, 2004.

[10] D. Anderson, "A theoretical study of the ionospheric F region equatorial anomaly, theory," *Planetary and Space Science*, vol. 21, no. 3, pp. 409–419, 1973.

[11] D. Anderson, "A theoretical study of the ionospheric F region equatorial anomaly, results in the American and Asian sectors," *Planetary and Space Science*, vol. 21, no. 3, pp. 421–442, 1973.

[12] W. Hanson and R. Moffett, “Ionization Transport Effects in the Equatorial F Region,” *Journal of Geophysical Research*, vol. 71, pp. 5559–5572, 1966.

[13] E. Appleton, “Two anomalies in the ionosphere,” *Nature*, no. 157, p. 691, 1946.

[14] M. Dikpati, G. Toma, and P. Gilman, “Predicting the strength of solar cycle 24 using a flux-transport dynamo-based tool,” *Geophysical Research Lett.*, vol. 33, 2006.

[15] S. Schaer, “Mapping and Predicting the Earth’s Ionosphere Using the Global Positioning System,” *Geodätisch-geophysikalische Arbeiten in der Schweiz*, vol. 59, 1999.

[16] Solar Influences Data Analysis Center. (2008) Solar Influences Data Center. Last accessed Apr., 2009. [Online]. Available: http://sidc.oma.be/html/wolfmms.html

[17] J. Y. Liu, Y. J. Chuo, S. J. Shan, Y. B. Tsai, Y. I. Chen, S. A. Pulinets, and S. B. Yu, “Pre-earthquake ionospheric anomalies registered by continuous GPS TEC measurements,” *Annales Geophysicae*, vol. 22, pp. 1585–1593, 2004.

[18] T. Bleier and F. Freund, “Earthquake Alarm,” *IEEE Spec.*, vol. 42, no. 12, pp. 16–21, 2005.

[19] University of Berne. (2009) Global ionospheric maps (GIM). Last accessed Apr., 2009. [Online]. Available: ftp://ftp.unibe.ch/aiub/CODE/

[20] P. Bereuter, “Visualisation and Analysis of Ionospheric Total Content Measurements,” Department of Geography, University of Zurich, Zurich, Switzerland,” Diploma thesis, 2007.

[21] J. M. Kelso, *Radio Ray Propagation in the Ionosphere.* New York: McGraw-Hill Book Company, 1964.

[22] K. Rawer, *Wave Propagation in the Ionosphere.* Kluwer Academic Publishers, 1993, vol. 5.

[23] J. Ratcliffe, “The magneto-ionic theory,” *Wireless Engineer*, vol. 10, pp. 354–363, 1933.

[24] R. Fitzpatrick. (2005) Faraday Rotation. Last accessed Apr., 2009. [Online]. Available: http://farside.ph.utexas.edu/teaching/em/lectures/node101.html

[25] Z.-W. Xu, J. Wu, and Z.-S. Wu, “A Survey of Ionospheric Effects on Space-Based Radar,” *Waves Random Media*, vol. 14, no. 12, pp. 189–272, Apr. 2004.

[26] M. Bevis, S. Businger, T. Herring, C. Rocken, R. Anthes, and R. Ware, “GPS Meteorology: Remote sensing of atmospheric water vapor using the Global Positioning System,” *Journal of Geophysical Research*, vol. 97, no. 15, pp. 787–801, 1992.

[27] R. F. Hanssen, *Radar Interferometry.* Kluwer Academic Publishers, 2001, vol. 2.

[28] E. Smith and S. Weintraub, "The constants in the equation for atmospheric refractive index at radio frequencies," in *Proceedings of the I.R.E.*, vol. 41, 1953, pp. 1035–1037.

[29] H. Hirter, "Mehrdimensionale Interpolation von meteorologischen Feldern zur Berechnung der Brechungsbedingungen in der Geodäsie," Dissertation ETH Nr. 11578, 1996.

[30] J. Askne and H. Nordius, "Estimation of Tropospheric Delay for Microwaves from Surface Weather Data," *Radio Sci.*, vol. 22, no. 3, pp. 379–386, 1987.

[31] A. E. Niell, "Global Mapping functions for the Atmosphere Delay at Radio Wavelengths," *Journal of Geophysical Research*, vol. B2, no. 4, pp. 3227–3246, 1996.

[32] M. Jehle, O. Frey, D. Small, E. Meier, and D. Nüesch, "Estimation and Correction of Atmospheric Path Delay in radar Signal Propagation," Remote Sensing Laboratories, University of Zurich, Technical Note TX-PGS-TN-3016, Feb. 2004.

[33] P. Collins and R. Langley, "Limiting Factors in Tropospheric Propagation Delay Error Modelling for GPS Airborne Navigation," *The Institute of Navigation 52nd Annual Meeting*, 1996.

[34] Naval Air Warfare Center, *Electronic Warfare and Radar Systems Engineering Handbook.* Washington, D.C. 20361: Avionics Department AIR-4.5, Apr. 1999.

[35] M. I. Skolnik, *Radar Handbook.* McGraw-Hill, 1990, vol. 2.

[36] International Telecommunication Union, "Attenuation by atmospheric gases in the frequency range 1-350 GHz," *ITU-R, Rec.P.676-1 (03/92)*, 1992.

[37] G. Brussard and P. Watson, *Atmospheric Modelling and Millimeter Wave Propagation.* Chapman and Hall, 1995, vol. 1.

[38] DLR. (2007) First TerraSAR-X image, Volgograd, Russia. Last accessed Apr., 2009. [Online]. Available: http://www.dlr.de/desktopdefault.aspx/tabid−4237/6803_read−9519

Chapter 2

Estimation of Atmospheric Path Delays in TerraSAR-X Data using Models vs. Measurements

This chapter has been published as:
M. Jehle, D. Perler, D. Small, A. Schubert and E. Meier.
Estimation of Atmospheric Path Delays in TerraSAR-X Data using Models vs. Measurements
Sensors, Volume 8, Issue 12, Pages 8479-8491, December 2008
Reprinted with permission.

Abstract

Spaceborne synthetic aperture radar (SAR) measurements of the Earth's surface depend on electromagnetic waves that are subject to atmospheric path delays, in turn affecting geolocation accuracy. The atmosphere influences radar signal propagation by modifying its velocity and direction, effects which can be modeled. We use TerraSAR-X (TSX) data to investigate improvements in the knowledge of the scene geometry. To precisely estimate atmospheric path delays, we analyse the signal return of four corner reflectors (CR) with accurately surveyed positions (based on differential GPS), placed at different altitudes yet with nearly identical slant ranges to the sensor. The comparison of multiple measurements with path delay models under these geometric conditions also makes it possible to evaluate the corrections for the atmospheric path delay made by the TerraSAR processor and to propose possible improvements.

2.1 Introduction

The correction of atmospheric path delays in high-resolution spaceborne synthetic aperture radar systems has become increasingly important with continuing improvements to the resolution of SAR systems surveying the Earth. Atmospheric path delays must be taken into account in order to achieve geolocation accuracies better than 1 meter. These effects are mainly due to ionospheric and tropospheric influences. Path delays through the ionosphere are frequency-dependent, proportional to the inverse square of the carrier [1,3]. At frequencies higher than L-band under average solar conditions, the major contribution of the atmospheric path delay comes from the troposphere [3, 3]. The tropospheric delay is usually divided into hydrostatic, wet and liquid components [4]. The hydrostatic delay is mainly related to the dependency of the refractive index on the air pressure (i.e. target altitude) and the wet delay on the water vapour pressure. The liquid delay is due to clouds and water droplets. While the wet component can be highly variable, the hydrostatic delay normally only changes marginally because of the lack of significant pressure variations within the extent of a typical SAR scene [4].

Interferometric radar meteorology produces high resolution maps of integrated water vapour for investigations in atmospheric dynamics and forecasting [4]. Using that knowledge, global and local atmospheric effects (e.g. vortex streets, heterogeneities, turbulences) can be detected or even removed using interferometric and multi-temporal data [5–7], or by inclusion of global water vapour maps from the ENVISAT Medium Resolution Imaging Spectrometer (MERIS) sensor [8]. In addition to interferometric applications, there is a growing interest in the correction of atmospheric influences within a single SAR image. Especially for SAR geolocation measurements, these atmospheric contributions introduce 'geolocation noise' that without correction causes shifts in geocoded products.

In this paper, the tropospheric path delay was assumed to depend only on the target's altitude and the local incidence angle of the radar wave. As the variability of the wet path delay is within $\approx$0.3 m [4], the wet delay in the model is based on average atmospheric conditions, maintaining the height- and incidence angle dependencies. Thus, the contribution of the wet component to the geolocation error should usually be significant below < 0.15 m. For comparison and as a reference model, a ray-tracing approach using current weather data is introduced. A set of TSX data and GPS measurements are used to verify the results from the model, as well as for comparison with the operational TSX processor's own atmospheric correction factors. The ionospheric contributions are estimated using total electron content (TEC) estimates from the Global Navigation Satellite System (GNSS) network, and are compared to the processor of the German Aerospace Center (DLR) estimates provided in the TSX products. Since the TSX operational processor corrects the whole scene in question for the influence of the atmosphere using average TEC values, the mean scene height and the nominal mid-range incidence-angle [9], atmosphere-induced geolocation errors of $\approx$1 m are possible in mountainous regions. Together with DGPS measurements of four on-site corner reflectors and the TSX data, the results from the models and the measurements were cross-validated. A set of six TSX scenes were used to compare the operational 'average' atmospheric correction to a model utilizing meteorological data, as well as to a simple altitude-dependent model. While the meteorological model may not be suitable for operational use, the altitude-dependent model is straightforward and easy to implement. A comparison between these approaches and the DGPS measurements indicates a path toward improvement, especially in mountainous areas.

2.2 Methodology

In the following, six TerraSAR-X Stripmap scenes (30 km x 20 km) containing four identical corner reflectors at altitudes of ≈570 m (Meiringen/Interlaken) and ≈3580 m (Jungfraujoch) were examined. Figure 2.1 illustrates the geometry and location of the scenes. In order to obtain nearly identical ranges for reflectors at different off-nadir angles, the reflectors closer to nadir are located ≈3000 m below the reflectors farther from nadir. Locations fulfilling these requirements were found in Switzerland for the descending case with a pair covering the Jungfraujoch and Meiringen regions, and for the ascending case with a Jungfraujoch and Interlaken pair. The arrangement serves two purposes:

(1) The same nominal antenna gain pattern correction is normally applied to two equal-range reflectors. Therefore, differences in their reflected intensities indicate topography-induced antenna gain pattern correction errors (not investigated within this paper).

(2) The nominal correction scheme for the atmospheric path delay can be tested by comparing predicted and measured ranges. The range differences between the high- and low-altitude reflectors help quantify *relative* differences in the path delay.

Another interesting side effect is that the average scene height in both configurations is close to the midpoint between the two reflector altitudes. Additional meteorological data (temperature, water vapour pressure, air pressure) from weather stations near Meiringen,

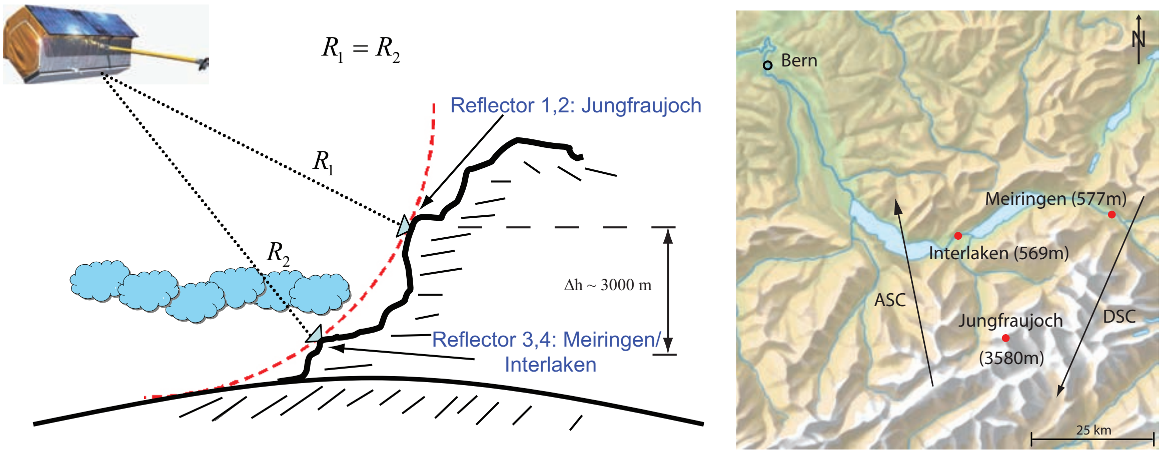

Figure 2.1: Observation geometry.

Interlaken and Jungfraujoch provided further reference information for accurate modeling of the refractive index and atmospheric path delays.

Though they play only a minor role in this case, ionospheric path delays observed during the data takes and at the corresponding locations were estimated using the TEC along the ray path. TEC measurements were obtained from global vertical TEC maps with bi-hourly temporal resolution. The TEC maps can be downloaded in the IONosphere map EXchange format (IONEX) from the Center for Orbit Determination in Europe (CODE) [10].

2.3 Models and Measurements

The following sections provide a brief description of two models used: (a) Raytracer, and (b) height-dependent. In addition, the measurements made for the estimation of the atmospheric path delays are described. While the raytracer uses weather data for an estimation of the path delays with mm accuracy, the altitude-dependent approach should provide a simplified model to correct path delays with cm accuracy.

2.3.1 Raytracer

The tropospheric delay is estimated on the basis of data provided by a numerical weather model [11]. Using this information, the raytracing algorithm integrates through the refractivity field along the path between the satellite and the point on the surface of the Earth.

The non-hydrostatic local area model COSMO-2 is used as a numerical weather model. It is operated by the Swiss Federal Office of Meteorology and Climatology and covers central Europe. It has a resolution of about 2 km and consists of 60 layers. The bottom layer follows the terrain, while the top boundary ends at 23589 m above the reference ellipsoid (WGS84). The model is used for the determination of the refractivity.

The raytracer assumes that the path followed by the ray is equivalent to the shortest geometrical path between the satellite and the point of interest. It is therefore only determined by the satellite position and the point of interest, but not by the refractivity field. This permits a simple computation of the ray paths. Since the refractivity field and its variability decreases with altitude, the length of the integration steps can be enlarged at upper levels without significantly reducing the accuracy, saving computation time. The integration method used is Newton-Cotes quadrature. However, this method has a fixed integration step length. To overcome this constraint, the atmosphere is subdivided into layers, each with a characteristic integration step size. By fixing the number of sampling points and increasing the thickness of a layer, the section of the ray path within the layer is lengthened. Consequently, the step size is increased, slightly reducing the accuracy. The thicknesses of the layers are chosen to cause zenith path delays nearly equivalent to those

Parameter	**Value**
Scale height h_s	7353.0 m
Integration height h_n	60000 m
Number of layers n	12
Number of sampling points per layer	12

Table 2.1: Setup parameters for the integration algorithm.

from a standard refractivity atmosphere (see Equation 2.2 and [12]). The boundaries of the layers are computed by following the recursive formula

$$h_{i+1} = -h_s \log(\exp(-\frac{h_i}{h_s}) - \frac{dt_{\text{tot}}}{n}) \tag{2.1}$$

$$dt_{\text{tot}} = \int_{h_0}^{h_n} \exp(-\frac{h}{h_s})dh \tag{2.2}$$

where h_i is the lower boundary height of the i-th layer ($i = 0, \dots, n-1$) and h_s the scale height. The parameter h_0 is set to the height of the point of interest and h_n to the height up to which will be integrated. The integration is carried out for each layer, and then the delays for all layers are added up to obtain the total result.

The refractivity N is usually not a prognostic variable in numerical weather models. However, it can be calculated from the partial dry air pressure p_d (in hPa), temperature T (in K) and partial water vapour pressure p_w (in hPa) using a formula published by Rüeger [13]

$$\mathrm{N} = 77.6890\frac{p_d}{T} + 71.2952\frac{p_w}{T} + 375463\frac{p_w}{T^2}. \tag{2.3}$$

The prognostic variables used in the integration are interpolated at the sampling points. A multi-linear interpolation method is applied in 4 dimensions (space and time). If a sampling point is located outside the domain of the weather model, the meteorological quantities are extrapolated from the values at the boundaries. Points situated above or below the area of interest are exponentially extrapolated, whereas points located adjacent to the area of interest are set to the value of the nearest boundary point.

The values of the interpolation parameters are listed in Table 2.1. The free parameter h_s in the exponential function used for estimating the layer thickness is proposed in [12]. The upper bound of the accuracy of the integration algorithm is set to 1 mm. Several tests were carried out to find adequate values for the remaining parameters fulfilling the accuracy constraints. More details on the accuracy of raytracers can be found in [14, 15].

2.3.2 Height-dependent Model

Since the tropospheric delay is most sensitive to altitude, a quick, straightforward and purely height-dependent approach was derived from standard models including mean estimates of the surface air-pressure P_0, temperature and water vapour. As mentioned in

$\mathbf{P}_{0,\texttt{mid}}$	$\mathbf{T}_{0,\texttt{mid}}$	$\mathbf{e}_{0,\texttt{mid}}$	$\beta_{\texttt{mid}}$	$\lambda_{\texttt{mid}}$
1013.25 [hPa]	288.15 [K]	11.691 [hPa]	$6.5\cdot10^{-3}$ [K/m]	3 [-]

Table 2.2: Parameters used to model the tropospheric path delay.

the introduction, the tropospheric delay is usually divided into hydrostatic- ($\Psi_{\texttt{hyd}}$), wet- ($\Psi_{\texttt{wet}}$) and liquid- ($\Psi_{\texttt{liq}}$) components and can be written as [16]:

$$\Psi_{\texttt{tropo}} = \Psi_{\texttt{hyd}} + \Psi_{\texttt{wet}} + \Psi_{\texttt{liq}} \tag{2.4}$$

The hydrostatic component refers to a standard atmosphere (in hydrostatic equilibrium). The wet component accounts for the water vapour while the liquid component takes into account the liquid water content (clouds, droplets) along the signal path. Due to its small contribution (on the order of a mm) $\Psi_{\texttt{liq}}$ is usually neglected for SAR path delay estimates [4]. The hydrostatic component $\Psi_{\texttt{hyd}}$ in the nadir direction can be derived from [17, 18]:

$$\Psi_{\texttt{hyd}} = 10^{-6} k_1 \cdot \frac{R_d}{g_m} P_0. \tag{2.5}$$

where g_m is the acceleration due to local gravity, k_1=77.6 $[\frac{K}{\texttt{mbar}}]$ is a refractive constant, and R_d=287 $[\frac{J}{K\cdot\texttt{kg}}]$ is the ideal gas constant. The wet delay contribution is estimated using [19]:

$$\Psi_{\texttt{wet}} = 10^{-6} \cdot \left(\frac{(k_2' T_m + k_3) R_d e_0}{T_0(g_m(\lambda+1) - \beta R_d)}\right) \cdot \kappa_{wet} \tag{2.6}$$

with:

$$\kappa_{\texttt{wet}} = \left(1 - \frac{\beta h}{T_0}\right)^{\frac{(\lambda+1)g_m}{R_d \beta} - 1} \tag{2.7}$$

where $k_2' = 23.3$ $[\frac{K}{\texttt{mbar}}]$, $k_3 = 3.75 \cdot 10^5$ $[\frac{K^2}{\texttt{mbar}}]$ are refractive constants, $\beta = 6.5$ $[\frac{K}{\texttt{km}}]$ is the temperature lapse rate, T_0 [K] the temperature-, e_0 [hPa] the water vapour pressure above sea level, T_m [K] the mean temperature of water vapour, h the target height and λ [unitless] the average water vapour decrease.

For the generation of a single altitude-dependent estimate of the tropospheric path delay for SAR applications, the average atmospheric parameters shown in Table 2.2 are used to determine the coefficients of a polynomial that fits the path delay data for heights h ranging from 0 to 9000 m in a least-squares sense. The resulting approach

$$\Psi_{\texttt{tropo,zenith}} = \frac{h^2}{8.55 \cdot 10^7} - \frac{h}{3411} + 2.41 \quad [\texttt{m}] \tag{2.8}$$

estimates the tropospheric delay in the zenith direction. The delay in the look direction of the antenna can be approximated using the nominal incidence angle $\alpha_{\texttt{inc}}$ [rad] according to

$$\Psi_{\texttt{tropo}} = \frac{\Psi_{\texttt{tropo,zenith}}}{\cos \alpha_{\texttt{inc}}} \quad [\texttt{m}], \tag{2.9}$$

where the incidence angle is calculated using the local height above the ellipsoid. This approximation of tropospheric path delay is compared later with an average delay correction and a path delay estimation based on the raytracer using meteorological data as described above. Figure 2.2 shows a block diagram of the three methods used for the estimation of tropospheric path delays. Figure 2.2a) illustrates the altitude-dependent method, Figure 2.2b) the raytracer and Figure 2.2c) the estimation and comparison of path delays from SAR data and GPS measurements described in the following section (JJ: Jungfraujoch, MI: Meiringen/Interlaken).

2.3.3 SAR and GPS Measurements

Estimation of atmospheric path delay directly from the SAR data was performed using precise DGPS measurements of four observed targets (corner reflectors) in the images. The range distance between the DGPS coordinates and the sensor is considered to be the reference for all estimates. The atmospheric corrections proposed in the TSX annotations, based on an average reference height (AVG), are applied to the image data (correction of fast time parameters). Their differences compared to the GPS measurements provide relative deviations from the reference range distance. The relative differences in path delay estimates between the corner reflectors located at different altitudes are calculated in a final step. These calculations point out varying propagation properties and indicate possibilities for refinement (Figure 2.2c). Ionospheric contributions are also considered, although they play a minor role at X-band frequencies, especially at the current solar minimum. Average estimates for their contribution (path delay at 5 TECU) are provided

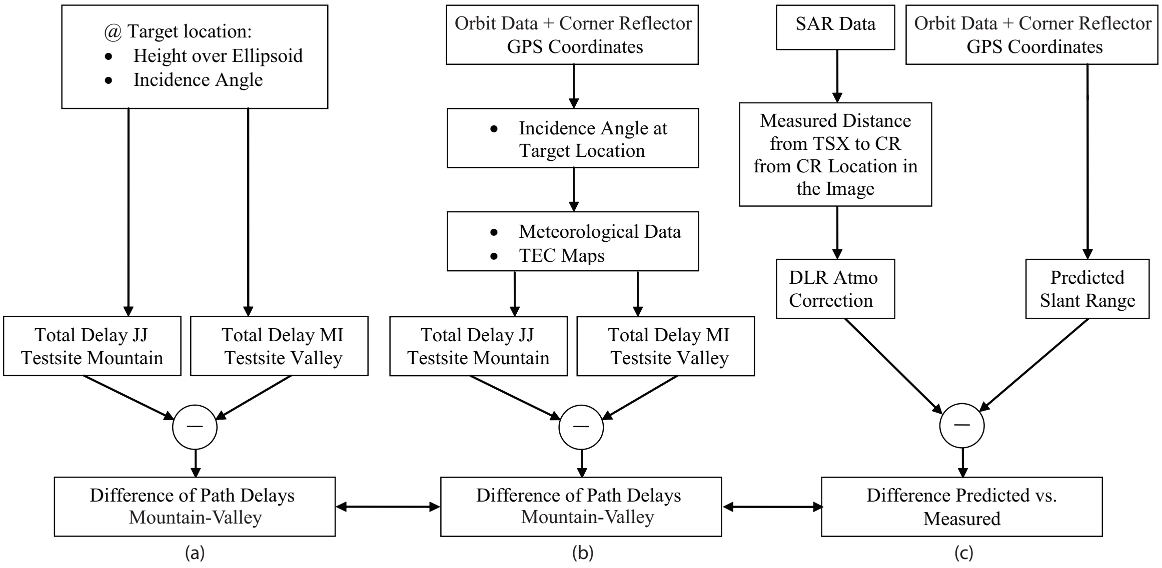

Figure 2.2: Scheme of methods used for comparison of atmospheric path delays; Testsite Jungfraujoch (JJ) on mountain site, Meiringen and Interlaken (MI) in the valley.

in the TSX product annotations [20]. Measured values were estimated using TEC maps describing spatial variations in TEC values across the Earth. The one-way ionospheric path delay may be estimated from [21]:

$$\Psi_{\text{iono}} = K \cdot \frac{\text{TEC}}{f_c^2} \cdot \frac{1}{\cos \alpha_{\texttt{inc}}} \tag{2.10}$$

where f_c is the center frequency of the radar wave, c the speed of light and $K = 40.3 \frac{\text{m}^3}{\text{s}^2}$ is a refractive constant. The factor $\frac{1}{\cos \alpha_{\texttt{inc}}}$ converts the path delay from nadir to the path at a particular incidence-angle. Measurements from GNSS networks provide multiple maps per day, and may be downloaded in a standardized format from the internet [10]. Given the TEC values together with the corresponding satellite and target positions, the expected path delay is calculated.

2.4 Path Delay Results

As a first test, the absolute image localization error for all four corner reflectors in each of the six TSX products was measured. Accurately surveyed DGPS measurements of the corner reflectors were used to predict their range and azimuth positions in each image, and these predictions were compared to their measured locations. Figure 2.3 shows an example for the absolute location error estimate for (a) Jungfraujoch, (b) Interlaken (INT) and (c) Meiringen (MEI). At successive ’zoom’ levels, the blue crosses indicate the prediction based on the GPS measurements, which represent the runtime measurements under ideal vacuum conditions. These image position predictions were made by solving the Doppler and range equations [22] using the surveyed target coordinates, together with the precise orbit state vectors and the image timing annotations [20]. The precise corner reflector (phase center) position in the image was determined by searching for local maxima in the neighborhood of the strong targets, using complex-FFT oversampling (factor of 50) to obtain sub-sample accuracy [22]. Results of the following analysis are based on the location error of the two corner reflectors at each test site, both at the same altitude and equidistant to the sensor. Figure 2.4 shows a scatter plot of all estimated location errors. The blue circles indicate descending-, the red circles ascending products. While for Interlaken and Meiringen (b) the range errors are on the order of a cm, for the Jungfraujoch site (a) the range errors increase to a mean of approximately 0.58 m. Since the TSX tropospheric correction is based on an *average* scene height roughly halfway between the test site altitudes (Jungfraujoch and Meiringen/Interlaken), the expected average location errors in range for the sites would be expected be approximately of the same magnitude with opposite signs.

In order to estimate the height-dependent path delays for each test site, the range errors were subtracted from the average range delay (see Table 2.3). As expected, atmospheric delays at the higher altitude of the Jungfraujoch site ($\Psi_{\texttt{JJ,AVG}}$) are smaller than at the Meiringen/Interlaken sites ($\Psi_{\texttt{MI,AVG}}$). The estimated relative difference in one-way path delay between both sites has a mean of 0.779 m. Differences in the descending case

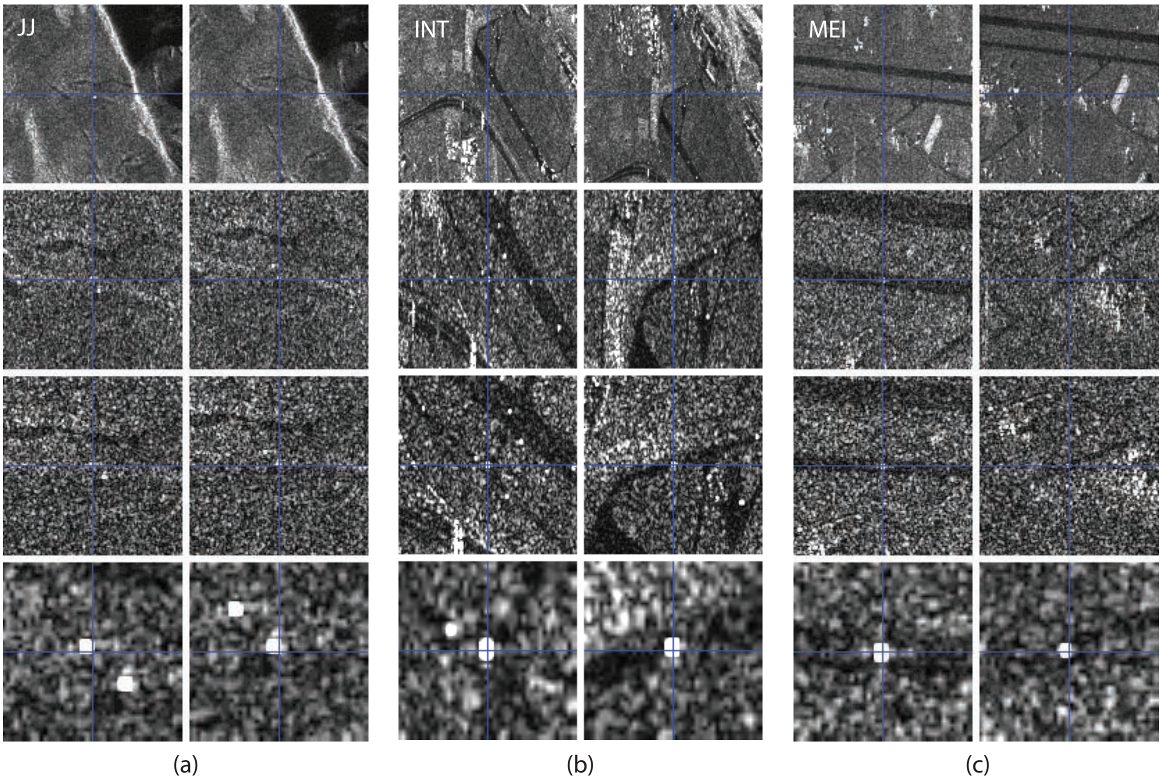

Figure 2.3: Example of zoomed in and interpolated corner reflectors in TSX imagery. The blue cross indicates the GPS derived position prediction and the strong white target the actual measured position of the CR in the image.

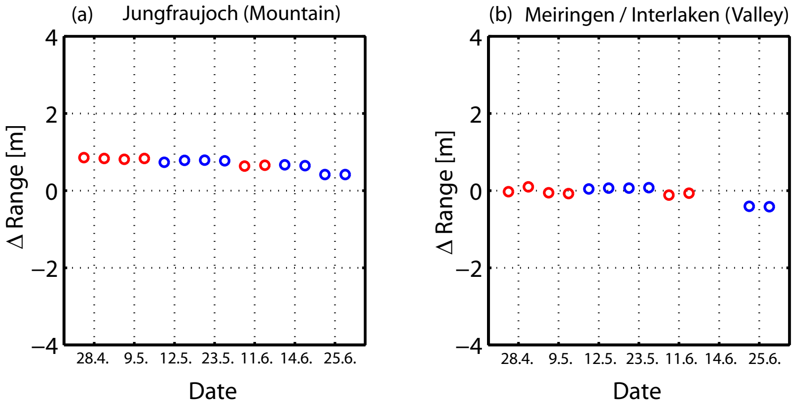

Figure 2.4: Absolute location error estimations for each testsite. Red circles mark descending and blue circles ascending geometry. Note: An additional data take is plotted in Figure 2.4(a). As it was not possible to deploy the CRs in Interlaken at that time, this data take was omitted in the analysis that followed.

Predicted Path Delay from Measurement and GPS								
A/D	Ref.Hgt.	$\alpha_{\mathtt{inc}}$	$\varnothing\Psi_{\mathtt{AVG}}$	ΔRg.$_{\mathtt{JJ}}$	ΔRg.$_{\mathtt{MI}}$	$\Psi_{\mathtt{JJ,AVG}}$	$\Psi_{\mathtt{MI,AVG}}$	$\Psi_{\mathtt{JJ}}$-$\Psi_{\mathtt{MI}}$
D	2163 m	31.2°	1.874 m	0.846 m	0.036 m	1.03 m	1.84 m	0.809 m
D	2166 m	31.2°	1.873 m	0.818 m	-0.064 m	1.05 m	1.94 m	0.882 m
A	1865 m	24.0°	1.845 m	0.755 m	0.055 m	1.09 m	1.79 m	0.700 m
A	1827 m	24.0°	1.857 m	0.782 m	0.068 m	1.07 m	1.79 m	0.714 m
D	2164 m	31.2°	1.874 m	0.646 m	-0.091 m	1.23 m	1.96 m	0.737 m
A	1827 m	24.0°	1.857 m	0.418 m	-0.414 m	1.44 m	2.27 m	0.832 m
Mean Values			1.863 m	0.581 m	-0.068 m	1.16 m	1.92 m	0.779 m

Table 2.3: Predicted path delays from measurements and GPS. The Ref.Hgt., α_{inc} and $\varnothing\Psi_{AVG}$ refer to the average scene height, the mid incidence angle and average tropospheric path delay respectively, as annotated in the TSX products (JJ: Jungfraujoch, MI: Meiringen/Interlaken, dates are all in the year 2008).

are usually higher in comparison to the ascending cases, as the signal path through the troposphere was longer, due to the more oblique incidence angle. Results from the height-dependent model (HM) and the raytracer (RT) use the altitudes and incidence angles estimated for each corner reflector position. The path delays from the TSX annotations ($\varnothing\Psi_{\mathtt{AVG}}$) are used together with the differences ΔRg.$_{\mathtt{JJ}}$ and ΔRg.$_{\mathtt{MI}}$ to map to the delays according to the altitude of the testsite. Figure 2.5(a) and (b) show the total tropospheric path delays (hydro + wet component) estimated from the models, including the results from the measurements as well as the ionospheric delays. In Figure 2.5(c) the black and yellow lines show the distribution of air pressure and water vapour during the data takes in comparison to the wet path delays estimated from the raytracer. Both pressure parameters are normalized to the assumptions of the standard atmosphere made in Table 2.2. Figure 2.5(d) shows the differences in atmospheric path between the mountain (Jungfraujoch) and the valley (Meiringen/Interlaken) testsites and therefore measures the dynamic of the path delay models at these altitudes. The results from the height-dependent model are very similar to the raytracer results. An exceptional scene was the data from June 25th (heavy rain) where high water vapour pressure was measured, which significantly increased the wet path delay contribution. The path delays estimated from the image as compared to the GPS measurements are plotted in red, and are less consistent with the model results, but strongly correlate with the water vapour measurements (Figures 2.5(a) to (c)). This is unsurprising, as the variations arise from the differences between these constant delays and the GPS-measured vacuum propagation (ΔRg.$_{\mathtt{MI}}$, ΔRg.$_{\mathtt{JJ}}$). The TSX average correction does not significantly vary across the ascending/descending geometries and therefore causes only a constant shift. From Figure 2.5(a) and (b) it can be seen that the shifts between the model and the measurements are nearly constant. This suggests that the tropospheric path delays from the TSX annotations consistently *underestimate* the true delays. On the other hand, this shift implies that if the delays from the models were applied to the TSX image, we would expect an average range shift ΔRg.$_{\mathtt{MI}}$ and ΔRg.$_{\mathtt{JJ}}$ of ≈0.7 m across all test sites. It follows that the measurements in Interlaken only performed with cm accuracy since the underestimated path delay having been compensated by the overall constant ≈0.7 m shift.

Path delays caused by the ionosphere were modelled to have been in the cm range. The average one-way ionospheric delays from measurements are comparable to, although slightly higher than, the average values provided in the TSX annotations ($\varnothing\Psi_{\texttt{Meas,iono}}=4.7$ cm, $\varnothing\Psi_{\texttt{AVG,iono}}=2.5$ cm).

The relative differences of the path delays between the test sites in Figure 2.5(d) can be considered an indication of the model's ability to capture altitude-dependent variations. With mean values of $\varnothing\Delta\Psi_{\texttt{HM}}=0.822$ m, $\varnothing\Delta\Psi_{\texttt{RT}}=0.786$ m and $\varnothing\Delta\Psi_{\texttt{AVG}}=0.779$ m, all models agreed closely.

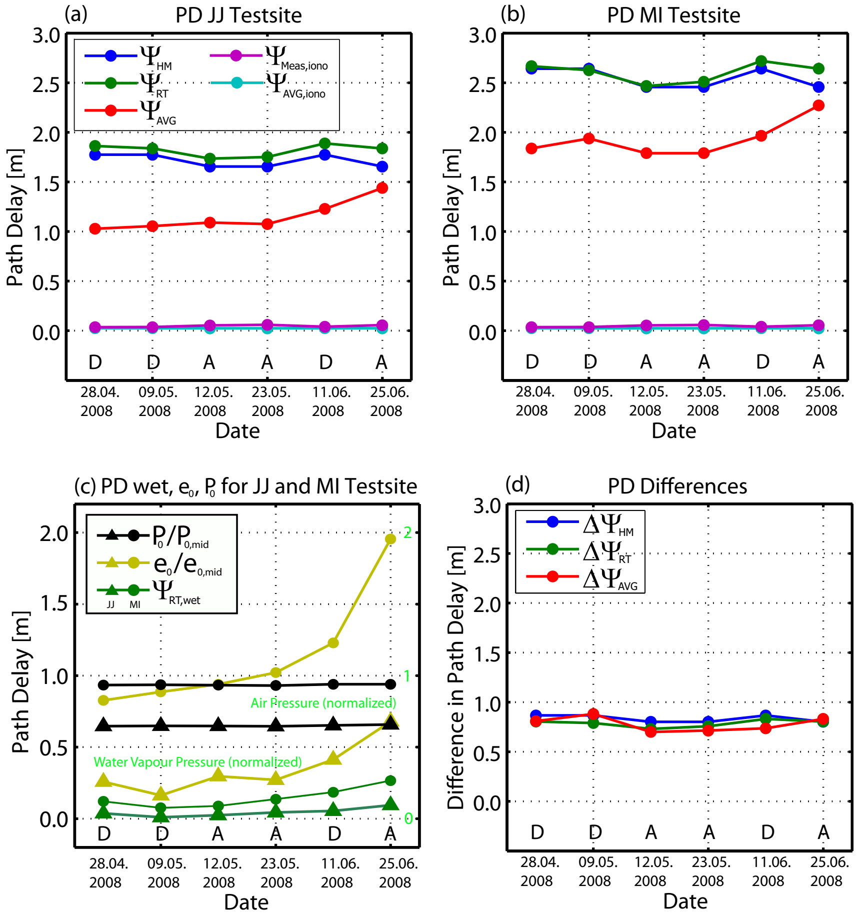

Figure 2.5: Modelled and measured atmospheric path delays. Path delays in a) for JJ testsite and in b) for the MI testsites. In c) wet path delays compared to measured air- and water vapour pressure (normalized) and in d) path delay differences between the results of the JJ and the MI testsites.

2.5 Discussion and Conclusion

With TerraSAR-X, a civilian spaceborne satellite is for the first time able to observe the Earth with a radar resolution on the order of 1 m. At such resolutions, the influence of the atmosphere on the geolocation accuracy plays a significant role and must be taken into account. Various methods for the correction of these delays can be applied, depending on the scientific application. In this work, we investigated the range delays predicted by an altitude- and incidence-angle dependent model, a raytracer and a model which corrects the path delay as a scene average. Model results were compared for six TerraSAR-X datasets containing four corner reflectors, two at altitudes 3000 m above the others.

We found that the scene-average method significantly *underestimates* the tropospheric delays compared to the raytracer model and the height-dependent polynomial. While the range location errors for the low-altitude reflectors were normally on the order of a cm, the range errors at the high altitude station were usually over half a meter. The absolute location error for a scene-average path delay estimate should result in comparable range errors at equal height offsets above and below the average scene height. Our test sites at Jungfraujoch (3580 m) and Meiringen/Interlaken (≈570 m) with average scene heights of 2160 m/1860 m nearly fullfilled that condition. When the annotated delays from the TSX products were replaced by the results from the raytracer for the individual locations, a nearly constant range shift of ≈0.7 m was estimated. On the one hand, this indicates that the corrections from the raytracer are reasonable, yet on the other hand, suggests an inherent systematic shift of ≈0.7 m which is still within the specifications of the TSX accuracy requirements.

Since the dynamics of all methods are similar, differences between the models are likely due to different atmospheric starting positions. The results for the last two acquisitions are more similar for the various models. The range deviations from the image measurements and the path delays from the raytracer show that this is probably due to the increased amount of atmospheric water vapour during these data takes. As a result, the path delay in the SAR image increases. The standard correction from the TSX annotations does not take these effects into account. Therefore, the influence of the higher water vapour pressure could be directly observed in the changes in the range location errors. In other words, the larger path delay in the image compensates for the underestimated average path delay which leads to the observed 'increased' accuracy. Path delay estimates from the raytracer include the higher water vapour pressure, but probably to a lesser extent, as the heavy rainfall was observed to be very localized. This might also be seen from its path delay estimates. Loss of accuracy caused by poor modelling of wet path delay estimation in such storm events are not expected to exceed ≈10 to 15 cm.

Separation of the ionospheric delays from the total atmospheric delays also indicates that the average value from the TSX annotations tends to underestimate the delay estimated from the measured TEC maps by a mean of 2.2 cm. Although solar activity and therefore the ionospheric delay is presently near its minimum, future path delays at X-band in mid-latitude regions are not expected to regularly exceed 0.30 m.

Unlike the scene-average model, the results from the height-dependent polynomial are very close to the raytracer estimates. The height-dependent polynomial would therefore seem to be a straightforward alternative for operational use. Worse results would be expected at high latitudes, as the correction is based on a standard atmosphere most representative of mid-latitude regions. This could be improved relatively simply with extra terms 'capturing' latitude-induced dynamics. As the raytracer produces the most accurate results, a correction of the data with this approach would be desirable; however, operational inclusion of the current weather data is currently not feasible.

Acknowledgments

We would like to thank the DLR in Oberpfaffenhofen for their scientific support and for providing us with the TerraSAR-X datasets granted within the framework of CAL0163. Furthermore, we are indebted to the International Foundation High Altitude Research Stations Jungfraujoch and Gornergrat (HFSJG), 3012 Bern, Switzerland, who made it possible for us to carry out our experiments at Jungfraujoch. We also would like to thank the respective airport authorities for their permission to deploy the corner reflectors on the grounds of the Meiringen and Interlaken airports and Dr. D. Leuenberger working at the Swiss Federal Office of Meteorology and Climatology MeteoSwiss for providing numerical weather prediction (NWP) model data.

References

[1] K. Davies, *Ionospheric Radio.* London: Peter Peregrinus Ltd., IEE Electromagnetic Waves, 1990, vol. 31.

[2] Z.-W. Xu, J. Wu, and Z.-S. Wu, "A survey of ionospheric effects on space-based radar," *Waves in Random Media*, vol. 14, no. 12, pp. 189–272, Apr. 2004.

[3] M. Jehle, O. Frey, D. Small, E. Meier, and D. Nüesch, "Estimation and correction of atmospheric path delay in radar signal propagation," Remote Sensing Laboratories, University of Zurich, Technical Note TX-PGS-TN-3016, Feb. 2004.

[4] R. F. Hanssen, *Radar Interferometry.* Kluwer Academic Publishers, 2001, vol. 2.

[5] F. Chaabane, A. Avallone, F. Tupin, P. Briole, and H. Maitre, "A multitemporal method for correction of tropospheric effects in differntial SAR interferometry: Application to the gulf of Corinth earthquake," *IEEE Transactions on Geoscience and Remote Sensing*, vol. 45, pp. 1605–1615, 2007.

[6] H. Tarayre and D. Massonnet, "Effects of a refractive atmosphere on interferometric processing," *Geoscience and Remote Sensing Symposium, 1994. IGARSS '94. Surface and Atmospheric Remote Sensing: Technologies, Data Analysis and Interpretation.*, vol. 2, pp. 717–719, 1994.

[7] H. Kimura and H. Kinoshita, "Effect of tropospheric range delay corrections on differential SAR interferograms," *Geoscience and Remote Sensing Symposium, 2001. IGARSS '01. IEEE 2001 International*, vol. 5, pp. 2049–2051, 2001.

[8] Q. Zeng, Y. Li, and X. Li, "Correction of tropospheric water vapour effect on ASAR interferogram using synchronous MERIS data," *Geoscience and Remote Sensing Symposium, 2007. IGARSS 2007. IEEE International*, pp. 2086–2089, 2007.

[9] T. Fritz, "Comments on TerraSAR-X Geolocation / Coordinate Annotation," 2008, Personal communication and handouts.

[10] Astronomical Institute of the University of Bern, "Centre for Orbit Determintation (CODE)," http://www.aiub.unibe.ch/download/CODE/, 2008.

[11] G. Doms and U. Schättler, "A description of the nonhydrostatic regional model LM. part I: Dynamics and numerics," *Consortium for Small-Scale Modelling COSMO, Offenbach, Germany*, no. LM-F90 2.18, p. 140, 2002.

[12] Recommendations and Reports of the CCIR XVIth Plenary Assembly, "Radiometeorological data," Dubrovnik, 1986, vol. 5, (Propagation in non-ionized media).

[13] J. M. Rüeger, "Refractive index formulae for radio waves," *Integration of Techniques and Corrections to Achieve Accurate Engineering*, 2002.

[14] T. Pany, P. Pesec, and G. Stangl, "Atmospheric GPS slant path delays and ray tracing through numerical weather models, a comparison," *Physics and Chemistry of the Earth, Part A: Solid Earth and Geodesy*, vol. 26, no. 3, pp. 183–188, 2001.

[15] X. Yang, B. H. Sass, G. Elgered, J. M. Johansson, and T. R. Emardson, "A comparison of precipitable water vapor estimates by an NWP simulation and GPS observations," *Journal of Applied Meteorology*, vol. 38, no. 7, pp. 941–956, 1999.

[16] M. Jehle, D. Small, E. Meier, and D. Nüesch, "Improved knowledge of SAR geometry through at-mospheric modelling," in *Proceedings of EUSAR*, 2004.

[17] J. Saastamoinen, "Contributions to the theory of atmospheric refraction," *Bulletin Geodesique*, no. 105-107, 1973.

[18] J. Davis, T. Herring, I. Shapiro, A.E.E.Rogers, and G. Elgered, "Geodesy by radio interferometry: Effects of atmospheric modelling errors on estimates of baseline length," *Radio Science*, vol. 20, no. 6, pp. 1593–1607, 1985.

[19] P. Collins and R. Langley, "Limiting factors in tropospheric propagation delay error modelling for GPS airborne navigation," *The Institute of Navigation 52nd Annual Meeting*, 1996.

[20] T. Fritz, "TerraSAR-X ground segment," DLR, Level 1b Product Format Specification TX-GS-DD-3307, Dec. 2007.

[21] U. Wild, "Ionosphere and geodedetic satellite systems: Permanent GPS tracking data for modelling and monitoring," *Geodätisch-geophysikalische Arbeiten in der Schweiz*, vol. 48, 1994.

[22] D. Small, B. Rosich, A. Schubert, E. Meier, and D. Nüesch, "Geometric validation of low and high resolution ASAR imagery," *Proc. of 2004 Envisat and ERS Symposium, Salzburg, Austria*, no. ESA SP-572, p. 8, 2005.

Chapter 3

Measurement of Ionospheric Faraday Rotation in Simulated and Real Spaceborne SAR Data

This chapter has been published as:
M. Jehle, M. Rüegg, L. Zuberbühler, D. Small and E. Meier.
Measurement of Ionospheric Faraday Rotation in Simulated and Real Spaceborne SAR Data
Transactions on Geoscience and Remote Sensing, Volume 47, Issue 5, Pages 1512-1523, May 2009
Reprinted with permission.

Abstract

The influence of the atmosphere on a frequency-modulated electromagnetic wave traversing the ionosphere has becoming increasingly important for recent and upcoming low-frequency and wide-bandwidth spaceborne synthetic aperture radar (SAR) systems. The ionized ionosphere induces Faraday rotation (FR) at these frequencies that affects radar polarimetry and causes signal path delays resulting in a reduced range resolution. The work at hand introduces a simulation model of SAR signals passing through the atmosphere including both frequency-dependent FR and path delays. Based on simulation results from this model [proven with real Advanced Land Observing Satellite Phased Array L-band Synthetic Aperture Radar (PALSAR) data], estimation of FR in quad-polarized SAR data using the given approach is shown for raw, range-compressed and focused radar images. Path delays and signal chirp bandwidth effects are considered. Investigations discuss the suitability of raw and compressed data vs. combination of total electron content (TEC) maps with the Earth's magnetic field for FR estimation and deduced from a large number of analyzed PALSAR data sets.

3.1 Introduction

With the successful launch of the Advanced Land Observing Satellite (ALOS) and the on-board Phased Array L-band Synthetic Aperture Radar (PALSAR) instrument, synthetic aperture radar (SAR) data at L-band have become available with a relatively wide bandwidth. Depending on the acquisition mode, the sensor's range chirp bandwidth can be as high as 28 MHz. However, in high solar conditions, ionospheric path delays and Faraday rotation (FR) become significant for wide-bandwidth SAR applications [6]; the use of large chirp-bandwidths is susceptible to signal degradation that can result in a sub-optimal resolution and FR may distort or even destroy important information otherwise available from polarimetric SAR data.

A preliminary study was directed towards how the influence of the ionosphere on SAR becomes significant at low frequencies starting at L-band and lower, and how signal degradation caused by the ionized ionosphere increases with larger chirp bandwidths [2,3]. The aim here is the development and description of algorithms and system models estimating ionospheric FR of electromagnetic waves from quad-polarized SAR data. Raw or focused radar images can be used for the estimation. Based on simulations and proven with real PALSAR data, the algorithms are based on known techniques for ionospheric total electron content (TEC) measurements. The electron content is responsible for FR [6]. Additional influences of ionospheric TEC such as path delays and signal reception degradation are considered for the simulations and discussed also in the real data. Once FR and TEC are known, fully polarimetric data sets can be calibrated and used for polarimetric SAR analyses. Resolution degradations may also be corrected.

The potential of low-frequency SAR with ionospheric path delays and FR for TEC measurements has been recognized in [2, 5]. FR effects have been discussed at length in [6–8]. Corrective methods were treated, e.g., in [9]. Distortion effects are laid out in [10], [9], [10]. Detection and estimation techniques based on quad-polarized data are presented in [6,11,12]. A good estimation aids and improves general polarimetric calibration and validation techniques such as given in [14, 15] to make spaceborne polarimetric measurements trustworthy for biomass classification and retrieval [16, 17]. In [18], a first analysis of PALSAR data considering FR detection is presented.

In Section 3.2, the theoretical background of the ionospheric influences on electromagnetic waves is outlined. Section 3.3 introduces the algorithms used for the simulation of spaceborne SAR data of a point target, including quad-polarization and FR. The influence of frequency-dependent radar chirp path delays is explained and added to the simulation. The simulations are carried out for typical L- and P-band sensor configurations. For the estimation of FR, the approach of frequency-dependent rotation of a linearly polarized wave is applied. The simulations are based on point targets, exploiting the information from quad-polarized data, and are performed using techniques proposed in [6]. Investigations discuss the suitability of raw, range-compressed (RC), and azimuth-compressed (AC) data for FR estimation. Empirical results obtained from PALSAR scenes are shown in Section 3.4 together with the calibration steps necessary to acquire them correctly.

Simulated and real data are compared and discussed in Section 3.5. Possible methods for properly validating the approaches are suggested. A conclusion with a summary of results, possible improvements and directions for further research is given in Section 3.6.

3.2 Effects of the Ionosphere

Electromagnetic waves propagating through the ionosphere experience a polarisation rotation of the electric field vector and a signal path delay that depends on the number of free electrons N_e along the ray path, the signal frequency f, and the strength of the magnetic field parallel to the propagation direction of the wave within the ionized layer. Entering an ionized medium, a linearly polarized wave can be regarded as a superposition of two separate counter-rotating circular polarized waves, traveling on slightly different paths with different velocities. Leaving the ionized medium, these waves recombine with a resulting polarisation that is dependent on these propagating effects. The two-way propagation from a satellite to the Earth and back does *not* compensate for this effect. The effect is cumulative: FR *doubles*, as does the path delay [3].

3.2.1 The Earth Magnetic Field and Free Electrons in the Ionosphere

A widely used model for the estimation of the geomagnetic field of the Earth is the International Geomagnetic Reference Field model (IGRF). The latest version is the 10^{th} generation of the model and was released by the International Association of Geomagnetism and Aeronomy (IAGA) [23]. It is described mathematically by a series of spherical harmonics, the coefficients of which are estimated to order 13. The main field can be approximated as a dipole centered within the Earth and caused by electric currents within the Earth. The magnetic field is therefore modeled as the negative gradient of the potential V, and can be written as [23]

$$V(r,\theta,\psi,t) = R\sum_{n=1}^{n_{\max}}(\frac{R}{r})^{n+1}\sum_{m=0}^{n}(g_n^m(t)\cos(m\psi) + h_n^m(t)\cdot\sin(m\psi))P_n^m(\theta) \tag{3.1}$$

where r is the distance from the center of the Earth, θ is the colatitude (i.e., $90° - $latitude), ψ is the longitude, R is the reference radius of the Earth, $g_n^m(t)$ and $h_n^m(t)$ are the field coefficients at time t, and $P_n^m(\theta)$ are the Schmidt semi-normalized associated Legendre functions of degree n and order m.

The model's coefficients of the spherical harmonic vary in time. Their period of validity is normally set to 5 years. More details on main-field modeling can be found in [20, 21]. Fig. 3.1 shows a plot of the nadir component relative to the Earth's center of the global magnetic field as modeled by the IGRF10 for June 21, 2007.

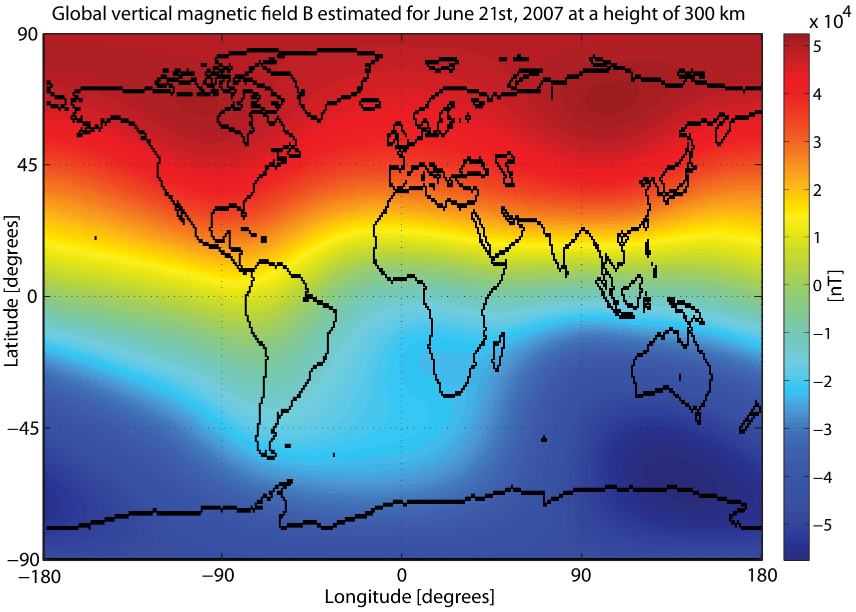

Figure 3.1: Effective component of the geomagnetic field for a nadir-looking sensor. Magnetic field as modeled by the IGRF10 for June 21, 2007.

3.2.2 FR

The polarisation rotation of the E-field vector of an electromagnetic wave traveling through the ionosphere is called FR as mentioned in the introduction. It depends on the total electron content along the ray path, its wavelength, and the Earth's magnetic field. From Fig. 3.1, it may be seen that there is no FR at the geomagnetic equator for a nadir looking sensor configuration. If the geomagnetic field is not zero, the wavelength-dependency of FR causes the low-frequency parts of a received radar chirp to be more strongly rotated than high-frequency parts. As a result, a single-polarized sensor configuration will receive—discernible for a point target—an apparently frequency-dependent change in amplitude of the transmitted chirp in the presence of FR.

Generally, FR depends on the total electron content and the magnetic field along the path and may be estimated from [7,9] as

$$\begin{aligned} \Omega &= \frac{2.365 \cdot 10^4}{c^2} \cdot \lambda^2 \cdot B_{||} \int_0^h N_e \ dh \\ &\approx \frac{2.365 \cdot 10^4}{f^2} \cdot \mathrm{VTEC} \cdot \frac{1}{\cos\gamma} \cdot B_{||} \end{aligned} \tag{3.2}$$

where $B_{||}$ is the mean parallel magnetic field in the line-of-sight of the sensor within the ionized layer, c the speed of light, λ the wavelength of the radar wave, VTEC the vertical total electron content and γ the off-nadir angle of the observation. The factor $1/\cos\gamma$

converts the vertical electron content to the electron content along the ray path. The commonly used zenith angle of the radar wave at the sub-ionospheric point was therefore approximated by the satellite's off-nadir angle. VTEC may be estimated using global ionospheric maps (GIM) from the Center for Orbit Determination in Europe (CODE) [22]. γ may be obtained for each image location in a product from the sensor data annotations for most currently active SAR satellites. Finally, the parallel magnetic field was obtained at a height of 300 km from the IGRF10 model presented in the previous Section 3.2.1. As the strength of geomagnetic field varies slowly at ionospheric heights, a reference mean value is commonly estimated for a set reference height between 300 km and 450 km [9].

3.2.3 Chirp Signal Path Delay

According to Hanssen [24], electromagnetic waves propagating through the ionosphere are delayed by

$$\Delta t_{\text{iono}} = \frac{K}{c} \cdot \frac{\text{TEC}}{f_c^2} \tag{3.3}$$

where TEC is the total electron content along the signal path and $K = 40.28\frac{\text{m}^3}{\text{s}^2}$ is a refractive constant. This means that for a down-chirp (e.g., PALSAR chirp) and a two-way propagation from satellite to Earth and back, the pulse is shifted between

$$t_{\text{shift\_min}} = \frac{2}{c}\, K \cdot \frac{\text{TEC}}{f_{\text{start}}^2} \tag{3.4}$$

$$t_{\text{shift\_max}} = \frac{2}{c}\, K \cdot \frac{\text{TEC}}{f_{\text{stop}}^2}. \tag{3.5}$$

For a linearly frequency modulated chirp, these shifts imply a change in the chirp rate and, therefore, a change in the length of the transmitted pulse. In a precise simulation of TEC influence on SAR signals, this behavior of the ionosphere must be considered by including the $t_{\text{shift\_min}}$ in the received signal. Because of the frequency-dependent path delays, given high ionospheric conditions, also a modified chirp rate replaces the transmitted chirp rate in the received pulse. Fig. 3.2 illustrates these effects including the shifts in range and the modified chirp rate. T_{p} is the pulse duration of the transmitted chirp and $T_{\text{p\_iono}}$ is the new pulse duration of the chirp after passing the ionosphere (two-way). Because the phase refractive index of a radio wave in the ionosphere is less than unity, a two-way phase advance at center frequency f_c relative to that in free space may be estimated as

$$\phi_{\text{ph}} \approx \frac{2K}{cf_c^2} \cdot \text{TEC}. \tag{3.6}$$

Finally, the rate of change of phase with respect to frequency, also known as the phase dispersion, $\phi_r(f)$, i.e., the residual phase function at frequency f caused by the non-turbulent ionosphere, may be modeled as [24]:

$$\phi_r(f) \approx \frac{4\pi K}{cf_c^3} \cdot \text{TEC}(f - f_c)^2. \tag{3.7}$$

Local or traveling ionospheric disturbances (TIDs) that are difficult to foresee may also play a role [3]. Because of the limited spatial area affected, they influence the standard deviation of a scene measurement of TEC and FR, but otherwise only pose a problem for pointwise applications like SAR interferometry [7].

In summary, signal FR and path delays caused by the ionosphere depend on the chirp bandwidth and increase at lower carrier frequencies. Table 3.1 shows the influence of the ionosphere at 50 and 100 TEC units (1 TECU $= 1 \times 10^{16} m^{-2}$) based on calculations from the above theory for the TerraSAR X and ALOS PALSAR systems as well as a possible configuration of a P-band spaceborne sensor. Calculations of amplitude variations refer to Section III-C.

3.3 Simulations

Compared to TEC values *normally* found in the ionosphere, the numbers listed in Table 3.1 are quite high. However, these values highlight the phenomena they cause, especially when the phenomena are subtle. Simulations made using a range of TEC values are presented in the following together with the necessary detailed simulation background and process explanations.

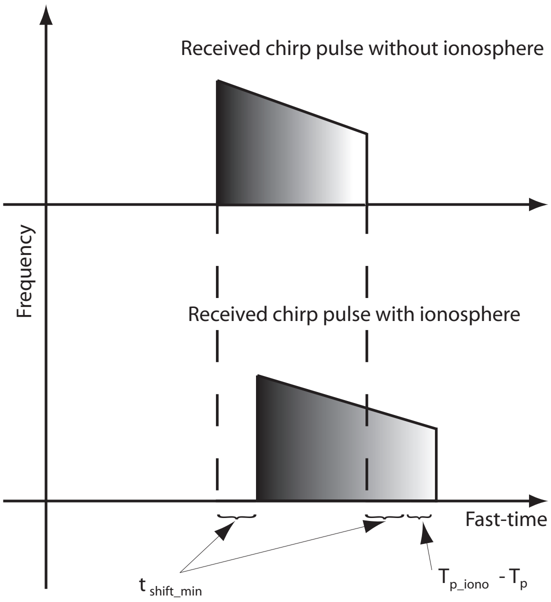

Figure 3.2: (Top) Received chirp pulse without and (bottom) including ionospheric effects.

Sensor	**TSX**		**PALSAR**		**P-band**	
Frequency (f_c) [GHz]	9.65		1.27		0.45	
Bandwidth (B) [MHz]	max. 300		max. 28		6	
Chirp duration [μsec]	40*		27		27	
Sampling rate [MHz]	max. 330		max. 32		8	
Chirp form	up		down		down	
Orbit (altitude) [km]	514		695		695	
TEC [TECU]	50	100	50	100	50	100
Path delay at f_c [m]	0.5	1	27	54	218	436
Change in chirp length for B [$n$sec]	-0.1	-0.2	4	8	19.4	38.7
Faraday rotation at f_c [°]	0.5	1	29.5	59	235	470
Δ FR within chirp [°]	0.03	0.06	1.3	2.6	6.3	12.5
$\varnothing$ Amplitude variation (M_{hh}) [dB]	-44	-38	-8.9	-3.1	-2.0	-1.3
Δ Amplitude within chirp (M_{hh}) [dB]	-53	-47	-19.5	-14.1	-10.5	-6.9

*Chirp duration for TerraSAR-X estimated using typical conversion factors based on PRF.

Table 3.1: Satellite sensor details and estimates (two-way) of influence of 50 and 100 TECU on the path delay, chirp length and FR for TerraSAR-X (TS-X), ALOS PALSAR, and a possible future spaceborne P-band sensor configuration. The Earth's magnetic field is modeled for June 21, 2007, 45° north and 0° east at a height of 300 km and a nadir-looking sensor configuration.

3.3.1 Chirp Signal Path Delay

Under high ionospheric conditions, visible differences in the SAR raw data result mainly in a slant range (fast time) positional shift. Relevant changes appear when correlating the received pulses with a replica of the transmitted chirp in order to perform pulse compression—a matched filter operation, where best compression of the pulses is achieved when the transmitted and received pulses match perfectly. In the time domain, matched filtering of the pulse corresponds to a convolution of the received chirp $s(t)$ with the complex conjugate $p^*(t)$ of the transmitted chirp, providing the desired compressed return echo

$$\begin{aligned} s_M(t) &= s(t) \otimes p^*(t) && (3.8)\\ &= \mathcal{F}^{-1}\{S(w) \cdot P^*(w)\} && (3.9) \end{aligned}$$

where $\otimes$ denotes a convolution and * the complex conjugate operator. Using this information and the theory presented in Section 3.2.3, the duration of the received pulse may be estimated as

$$T_{p\_\mathrm{iono}} = T_p \pm \frac{2}{c} \cdot K \cdot \mathrm{TEC} \cdot \left(\frac{1}{(f_c - f_0)^2} - \frac{1}{(f_c + f_0)^2} \right) \tag{3.10}$$

depending (in contrast to the transmitted chirp) additionally on the TEC value. f_0 denotes the half chirp bandwidth. The corresponding chirp rate is

$$\alpha_{\mathrm{iono}} = \frac{f_0}{T_{p\_\mathrm{iono}}}. \tag{3.11}$$

The expected form of the received chirp under the influence of the ionosphere can be written as

$$s_{\mathrm{iono}} = e^{j2\pi(f_{\mathrm{start}} \cdot t_{d0} - \alpha_{\mathrm{iono}} \cdot t_{d0}^2)} \tag{3.12}$$

where t_{d0} is a time vector depending on the sensor's sampling rate and the range to the target Y_c according to

$$t_{d0} = \frac{2Y_c}{c} + (0 : n-1) \cdot \frac{1}{f_s} + \Delta t_{d0} \tag{3.13}$$

$$\Delta t_{d0} = 2 \cdot (0 : n-1) \cdot \frac{K \cdot TEC}{(f_c \pm f_0)^2} \cdot c \tag{3.14}$$

where Δt_{d0} includes the frequency-dependent behavior of the chirp. The "±" derives from the choice of down- vs. up-chirp. n is an integer satisfying the condition

$$(n-1) \cdot \frac{1}{f_s} \leqslant T_{p\_\mathrm{iono}}. \tag{3.15}$$

In the following simulations, the raw data were estimated using a standard system model proposed in Ch. 6 of [25] with an antenna beam pattern dependent mainly on the center frequency and the physical antenna length. Without loss of generality, we assume that any antenna gain-dependent effects on the SAR signal have been corrected and removed from the SAR data. The standard system model has been extended to include all ionospheric effects discussed in Section 3.2, including time and phase shifts of the chirp due to the non-turbulent ionosphere, but TID and non-equal antenna gains of different polarizations are left out of the simulation, as they would not add significant information. Azimuth compression was performed using the ω-k algorithm. For detailed information on the SAR focusing steps, the reader is referred to [25] and [25].

3.3.2 FR Simulation

All independent channels of a multi-polarized SAR are affected by FR in the same way. Therefore, a single model for these effects is sufficient. An approach described in [14] is used here to retrieve the measured scattering matrix $\mathbf{M_0}$. It may be written as

$$\mathbf{M_0} = Ae^{j\varphi}\mathbf{R}^T\mathbf{R}_F\mathbf{S}\mathbf{R}_F\mathbf{T} + \mathbf{N} \tag{3.16}$$

where $\mathbf{S}$ is the scattering matrix, $\mathbf{R}$ and $\mathbf{T}$ are the receive and transmit distortion matrices, $\mathbf{N}$ is additive noise, A the amplitude of the received pulse after the matched filter, $e^{j\varphi}$ the signal phase and $\mathbf{R}_F$ the one-way FR matrix. As the focus here lies on FR, in the forgoing, the parameters $e^{j\varphi}$, A, $\mathbf{T}$, and $\mathbf{R}$ can be independently calibrated: Within the simulation, calibration errors are not modeled [12]. In our simulation, $\mathbf{N}$ varies from zero for an ideal case, to -30 dB, corresponding to reasonable PALSAR noise equivalent sigma zero (NESZ) values for polarimetric mode [27]. Under ideal conditions, equation (3.16) simplifies to:

$$\mathbf{M} = \mathbf{R}_F \mathbf{S} \mathbf{R}_F \tag{3.17}$$

or

$$\begin{bmatrix} M_{\mathrm{hh}} & M_{\mathrm{vh}} \\ M_{\mathrm{hv}} & M_{\mathrm{vv}} \end{bmatrix} = \begin{bmatrix} \cos\Omega & \sin\Omega \\ -\sin\Omega & \cos\Omega \end{bmatrix} \cdot \begin{bmatrix} S_{\mathrm{hh}} & S_{\mathrm{vh}} \\ S_{\mathrm{hv}} & S_{\mathrm{vv}} \end{bmatrix} \cdot \begin{bmatrix} \cos\Omega & \sin\Omega \\ -\sin\Omega & \cos\Omega \end{bmatrix}. \tag{3.18}$$

Under backscatter alignment conditions, (3.18) can be written as

$$\begin{aligned} M_{\mathrm{hh}} &= S_{\mathrm{hh}}\cos^2\Omega - S_{\mathrm{vv}}\sin^2\Omega + (S_{\mathrm{hv}} - S_{\mathrm{vh}})\sin\Omega\cos\Omega \\ M_{\mathrm{vh}} &= S_{\mathrm{vh}}\cos^2\Omega + S_{\mathrm{hv}}\sin^2\Omega + (S_{\mathrm{hh}} + S_{\mathrm{vv}})\sin\Omega\cos\Omega \\ M_{\mathrm{hv}} &= S_{\mathrm{hv}}\cos^2\Omega + S_{\mathrm{vh}}\sin^2\Omega - (S_{\mathrm{hh}} + S_{\mathrm{vv}})\sin\Omega\cos\Omega \\ M_{\mathrm{vv}} &= S_{\mathrm{vv}}\cos^2\Omega - S_{\mathrm{hh}}\sin^2\Omega + (S_{\mathrm{hv}} - S_{\mathrm{vh}})\sin\Omega\cos\Omega \end{aligned} \tag{3.19}$$

In our simulation, we consider reflection symmetry, where we assume a constant signal return amplitude $B = S_{\mathrm{hv}} = S_{\mathrm{vh}}$. This reduces (3.19) to

$$\begin{aligned} M_{\mathrm{hh}} &= S_{\mathrm{hh}}\cos^2\Omega - S_{\mathrm{vv}}\sin^2\Omega \\ M_{\mathrm{vh}} &= B + (S_{\mathrm{hh}} + S_{\mathrm{vv}}) \cdot \sin\Omega\cos\Omega \\ M_{\mathrm{hv}} &= B - (S_{\mathrm{hh}} + S_{\mathrm{vv}}) \cdot \sin\Omega\cos\Omega \\ M_{\mathrm{vv}} &= S_{\mathrm{vv}}\cos^2\Omega - S_{\mathrm{hh}}\sin^2\Omega \end{aligned} \tag{3.20}$$

which in the case of a trihedral corner reflector (TCR). A point target with $A = S_{\mathrm{hh}} = S_{\mathrm{vv}}$ can be rewritten as

$$\begin{aligned} M_{\mathrm{hh}} &= A \cdot \cos 2\Omega \\ M_{\mathrm{vh}} &= B + A \cdot \sin 2\Omega \\ M_{\mathrm{hv}} &= B - A \cdot \sin 2\Omega \\ M_{\mathrm{vv}} &= A \cdot \cos 2\Omega. \end{aligned} \tag{3.21}$$

By using the aforementioned assumptions for calibration and TCR measurements, the backscatter behavior is implemented as described in (3.21) with noise added in the non-ideal case. For simplicity, the amplitude A was set to 1 and B to zero, corresponding to the backscatter behavior of an ideal TCR.

3.3.3 Chirp Amplitude Variations Because of FR

The chirp amplitude variation caused by FR is also modeled in the simulation. The single-polarized amplitude is used to model the received pulse subject to Faraday rotation. For a single channel, e.g., HH, the received pulse is modeled with (3.12) and (3.21) as

$$s_{\mathrm{FR}} = M_{\mathrm{hh}} \cdot e^{j2\pi(f_{\mathrm{start}} \cdot t_{d0} - \alpha_{\mathrm{iono}} \cdot t_{d0}^2)}. \tag{3.22}$$

Because M_{hh} depends on the FR angle Ω, which, in turn, depends on the frequency f, a frequency-dependent amplitude variation is to be expected. At L-band—under the PALSAR system parameters and NESZ assumptions—the expected frequency-dependent change in amplitude might not be detectable at TEC levels below 15 TECU. The reason becomes clear if one thinks about the small change of FR angles within the typical 14 MHz range bandwidth of quad-polarized PALSAR data. An attenuation would, however, be clearly observable with a spaceborne P-band system. The results from Table 3.1 show that under higher ionospheric conditions and at lower frequencies, amplitude variations within a chirp can rise to above the noise level and degrade the image quality.

The change in FR $\Delta\Omega$ within the chirp bandwidth may be estimated from single-polarized data using (3.21)

$$\begin{aligned}
\Omega_1 &= \frac{1}{2}\arccos\left(\frac{M_{\mathrm{hh}_1}}{A}\right) && (3.23)\\
\Omega_2 &= \frac{1}{2}\arccos\left(\frac{M_{\mathrm{hh}_2}}{A}\right) && (3.24)\\
\Delta\Omega &= \Omega_1 - \Omega_2 && (3.25)\\
&= \frac{1}{2}\left(\arccos\frac{M_{\mathrm{hh}_1}}{A} - \arccos\frac{M_{\mathrm{hh}_2}}{A}\right). && (3.26)
\end{aligned}$$

where M_{hh_1} and M_{hh_2} are the amplitudes of the chirp at its respective start and stop frequencies. Low sampling rates can distort the accuracy of the measurements of both amplitudes by misestimating the location of the maxima. Measurement of the *difference* of the amplitudes removes the necessity to estimate the absolute value of the amplitudes M_{hh_1} and M_{hh_2}. The relative difference in amplitude can be obtained from the mean gradient within the amplitudes and the chirp bandwidth. It is therefore probably more accurate to calculate $\Delta\Omega$ from the difference in amplitude $\Delta A = M_{\mathrm{hh}_1} - M_{\mathrm{hh}_2}$ within the chirp. Using a series expansion for the arccos-function

$$\begin{aligned}
\arccos x &= \frac{\pi}{2} - \Big[x + \frac{x^3}{2\cdot 3} + \frac{1\cdot 3x^5}{2\cdot 4\cdot 5} + \frac{1\cdot 3\cdot 5x^7}{2\cdot 4\cdot 6\cdot 7} + \cdots\\
&\quad + \frac{1\cdot 3\cdot 5\cdots(2n-1)x^{2n+1}}{2\cdot 4\cdot 6\cdots(2n)(2n+1)} + \cdots\Big]\\
&\quad \text{for all } |x| < 1 \in \mathbb{R} && (3.27)
\end{aligned}$$

and (3.26) as

$$\begin{aligned}2\Delta\Omega &= \frac{\pi}{2} - \left[\frac{M_{\mathrm{hh}_1}}{A} + \frac{M^3_{\mathrm{hh}_1}}{6A^3} + \frac{3M^5_{\mathrm{hh}_1}}{40A^5} + \cdots\right] \\ &\quad -\frac{\pi}{2} + \left[\frac{M_{\mathrm{hh}_2}}{A} + \frac{M^3_{\mathrm{hh}_2}}{6A^3} + \frac{3M^5_{\mathrm{hh}_2}}{40A^5} + \cdots\right] \\ &\quad \text{for all } \left|\frac{M_{\mathrm{hh}_1}}{A}\right|, \left|\frac{M_{\mathrm{hh}_2}}{A}\right| < 1 \in \mathbb{R}. \end{aligned} \tag{3.28}$$

Neglecting terms of higher order reduces (3.28) to

$$\Delta\Omega \approx \frac{M_{\mathrm{hh}_2} - M_{\mathrm{hh}_1}}{2 \cdot A} = \frac{-\Delta A}{2 \cdot A}. \tag{3.29}$$

3.3.4 FR Extraction

There exist a number of methods for the extraction of FR from quad-polarized data. The most well known are given in [6, 12]. The approach described in [6] is the most robust because it estimates FR using the phase between the cross-polarized (left/right) circular states. It was used throughout our investigations.

For simulated data, the algorithm presented in [12] would work as well, and is easier to implement. It defines the two-way FR by observing that:

$$\Omega_{2-\mathrm{way}} = 2 \cdot \frac{1}{2} \arctan\left[\frac{(M_{\mathrm{vh}} - M_{\mathrm{hv}})}{(M_{\mathrm{hh}} + M_{\mathrm{vv}})}\right]. \tag{3.30}$$

Similarly, the circular cross-pol method [6] states that:

$$\Omega_{2-\mathrm{way}} = 2 \cdot \frac{1}{4} \arg(Z_{12} Z^*_{21}) \tag{3.31}$$

with

$$\left[\begin{array}{cc} Z_{11} & Z_{12} \\ Z_{21} & Z_{22} \end{array}\right] = \left[\begin{array}{cc} 1 & j \\ j & 1 \end{array}\right] \cdot \left[\begin{array}{cc} M_{\mathrm{hh}} & M_{\mathrm{vh}} \\ M_{\mathrm{hv}} & M_{\mathrm{vv}} \end{array}\right] \cdot \left[\begin{array}{cc} 1 & j \\ j & 1 \end{array}\right].$$

The results from the method described in [6] can easily be analyzed using the simulation model developed above. To allow comparison with results in the following Section 3.4, the PALSAR system parameters listed in Table 3.1 were used. However, simulations were done with 14-MHz bandwidth, as PALSAR does not support higher bandwidths in polarimetric mode [28]. Noise with a level of -30 dB was added to each channel. Simulations were conducted at 20 TECU, a reasonable value at average solar conditions. Equation (3.2) indicates that 20 TECU induce a FR angle of 11.812° at $f = f_c = 1.27$ GHz, and the Earth's magnetic field $B_{||}$ is modeled at a height of 300 km for June 21, 2007, 45° North and 0° East. The peak of the focused point target in the simulation is at 20 dB.

Fig. 3.3 shows the results of an analysis of simulated raw data. In Fig. 3.3(a), the FR values over the complete scene are shown calculated with (3.31). Where a chirp signal is

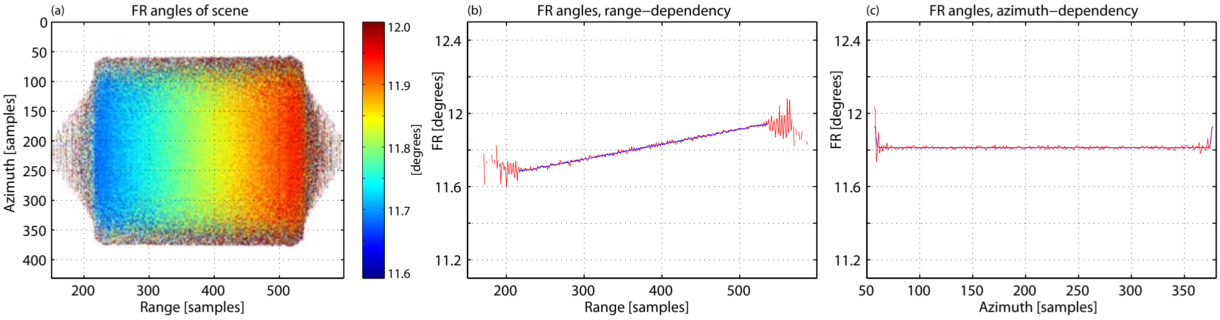

Figure 3.3: FR analysis on simulated *PALSAR* ***raw*** *data of a TCR at scene center for 20 TECU. In (a), the FR values of the received quad-polarized signal from the TCR are calculated with (3.31). FR varies between 11.68 and 11.94°. In (b) and (c), the mean range and azimuth profiles, respectively, are plotted. Blue: Without noise. Red: NESZ = -30 dB added.*

present, FR varies between 11.68 and 11.94°, as predicted in theoretical calculations. As this is only a single point target, the variations are due to the change of frequency *inside* the chirp, not to slant range or off-nadir angle variations (constant for a single stationary TCR on the ground). The influence of noise is very visible at the border of the chirp signal. The retrieved mean FR angle was $\Omega_\varnothing = 11.8132°$ with a standard deviation of $\sigma_\Omega = 0.16774°$ (no noise: $\sigma_\Omega = 0.07531°$). An almost uniform distribution of values is observed, caused by the characteristics of the chirp passing over a single TCR. An SNR threshold was applied in the figure, discarding values in Fig. 3.3(a) below a 5% limit of peak signal power. In the following, we compare compressed signals where the noise level of images increases due to the nonideal matched filtering. In Fig. 3.3(b) and (c), the range and azimuth profiles are plotted. Some border effects are observable. The edge effect in Fig. 3.3(c) is caused by variations in the aperture length which is always slightly longer in far-than-in-near range. Values retrieved from simulations without added noise are plotted for comparison, indicated in blue.

Similar results from the RC data derived from the raw data of Fig. 3.3 are shown in Fig. 3.4. Due to the compression, the signal in Fig. 3.4(a) is much more compact, clearly showing the SAR-typical azimuth characteristics of a dwell-time smearing in azimuth, typically focused later in azimuth-compression. Power thresholding was applied to improve the image's SNR. FR estimates are much closer to a single value in Fig. 3.4(a) than in Fig. 3.3(a). The mean value of FR measured from the noised data is $\Omega_\varnothing = 11.8145°$ with a standard deviation of $\sigma_\Omega = 0.02348°$. After range compression in Fig. 3.4(b), one sees that the range dependency is completely lost. The standard deviation without noise yields $\sigma_\Omega = 0.00327°$. Azimuth dependence in Fig. 3.4(c) again shows constant characteristics.

The AC data of the same TCR as in Figs. 3.3 and 3.4 are presented in Fig. 3.5. As before, in Fig. 3.5(a) the FR values for the complete scene are shown with the same power threshold applied. Areas with very weak backscatter, that become visible after azimuth compression, are removed. Still, there remain large regions in the scene where a signal

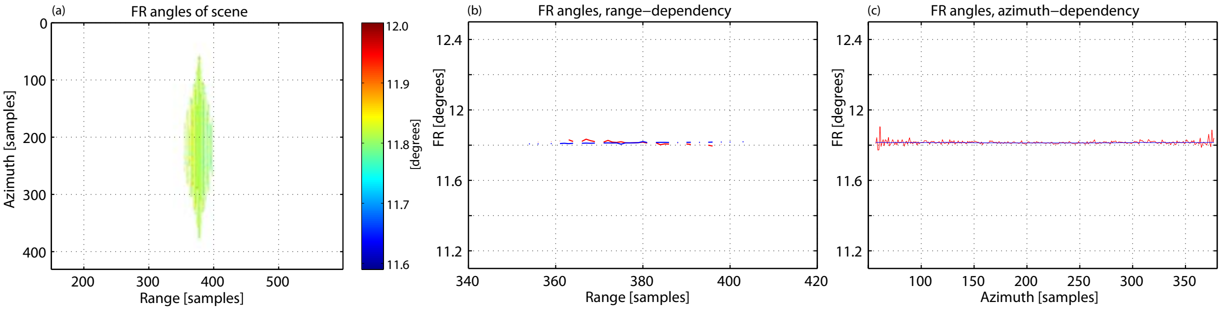

Figure 3.4: FR analysis on simulated *PALSAR **RC** data of a TCR at scene center for 20 TECU. In (a), the FR values of the quad-polarized and compressed signal are calculated with (3.31). Areas with no signal are masked out. In (b) and (c), the mean range and azimuth profiles, respectively, are plotted. Blue: Without noise. Red: NESZ = -30 dB added.*

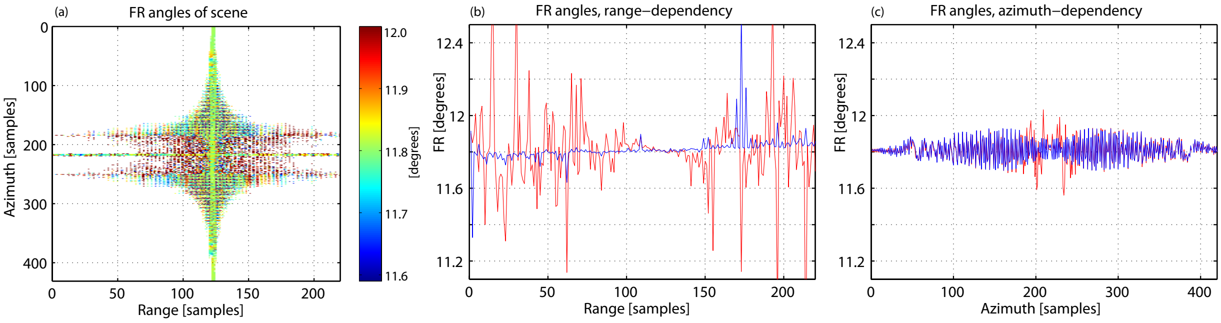

Figure 3.5: FR analysis on simulated *PALSAR **AC** data of a TCR at scene center for 20 TECU. In (a), the FR values of the quad-polarized and compressed signal are calculated with (3.31). Areas with no signal are masked out. The mean range and azimuth profiles are plotted in (b) and (c). Blue: Without noise. Red: NESZ = of -30 dB added.*

is present and where FR analysis may be applied. The results are consistent with those shown for the RC and raw data scene. However, as may be seen in Fig. 3.5(b), the simulations including noise produce retrievals that oscillate around the mean value (red line), whereas the ideal data gives an almost constant value of FR over range (blue line). The calculated mean FR is $\Omega_{\varnothing} = 11.8091°$ with a standard deviation of $\sigma_{\Omega} = 0.52256°$ with noise ($\sigma_{\Omega} = 0.12383°$ no noise). This is confirmed by the azimuth trend of a cut through the TCR that shows a constant value with a large standard deviation. The variation is reduced if a threshold is chosen that cuts off more of the signal. The signal of an AC simulated TCR has a high peak power value at its focal point and only low signals (sidelobes) around it.

For a more meaningful comparison with real data measurements, a set of 100 simulated TCRs was investigated under mean ionospheric conditions of 20, 50, and 100 TECU and for two different noise levels (-30 and -25 dB). TEC was therefore modeled to be range dependent. The amplitudes ($S_{\mathrm{hh}} = S_{\mathrm{vv}}$) of the TCRs were randomly set between zero

	NESZ	**-30 dB**		**-25 dB**	
TEC	**Data**	$\varnothing$FR[$^\circ$]	$\sigma_\Omega[^\circ]$	$\varnothing$FR[$^\circ$]	$\sigma_\Omega[^\circ]$
20 [TECU]	RAW	11.83	0.07	11.83	0.09
	RC	11.87	0.06	11.87	0.07
	AC	11.87	0.18	11.87	0.33
50 [TECU]	RAW	29.56	0.18	29.56	0.18
	RC	29.68	0.12	29.68	0.13
	AC	29.66	0.31	29.66	0.42
100 [TECU]	RAW	59.13	0.35	59.13	0.35
	RC	59.35	0.27	59.35	0.27
	AC	59.30	0.87	59.30	0.91

Table 3.2: Results of two-way FR and standard deviation for simulated PALSAR raw, RC and, AC data under ionospheric conditions of 20, 50, and 100 TECU. Simulation was done for 100 TCRs with random amplitudes between 0 and 1 and two noise levels.

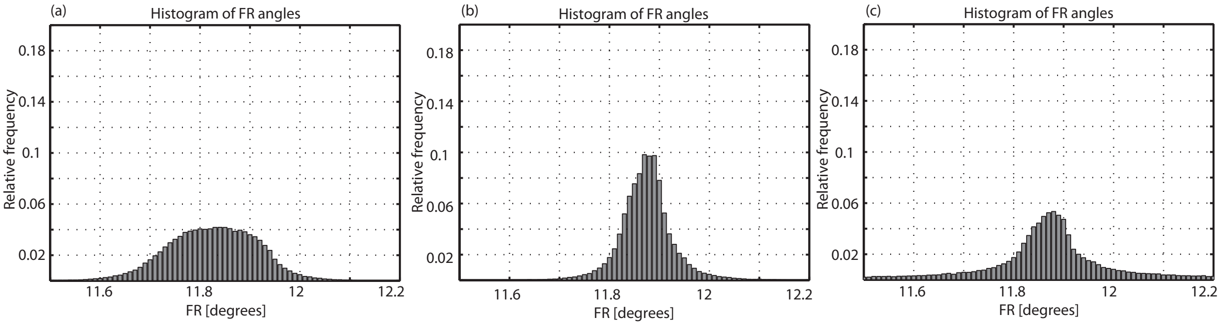

Figure 3.6: Comparison of FR histograms from simulated *PALSAR data of 100 TCRs at a mean TEC level of 20 TECU and -25 dB NESZ. (a) FR values from the* raw *data. (b) FR values from the RC data. (c) FR values from the AC data.*

and one. Table 3.2 shows extracted two-way FR values and related standard deviations. Fig. 3.6 shows an example of the histograms of the extracted FR angles under mean ionospheric conditions of 20 TECU and a noise level of -25 dB. The histogram shows the results in Fig. 3.6(a)-(c) for the raw, the RC, and AC data, respectively. The mean extracted FR angles from the data are (a) $\Omega_\varnothing = 11.826^\circ$, (b) $\Omega_\varnothing = 11.874^\circ$, and (c) $\Omega_\varnothing = 11.87^\circ$. The standard deviations are estimated to be (a) $\sigma_\Omega = 0.089^\circ$, 0.066°, and 0.332°, respectively.

Compared to the single TCR simulations, the spread of FR in the RC data is again lowest, but differences between the raw and RC become smaller. The spread of FR retrievals is highest for the fully focused data. Moreover, the mean value of the focused data is slightly increased in comparison to the raw data. The differences in extracted FR between the raw and focused data are again due to the nonideal focusing operations caused mainly by the frequency-dependent modifications of the chirp under ionospheric conditions. FR estimation from simulations at higher TEC levels increase correspondingly (see Table 3.1). The influence of noise on the variation in FR angles is most relevant at lower TEC levels.

In P-band simulations, stronger FR dependency in range on the raw data is expected to be observed because of the larger relative change of frequencies inside the bandwidth relative to the center frequency.

3.4 ALOS PALSAR Data

After reviewing theoretical considerations with simulations, the step from simulations to real data measurements is a natural goal. With PALSAR, the first spaceborne system is operational where FR can significantly influence polarimetric measurements. The challenges of measuring FR from real data are a correct calibration of the polarimetric channels as well as background clutter, speckle, and the systematic noise sources.

3.4.1 Calibration and Validation

PALSAR was specifically designed to be a polarimetric SAR system. Its engineers therefore took great care to ensure that the antenna gain pattern could be consistently calibrated across all channels with the help of PALSAR antenna gain files [28]. Assuming stationarity, polarimetric calibration with preservation of the FR can be achieved by applying calibration parameters estimated within a scene known to have very low expected FR. The parameters can be estimated via the aforementioned algorithms or taken directly from Japan Aerospace Exploration Agency (JAXA) level 1.1 single look complex products. The integration of polarimetric calibration in the FR estimation based on SAR data was made using standard reference values from JAXA. The FR estimates were averaged over a rectangular area (according to projected range and azimuth resolutions).

For the estimation of the FR from the Global Navigation Satellite System (GNSS) TEC maps, the magnetic field was simulated at the scene center using the IGRF10 model for a height of 300 km. FR angles in the slant direction were estimated using the nadir component of the magnetic field and the vertical TEC over the scene center mapped by the satellite's off-nadir angle. Bihourly TEC maps sampled every 2.5° in latitude and 5.0° in longitude were interpolated to 1° resolution and temporally to the corresponding sense time between two consecutive TEC maps. The accuracy of the TEC maps over regions with high GPS receiver density (e.g., Europe) is advertised to be in the range of ± 3-4 TECU [29].

3.4.2 FR Measurement

Examining a set of 15 fully polarimetric ALOS PALSAR scenes from -10 to 50° latitude, expected two-way FR from the simulations ranges from 0.82° to 14.2°. Fig. 3.7 shows the two-way FR measurements from a dataset where higher FR were expected from the TEC maps and the IGRF10 model. Values that are below a 5% limit of peak signal power and that are over a 95% limit of peak signal power were masked out (marked in dark blue). The colorbar for FR over the scene in Fig. 3.7(a) is also valid for the scenes in Fig. 3.7(c), (e), and (g). Fig. 3.7(b), (d), and (f) shows normalized histograms corresponding to the FR scene on their left. Fig. 3.7(g) shows the FR angles of the azimuth focused scene with values below a 80% limit of peak signal power masked out. Fig. 3.7(h) compares the amplitudes of the focused image. The behavior of these results is generally representative for all examined PALSAR scenes. Comparing the FR estimations from the raw [Fig. 3.7(a) and (b)], RC [Fig. 3.7(c), (d)], and AC [Fig. 3.7(e), (f)] data with the simulations, the same trends can be observed. FR from the raw data is closer to the trend of the simulations than the FR from the RC and AC data as the raw data better fit the simulations than the focused data. The FR from the RC data is as in the simulations usually higher than the FR from the AC data. The broadness of the distribution of the real data increases with every compression step. From the simulations, we were able to observe this trend only with regard to the AC data. Standard deviations of raw and RC data from simulations of 100 TCRs became nearly identical.

Fig. 3.7(e) shows that areas where FR is undefined (colored in dark blue) or highly variable are typically dark regions such as lakes and mountainous backslope areas. No range and azimuth profiles are shown in Fig. 3.7, as in a large and complex scene; they only emphasize the variations and do not otherwise provide any useful information (assuming that ionospheric variations within the SAR image can be neglected). At L-band frequencies given the observed variations, it is not feasible to extract any range-dependent FR from the range profile for the available data sets. For the raw data, not even the frequency dependence of FR within the chirp in a range profile can be shown (as analog to Fig. 3.3), as all frequencies overlap at every point in space. Therefore, the extracted FR angles from the raw data are influenced by the FR of all contributing scatterers within that pixel and are dominated by the strongest ones. As the FR variations of the scatterers are caused by the range and chirp bandwidth dependence, no significant spread of the standard deviation is expected. However, the presence of noise in the data increases the standard deviation and also causes a bias away from the ”true” FR towards zero. However, as the SNR of the raw data is nearly constant throughout the data matrix, the FR variations are expected to stay small. The bias results in an underestimation of the FR when based on the raw data. The presence of multiple strong scatterers in a SAR scene reduces this bias, as they improve the SNR. After focusing the image, the standard deviation increases, as the SNR is now very inhomogeneous. While the accuracy decreases, the lowered bias improves the precision, as the SNR is largely higher than in the raw data. To validate the presented FR measurement method not just for a single data set, data from multiple quad-polarized PALSAR scenes from -10 to 50° latitude at diverse ionospheric activity

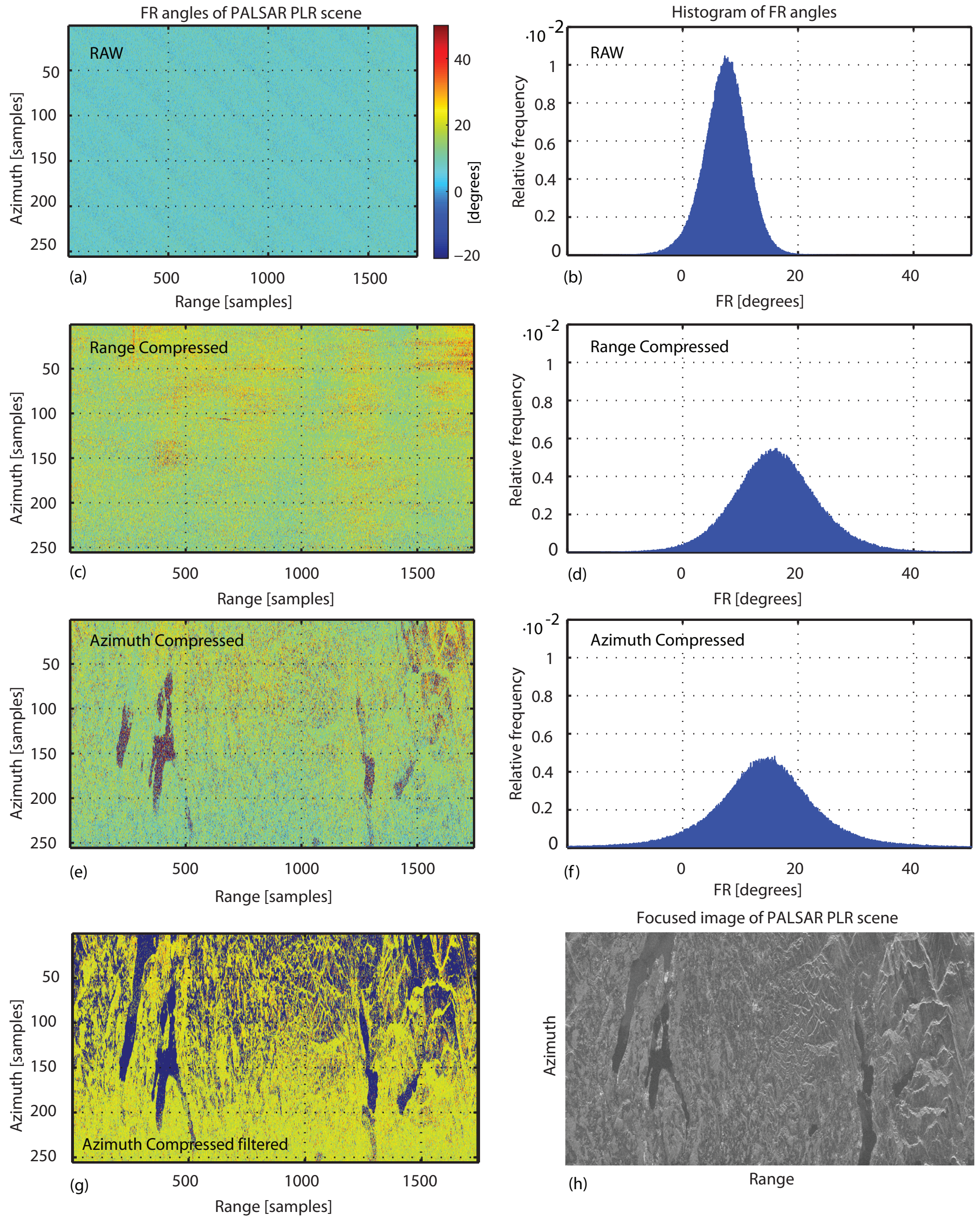

Figure 3.7: (a) FR measurement from the PALSAR raw data, (b) FR histogram, (c) FR from range-compressed data, (d) FR histogram for rc, (e) FR from azimuth-compressed data, (f) FR histogram for ac. In each case, the left image shows FR angles estimated for individual *pixels of a scene, while the right image shows a histogram of the FR values. In (g) scatterers, that are below a 80% limit of peak signal power of the azimuth-compressed data are masked out. (h) shows the corresponding HH amplitude image of the scene as a reference, allowing comparison of the azimuth-compressed FR measurements to the backscatter brightness and hence SNR level.*

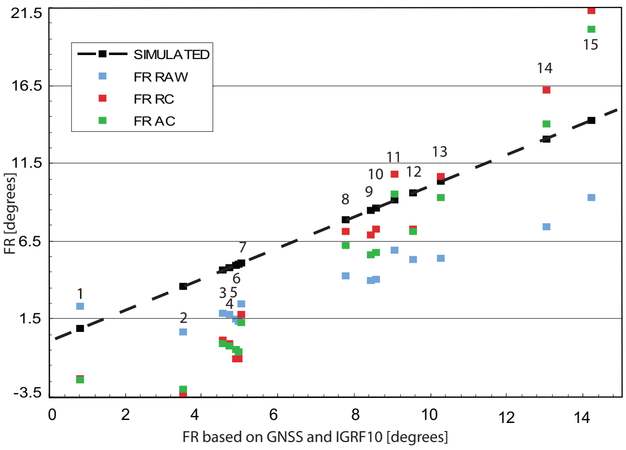

Data No.	Sim. FR	FR RAW	Std.dev. RAW	FR RC	Std.dev. RC	FR AC	Std.dev. AC	TECU slant	TECU from AC
1	0.8°	2.3°	3.5°	-2.4°	9.8°	-2.4°	8.0°	19.8	58.0
2	3.5°	0.7°	3.5°	-3.5°	9.0°	-3.1°	12.6°	5.7	5.0
3	4.6°	1.8°	3.4°	0.1°	8.8°	-0.1°	11.9°	7.4	0.2
4	4.8°	1.8°	3.5°	-0.2°	9.0°	-0.3°	13.2°	7.7	0.5
5	4.9°	1.4°	3.2°	-1.1°	11.2°	-0.5°	20.1°	8.0	0.8
6	5.0°	1.3°	3.3°	-1.1°	10.5°	-0.6°	18.8°	8.1	1.0
7	5.1°	2.4°	3.5°	1.8°	9.1°	1.2°	13.2°	8.1	1.9
8	7.8°	4.3°	3.6°	7.1°	8.7°	6.2°	11.3°	12.4	9.8
9	8.5°	3.9°	3.6°	6.8°	8.4°	5.6°	12.9°	13.6	9.0
10	8.6°	4.0°	3.7°	7.2°	8.9°	5.8°	14.0°	13.8	9.3
11	9.1°	5.9°	2.9°	10.8°	8.4°	9.5°	13.3°	14.6	15.3
12	9.6°	5.3°	4.4°	7.3°	21.8°	7.1°	19.7°	15.7	11.7
13	10.3°	5.3°	3.7°	10.6°	8.5°	9.3°	11.1°	16.3	14.8
14	13.0°	7.4°	3.7°	16.2°	7.7°	14.0°	13.0°	21.0	22.5
15	14.2°	9.3°	4.1°	21.3°	8.9°	20.1°	10.1°	23.8	33.6

Figure 3.8: FR measurements from raw and focused PALSAR scenes from -10 to 50° latitude at diverse ionospheric activity levels. For comparison, GNSS estimates from TEC maps were calculated for each scene (Sim. FR) and plotted as reference data (black line). The table lists the FR estimates and their standard deviation. TEC estimated from the azimuth-compressed data (TECU from AC) is also shown for comparison.

levels were examined. In Fig. 3.8, the results for 15 scenes are presented. The table to the right of Fig. 3.8 shows, in addition to the two-way FR angles, the standard deviation and the estimated/measured TEC levels from the simulation (TECU slant), and the TEC levels (TECU from AC) derived from the mean FR of the azimuth focused data using again the magnetic field over the scene center.

FR estimation for these scenes shows that the FR angles derived from GNSS-based simulations largely agree with the estimations from the real data, generally following the same trend. Very low estimations of FR at comparably high TEC levels (i.e., data set 1) are typically seen near the equator, where the parallel component of the magnetic field is small. The lower half of estimated FR from the real data tends to be *less* than estimations from simulation. This behavior changes for higher FR and compressed data, where the frequency-dependent amplitude variations are generally above the NESZ level. FR from the raw data is usually lower than the estimates from the simulations, but its trend agrees more strongly with GNSS-based simulations. This was also observed in the TCR simulations in Section III-D. The standard deviation, as expected from Section IV-B, increases transitioning from the raw to the focused data. Estimated FR largely decreases from the RC to the AC data.

3.5 Discussion of Results

The simulation results show that raw data clearly are susceptible to the chirp frequency dependence: A good estimate of mean FR was achieved. Derivation of FR from raw data produces an average FR from all contributing frequencies and is dominated by its strongest scatterers. Also caused by the nearly constant SNR, FR variations are expected to stay small. The comparably low SNR in the raw data results in a noise-induced shift of FR angles towards zero, explaining why FR from the raw data tends to be underestimated. Equations (2) and (20) show that FR depends on wavelength. We therefore expect, in addition to a change in the chirp length, a variation in the amplitude of the varying frequency components of a chirp. Under strong ionospheric conditions, these frequency-dependent modifications of the chirp reduce the performance of the matched filter. FR retrievals from raw and RC signals will thus tend to be dominated by the frequency parts of the chirp with higher amplitudes. FR from AC signals shows improved robustness if thresholding is applied. The decision of whether raw, RC or fully compressed images should be used for FR analysis depends on how well compression is able to focus individual targets and also on how high a power threshold value is applied. Higher thresholds yield better estimates and lower FR variations for a single TCR, but they also decrease the number of measurements available in a scene. High TEC levels increase the amplitude variations (within the range of ambiguity) within the chirp and can therefore reduce the reliability of the FR measurement.

The same considerations also apply for real data measurements. For real data, FR measurements of raw data tend to underestimate the true ionospheric TEC and FR effects. Tests where low-power signals were filtered out with a threshold showed the same effects as simulated data: inaccuracies in mean FR values and high FR variance caused by low SNR. Good examples of typical areas with low SNR are quiet water surfaces and mountainous backslopes [Fig. 3.7(e)]. As compression gives all targets an equal opportunity to express their individual FR, an important step toward improving the accuracy of measurements in focused data is therefore the masking out of low SNR regions. A uniform distribution of the FR as in the simulation of the raw data of a single point target cannot be achieved under real conditions.

Observations of trends for FR estimation over many real data scenes show that the FR angles derived from GNSS-based simulations follow the same trend as the estimations from raw and focused data. FR estimates from the raw data generally agree better with simulations, but there are larger differences at higher FR compared to results based on products. FR from the focused data with slant TEC levels below 12 TECU (estimations from TEC maps and the IGRF10 model) are generally around or below retrievals from the raw data.

The Bickel-Bates method [6] proves to be robust and shows that extracting FR from real quad-polarized PALSAR data provides comparable results to GNSS derived FR. We were able to develop a screening tool that enables users of SAR data to scan a large catalog of PALSAR acquisitions for expected FR using only the sensor and acquisition details.

3.6 Conclusions

Frequency-dependent propagation effects are a result of the influence of the ionosphere's electron content along the ray path and the Earth's magnetic field. In order to demonstrate the behavior of radar waves under different ionospheric conditions, a standard SAR simulation was implemented and extended to include ionospheric effects. Point target examples were used to simulate range shifts and frequency-dependent amplitude variations within a SAR image. An evaluation of a set of sensor configurations at P-, L- and X-bands showed that the influence of the ionosphere can become significant at lower frequencies. All polarimetric measurements are affected and must be corrected. Seen in a positive light, it also could enable the extraction of ionospheric FR, and the generation of high-resolution TEC maps.

FR angle estimation using quad-polarized data was applied to simulated and real PALSAR data. It showed that the FR measurement approach discussed in [6] works well for raw, RC, and AC SAR data. In the simulations, the dependency of FR on the instantaneous frequency was seen, and a comparison between the measurements extracted from raw, RC, and AC data was made. The PALSAR data showed first results of FR angles as they appear in any operational polarimetric SAR system. FR retrievals based on GNSS measurements and the IGRF10 model agreed with extracted angles from raw and focused PALSAR data. The use of raw data for FR estimation is recommended, as the results agree better with retrievals from TEC maps and the simulated magnetic field than those based on the focused data. FR estimates from the raw data also generally have lower variability and are not subject to the nonideal focussing algorithms. However, underestimation of FR angles caused by the low SNR must be considered. SAR scenes over low reflecting areas are expected to be more strongly affected.

FR from focused data appears to be shifted due to the frequency-dependent amplitude variations and the change in chirp length that reduce the performance of the matched filter. Calculation of FR using measured TEC maps, a magnetic field model, and the sensor annotations enables users of quad-polarized data to make first estimates of the FR in an acquired scene. No detailed scene-specific analysis of the SAR data is required. To validate the results from a single closely discussed example, data from multiple quad-polarized PALSAR scenes between -10 and 50° latitude at diverse ionospheric activity levels were examined.

Further investigations of the presented approaches, examining more datasets would enable delimitation of the estimation accuracy. It should not be forgotten that the simulations represent ideal situations. The 20 TECU used in the simulations treat the ionosphere at an average activity level. TEC values at these levels can be observed within PALSAR orbits at the programmed acquisition times even during the (presently occurring) solar minimum. The real data could be verified by GNSS. Making use of a polarimetric SAR offers much more than a single FR value: It can provide FR and TEC over a complete scene and at high resolution.

Acknowledgments

We would like to thank P. Pasquali of SARMap S.A. and B. Rosich of ESA-ESRIN for generously providing us with a large number of ALOS PALSAR raw data sets. Furthermore, we are indebted to B. Rommen and B. Rastburg-Arbesser of ESA-ESTEC for their scientific input and financial support. Thanks to the anonymous reviewers for helping improve the quality of the paper.

References

[1] S. H. Bickel and R. H. T. Bates, "Effects of Magneto-Ionic Propagation on the Polarization Scattering Matrix," *Proc. IEEE*, vol. 53, no. 8, pp. 1089–1091, Aug. 1965.

[2] M. Jehle, M. Rüegg, D. Small, E. Meier, and D. Nüesch, "Estimation of Ionospheric TEC and Faraday Rotation for L-band SAR," *Proc. SPIE*, vol. 5979, pp. 252–260, Oct. 2005.

[3] M. Jehle, M. Rüegg, D. Small, and E. Meier, "SAR Data for TEC and Faraday Rotation," Remote Sensing Laboratories, University of Zurich, Final Report 20046/06/NL/CO, May 2007.

[4] F. Meyer, R. Bamler, N. Jakowski, and T. Fritz, "The Potential of Low-Frequency SAR Systems for Mapping Ionospheric TEC Distributions," *IEEE Geosci. Remote Sens. Lett.*, vol. 3, no. 4, pp. 560–564, Oct. 2006.

[5] E. J. M. Rignot, "Effect of Faraday Rotation on L-Band Interferometric and Polarimetric Synthetic-Aperture Radar Data," *IEEE Trans. Geosci. Remote Sens.*, vol. 38, no. 1, pp. 383–390, Dec. 2000.

[6] W. B. Gail, "Effect of Faraday Rotation on Polarimetric SAR," *IEEE Trans. Aerosp. Electron. Syst.*, vol. 34, no. 1, pp. 301–307, Jan. 1998.

[7] P. A. Wright, S. Quegan, N. S. Wheadon, and C. D. Hall, "Faraday Rotation Effects on L-Band Spaceborne Data," *IEEE Trans. Geosci. Remote Sens.*, vol. 41, no. 12, pp. 2735–2744, Dec. 2003.

[8] R.-Y. Qi and Y.-Q. Jin, "Analysis of the Effects of Faraday Rotation on Spaceborne Polarimetric SAR Observations at P-Band," *IEEE Trans. Geosci. Remote Sens.*, vol. 45, no. 5, pp. 1115–1122, May 2007.

[9] J. Liu, Y. Kuga, A. Ishimaru, X. Pi, and A. Freeman, "Ionospheric Effects on SAR Imaging: A Numerical Study," *IEEE Trans. Geosci. Remote Sens.*, vol. 41, no. 5, pp. 939–947, May 2003.

[10] D. M. L. Vine, S. D. Jacob, E. P. Dinnat, P. de Matthaeis, and S. Abraham, "The Influence of Antenna Pattern on Faraday Rotation in Remote Sensing at P-Band," *IEEE Trans. Geosci. Remote Sens.*, vol. 45, no. 9, pp. 2737–2746, Sept. 2007.

[11] A. Freeman and S. S. Saatchi, “On the Detection of Faraday Rotation in Linearly Polarized L-Band SAR Backscatter Signatures,” *IEEE Trans. Geosci. Remote Sens.*, vol. 42, no. 8, pp. 1607–1616, Aug. 2006.

[12] A. Freeman, “Calibration of Linearly Polarized Polarimatric SAR Data Subject to Faraday Rotation,” *IEEE Trans. Geosci. Remote Sens.*, vol. 42, no. 8, pp. 1617–1624, Aug. 2004.

[13] W. B. Gail, “A Simplified Calibration Technique for Polarimetric Radars,” in *Proc. IGARSS*, vol. 2, Tokyo, Japan, Aug. 1993, pp. 377–379.

[14] R. Touzi and M. Shimada, “On the Use of Symmetric Scatterers for Calibration and Validation of PALSAR Polarimetric Modes,” in *Proc. IGARSS*, vol. 3, Anchorage, AK, Sept. 2004, pp. 1835–1837.

[15] D. H. Hoekman and M. J. Quiriones, “Land Cover Type and Biomass Classification Using AirSAR Data for Evaluation of Monitoring Scenarios in the Colombian Amazon,” *IEEE Trans. Geosci. Remote Sens.*, vol. 38, no. 2, pp. 685–696, Mar. 2000.

[16] B. Hallberg, G. Smith, A. Olofsson, and L. M. H. Ulander, “Performance Simulation of Spaceborne P-Band SAR for Global Biomass Retrieval,” in *Proc. IGARSS*, vol. 1, Anchorage, AK, Sept. 2004, pp. 503–506.

[17] J. Nicoll, F. Meyer, and M. Jehle, “Prediction and Detection of Faraday Rotation in ALOS PALSAR Data,” in *Proc. IGARSS*, Barcelona, Spain, Aug. 2007, p. 2350.

[18] Z.-W. Xu, J. Wu, and Z.-S. Wu, “A Survey of Ionospheric Effects on Space-Based Radar,” *Waves Random Media*, vol. 14, no. 12, pp. 189–272, Apr. 2004.

[19] S. Macmillan and S. Maus, “International Geomagnetic Reference Field—The Tenth Generation,” *Earth Planets Space*, vol. 57, no. 12, Dec. 2005.

[20] R. A. Langel, *The Main Field.* Academic Press, 1987, vol. 1.

[21] S. Chapman and J. Bartels, *Geomagnetism.* Oxford University Press, 1940.

[22] U. Hugentobler, M. Meindl, G. Beutler, H. Bock, R. Dach, A. Jäggi, C. Urschl, L. Mervart, M. Rothacher, S. Schaer, E. Brockmann, D. Ineichen, A. Wiget, U. Wild, G. Weber, H. Habrich, and C. Boucher, “CODE IGS Analysis Center Technical Report 2003/2004,” Astronomical Institute, University of Bern,” Annual Technical Report, 2004. [Online]. Available: http://www.aiub.unibe.ch/content/research/gnss/publications/

[23] R. F. Hanssen, *Radar Interferometry.* Kluwer Academic Publishers, 2001, vol. 2.

[24] K. Davies and E. K. Smith, “Ionospheric Effects on Satellite Land Mobile Systems,” *IEEE Antennas Propag. Mag.*, vol. 44, no. 6, pp. 24–31, Dec. 2002.

[25] M. Soumekh, *Synthetic Aperture Radar Signal Processing with MATLAB Algorithms.* New York: John Wiley & Sons, Inc., 1999.

[26] I. G. Cumming and F. H. Wong, *Digital Processing of Synthetic Aperture Radar Data, Algorithms and Implementation.* Boston: Artech House, 2005.

[27] M. Shimada, A. Rosenqvist, M. Watanabe, and T. Tadono, "The Polarimetric and Interferometric Potential of ALOS PALSAR," in *Proc. POLinSAR 2005*, Frascati, Italy, Jan. 2005.

[28] "Information on ALOS PALSAR Products for ADEN Users," European Space Agency, Technical Note ALOS-GSEG-EOPG-TN-07-0001, Apr. 2007.

[29] M. Sekido, T. Kondo, E. Kawai, and M. Imae, "Evaluation of GPS-based ionospheric TEC map by comparing with VLBI data," *Radio Sci.*, vol. 38, no. 4, July 2003.

Chapter 4

Measurement of Ionospheric TEC in Spaceborne SAR Data

This chapter has been submitted as:
M. Jehle, O. Frey, D. Small and E. Meier.
Measurement of Ionospheric TEC in Spaceborne SAR Data
Transactions on Geoscience and Remote Sensing, Pages 1-8, submitted 28. May 2009

Abstract

Propagation of spaceborne radar signals operating at L-band frequency or below can be seriously affected by the ionosphere. At high states of solar activity, Faraday rotation (FR) and signal path delays disturb radar polarimetry and reduce resolution in range and azimuth. While these effects are negligible at X-band, FR and the frequency-dependent path delays can become seriously problematic starting at L-band. For quality assurance and calibration purposes, existing L-band or potential spaceborne P-band missions require estimation of the ionospheric state before or during the data take. The work at hand introduces two approaches for measuring the ionospheric total electron content (TEC) from single-pol spaceborne SAR data. The two methods are demonstrated using simulations. Both methods leverage knowledge of the frequency-dependent path delay through the ionosphere: the first estimates TEC from the phase error of the filter mismatch, while the second gauges path delay differences between up- and down chirps. FR, mean (DC) offsets and noise contributions are also considered in the simulations. Finally, possibilities for further methodological improvements are discussed.

4.1 Introduction

A major problem in assessing the global carbon cycle is the state of understanding of the terrestrial ecosystem. Measuring the biomass on a global scale including its temporal variations would help to improve knowledge of these processes. Good estimates of forest biomass could be obtained from synthetic aperture radar (SAR) at lower frequencies such as P-band [1]. However, the performance of a spaceborne SAR system at lower frequencies is often significantly degraded by the effects of the ionosphere. In order to correct or avoid these problems, it is necessary to assess the ionospheric state before or during a data take.

Under strong solar activity, the influence of the ionosphere on radar signal propagation at L- and P-band becomes a significant error source. Low frequencies and high chirp signal bandwidth are more susceptible to effects like signal path delay and Faraday rotation (FR). Frequency-dependent path delays and FR result in changes to the chirp length, and imply a variation of the chirp amplitude for single-pol sensor configurations. While these effects are not noticeable at X-band frequencies and above, the performance of sensors starting at L-band and lower is reduced [2].

Since the launch of the Advanced Land Observing Satellite (ALOS) and the on-board Phased Array L-band Synthetic Aperture Radar (PALSAR) instrument, spaceborne SAR data at L-band has been available to study the ionospheric effects from polarimetric measurements. Depending on the acquisition mode, the PALSAR range chirp bandwidth can be as high as 28 MHz. A preliminary study investigated the influence of the ionosphere at low frequencies (L-band and lower). Signal degradation caused by the ionosphere also increases with larger chirp bandwidths [3, 4].

In this work, the aim is to describe algorithms and possibilities for the estimation of the ionospheric total electron content (TEC) from low carrier frequency high bandwidth SAR raw data. The chirp replica is iteratively modeled until it best matches a synthetic pulse deformed under the influence of the ionosphere. In a second approach introduced later, the phase information from alternating up- and down chirps is utilised. Changes causing phase advance, chirp length modification, amplitude and chirp-rate modulations are considered to evaluate local TEC levels.

The potential of low-frequency SAR with ionospheric path delays and FR for TEC measurements was recognized in [2, 5]. FR effects were discussed at length in [6–8]. Corrective methods were treated in [9], distortion effects in [10]. Detection and estimation techniques based on quad-polarized data are presented in [6,11–13]. A good estimation improves general polarimetric calibration and validation techniques such as those described in [14] and [15], helping to improve reliability of spaceborne polarimetric measurements for biomass classification and retrieval [16,17]. In [18,19], a first analysis of PALSAR data considering FR detection was presented. An alternative concept for spaceborne SAR at low frequencies was shown in [20].

In Section 4.2, the theoretical background of the ionospheric influences on electromagnetic waves is outlined. The algorithms used for simulation of spaceborne SAR backscatter from a trihedral corner reflector (TCR) are introduced (including FR). The influence of the frequency-dependent path delay within a radar up- or down chirp is explained and integrated in the simulation. Simulations are then carried out for typical L- and P-band sensor configurations with multiple targets in a scene.

To estimate TEC levels from SAR raw data, two methods are described in Section 4.3 and Section 4.4. The suitability of SAR data to TEC estimation under real conditions is assessed using comparable noise levels, FR and disturbing targets within a scene. The results of simulated L- and P-band data are compared, and possible methods for proper validation are suggested. In conclusion, the results are summarized in Section 4.5, and directions for further research are discussed.

4.2 Effects of the Ionosphere

Electromagnetic waves propagating through the ionosphere experience a polarisation rotation of the electric field vector and a signal path delay that depends on the free electron density number N_e along the ray path, the signal frequency f and the strength of the magnetic field parallel to the propagation direction of the wave within the ionized layer. The reversal of paths in two-way propagation from a satellite to the Earth and back does *not* compensate for this effect. Instead, the effect is cumulative: Faraday rotation *doubles* as does the path delay [3].

4.2.1 Ionosphere

In a manner similar to chromatic abberation in a camera lens, wavelength-dependent distortions can be introduced to radar measurements by the ionosphere. Spaceborne SAR systems usually transmit linear frequency modulated chirp pulses. Mathematically, a chirped pulse s_0 is a function of time t and can be written as

$$s_0(t) = U_{st} \cdot e^{j2\pi(f_{\text{start}} \cdot t \pm \alpha \cdot t^2)} \qquad 0 \leq t \leq T_p, \tag{4.1}$$

where the amplitude U_{st}, the start frequency of the chirp $f_{\text{start}} = f_c \pm f_0$, the chirp rate $\alpha = \frac{f_0}{T_p}$ and the pulse duration T_p parameterise the chirps. f_c is the center frequency and $f_0 = \frac{B}{2}$ is half of the chirp bandwidth B. The ± distinguishes between up- and down-chirps. As the refractive index of the ionosphere is dependent on frequency, each sample of a chirp is delayed individually. The *group* refractive index of the ionosphere can be estimated from

$$n \approx 1 + \frac{f_N^2}{2f^2} \tag{4.2}$$

$$f_N^2 = \frac{N_e e^2}{4\pi^2 \varepsilon_0 m_e} = 80.56 N_e, \tag{4.3}$$

where f_N is the plasma frequency, e is the charge of an electron, m_e is the electron mass and ε_0 is the electric permittivity. The delay by the ionosphere compared to vacuum conditions is given by

$$\Delta t = \frac{1}{c}\int_{path} n - 1 ds = \frac{40.28}{cf^2}\int_{path} N_e ds = \frac{40.28}{cf^2}\text{TEC}. \tag{4.4}$$

Based on the individual path delays at either end of the chirps, a modified chirp rate and pulse duration can be estimated to simulate the chirp after propagation through the ionosphere. Matched filtering of the chirp was done by convolution of the measured signal s_r with the complex conjugate of the transmitted chirp s_t^*. For the range compressed signal s_{rg} one has

$$\begin{aligned} s_{rg} &= s_t^*(t) * s_r(t) \\ &= \mathcal{F}^{-1}\{S_t(w)^* \cdot S_r(w)\} \end{aligned} \tag{4.5}$$

where $S_t(w), S_r(w)$ are the Fourier transforms of s_t and s_r respectively and $\mathcal{F}^{-1}$ denotes the inverse Fourier transform.

4.2.2 Faraday Rotation

At L-band frequencies or lower, FR has serious effects on SAR imagery. Backscatter measurements from single-pol sensor configurations can become ambiguous at high solar activity conditions. Within the following simulations, FR is expected to play a minor role as there is only a small change in polarisation rotation *within* a chirp. Nevertheless, FR rotation was considered in the simulations. The one-way FR Ω may be estimated from [9] and [7] as:

$$\begin{aligned} \Omega &= \frac{2.365 \cdot 10^4}{c^2} \cdot \lambda^2 \cdot B_{||} \int_0^h N_e \ dh \\ &\approx \frac{2.365 \cdot 10^4}{f^2} \cdot \text{VTEC} \cdot \frac{1}{\cos\gamma} \cdot B_{||}, \end{aligned} \tag{4.6}$$

where $B_{||}$ is the mean parallel magnetic field within the ionized layer, λ the wavelength of the radar wave, VTEC the vertical total electron content (TEC in nadir direction) and γ the off-nadir angle of the observation. The factor $1/\cos\gamma$ is used to transform the vertical electron content to the electron content along the propagation path h. The commonly used zenith angle of the radar wave at the sub-ionospheric point was therefore approximated by the satellite's off-nadir angle [21]. VTEC may be estimated using global ionospheric maps (GIM) from the Center for Orbit Determination in Europe (CODE) [22]. γ may be obtained for each image location in a product from the sensor data annotations for most current SAR satellites. The parallel magnetic field was estimated using the International Geomagnetic Reference Field model (IGRF10) [23]. More details on the modelling of FR can be found in [13].

4.2.3 Chirp Signal Path Delay

Within the ionospheric layer, the refractive index that the wave group sees increases at higher solar activity to above unity. As information within a radar pulse travels with the group velocity, the arrival of the pulse back at the antenna is delayed according to [24] and Eq.(4) by

$$\Delta t_{\text{iono}} = 2 \cdot \frac{K}{c} \cdot \frac{\text{TEC}}{f^2}, \tag{4.7}$$

where c is the speed of light, TEC is the total electron content along the signal path and $K = 40.28\frac{\text{m}^3}{\text{s}^2}$ is a refractive constant. For two-way propagation from a satellite to Earth and back, the pulse front is delayed between

$$t_{\text{shift\_min\_d}} = 2 \cdot \frac{K}{c} \cdot \frac{\text{TEC}}{(f_c + f_0)^2} \tag{4.8}$$

and

$$t_{\text{shift\_min\_u}} = 2 \cdot \frac{K}{c} \cdot \frac{\text{TEC}}{(f_c - f_0)^2}, \tag{4.9}$$

where the indexes d and u indicate that the starting frequency of the up - or down chirp is used respectively. The new pulse duration of the chirp after traversing the ionosphere twice can be calculated as

$$T_{p\_\text{iono}} = T_p \mp \frac{2}{c} \cdot K \cdot \text{TEC} \cdot \left(\frac{1}{(f_c - f_0)^2} - \frac{1}{(f_c + f_0)^2} \right). \tag{4.10}$$

The time delay of the pulse and the accompanying linear chirp rate alterations imply also phase distortions. Given that the frequency components are invariant under non neutral (vacuum) ionospheric conditions, there must be a phase advance approximately equal to the path delay. The refractive index for the phase is reduced to less than unity. The extent of the phase advance can therefore be estimated using the time delay Δt_{iono} together with the angular frequency $\omega = 2\pi f$:

$$\Delta\phi = -\omega \cdot \Delta t_{\text{iono}} = -\frac{4\pi \cdot 40.28}{cf} \cdot \text{TEC}. \tag{4.11}$$

For a linearly frequency modulated chirp, these frequency-dependent shifts imply a slight change in the chirp rate and thus a change in the length of the transmitted pulse. Figure 4.1 shows a sketch of the expected chirp path and length variations caused by the ionosphere. The pulses at the top sketch the shape of down- and up chirps under neutral ionospheric conditions. The green arrows mark where the pulses center after range compression. The pulses at the bottom are simulated for an ionised state of the ionosphere. The red dashed line shows the shape of the transmitted pulse aligned to the left with the received pulse to outline the chirp length and chirp rate variations before and after passing through the ionosphere. The green arrows again show where the pulses center after matched filtering when using a reference chirp similar to the transmitted chirp. Matching the received signals with the unaltered transmitted pulses causes a slight filter mismatch and therefore a marginally shorter arrow length. The red arrows show where the pulses would center if the ionosphere were absent with a constant path delay applied shifting the dashed red pulse before the deformed pulses. The most crucial parameter in the matched filtering process is the chirp rate. A varying chirp rate causes a filter mismatch if left uncorrected, broadening the main lobe and raising the sidelobes. A parameter that is a measure for the broadening of the pulse is the quadratic phase error (QPE). The QPE at the margins of a chirp with pulse duration T_p can be estimated for a signal at baseband from the phase difference of the signals at the time $\frac{T_p}{2}$ using [25]

$$\begin{aligned}
\text{QPE} &= \phi\left(s_t(\frac{T_p}{2})\right) - \phi\left(s_r(\frac{T_p}{2})\right) \\
&= 2\pi\Delta\alpha \cdot \left(\frac{T_p}{2}\right)^2 \\
&= 2\pi f_0 \left(\frac{1}{T_p} - \frac{1}{T_{p\_\text{iono}}}\right) \cdot \left(\frac{T_p}{2}\right)^2 \\
&= \frac{4\pi K f_0 T_p}{c T_{p\_\text{iono}}} \frac{f_c f_0}{(f_c - f_0)^2 (f_c + f_0)^2} \cdot \text{TEC} \\
&\approx \frac{4\pi K f_0^2}{c f_c^3} \cdot \text{TEC}, \qquad (4.12)
\end{aligned}$$

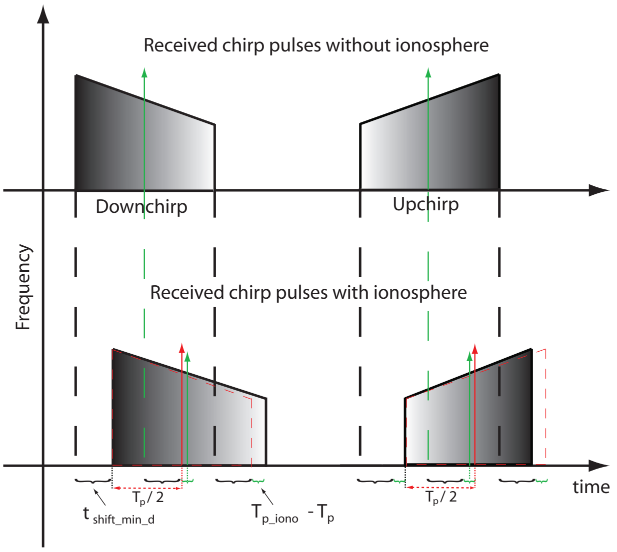

Figure 4.1: Received chirp pulses without (top) and including ionospheric effects (bottom). The green arrows show where the pulses center after range compression. Red dashed line: Shape of transmitted chirp aligned to received pulse. Red arrow: Peak after range compression matched to the transmitted pulse.

where the indices t and r mark the transmitted or received pulse, and $\Delta\alpha$ is the change in the chirp rate. The phase error at the peak of the range compressed target is found to be $\mathrm{QPE}_{\mathrm{peak}} \approx \frac{\mathrm{QPE}}{3}$ [25]. The unequal length of the matched pulses shifts the range compressed peak by half of the chirp length difference, causing an additional phase shift equal in magnitude to the QPE when compared to an ideal matched filtering result. CPE denotes the third order phase error as it can be estimated using the Taylor series expansion of the ionospheric transfer function [26]. As their contribution is in the range of a hundredth of a degree, it can safely be neglected in the simulations.

4.3 Simulations

Simulation of ionospheric effects in SAR data enables the testing of new methodologies to estimate the ionospheric state during a SAR acquisition. Ionospheric states can be modeled and tested under consistent geometric conditions and without any temporal decorrelation. When simulating the influence of TEC on SAR signals, the bandwidth-dependent ionospheric behavior described above must be considered. In the following simulations, the modifications caused by the ionosphere are incorporated by replacing the reference chirp rate and the time delay vector with values corresponding to a modeled ionospheric state, enabling simulation of frequency-dependent FR. The signal return of TCRs under typical noise levels and including direct current (DC) offsets is analysed. Possibilities for estimating the traversed TEC from analysis of the modified chirp or the phase difference of an alternating pair of chirps are evaluated. The PALSAR instrument (L-band) and a possible P-band configuration for a spaceborne sensor parameterise the simulations. The configuration parameters are listed in Table 4.1 together with corresponding typical effects on the pulse at different ionospheric states. Significantly higher TEC values are expected in the equatorial region at solar max.

4.3.1 TEC Autofocus

Estimation of TEC from SAR data by evaluating pulse degradation requires high contrast, typically strong point targets such as corner reflectors within an otherwise dark area, to achieve a high signal-to-clutter ratio (SCR).

One models ionospheric states differing from neutral ionospheric conditions (vacuum) to a ionised state where both pulses match optimally. The algorithm iteratively tries to compensate the phase error caused by a change in the chirp rate of the pulse while propagating through the ionosphere, and is comparable to existing SAR azimuth autofocusing techniques such as the phase gradient or the range Doppler algorithm [25], [27].

A chirp replica is built using the static system parameters such as chirp bandwidth, chirp form (up- or down-chirp), pulse repetition frequency (PRF), sampling rate and center frequency. As the TEC level is successively increased, the chirp rate of the reference pulse is modified. Range compression is then done repeatedly with a set of generated

Sensor	**L-band**			**P-band**		
	PALSAR FBS			ESA Biomass		
Frequency (f_c) [GHz]	1.27			0.435		
Bandwidth (B) [MHz]	28			6		
Chirp duration [μsec]	27			27		
Sampling rate [MHz]	32			8		
Chirp form	down			down		
Orbit (altitude) [km]	695			695		
TEC [TECU]	**5**	**15**	**25**	**5**	**15**	**25**
Path delay (2-way) at f_c [m]	2.50	7.49	12.48	21.3	63.9	106.4
Change in chirp length (2-way) over B [m]	0.11	0.33	0.55	0.59	1.76	2.93
Faraday rotation at f_c (2-way) [°]	2.95	8.86	14.8	25.2	75.5	125.9
QPE and CPE	0.46	1.39	2.31	0.53	1.58	2.64
at $\frac{T_p}{2}$ (2-way) [°]	0.01	0.02	0.03	0.00	0.01	0.02
Phase error at RC peak (2-way) [°]	0.62	1.85	3.09	0.71	2.11	3.52

Table 4.1: SAR system configuration details and expected ionospheric effects at nadir based on simualtions.

TEC-dependent reference chirps. As a measure for the quality of the range compression, the peak to side-lobe ratio (PSLR) was used. Though the bandwidth of the chirp in general is static, the pulse sampled at reception might have a slightly reduced bandwidth depending on the time interval between two samples ($\frac{1}{f_s}$, f_s = sampling rate) and the sampling window start time. The implemented correction algorithm therefore correlates the generated replica with a simulated received pulse not only for a wide range of different TEC levels but also for multiple path delays within $\frac{1}{f_s}$. A nearly identical path delay of the vector ensures a coherent phase and bandwidth distribution in both signals.

Figure 4.2a) shows the result of the TEC autofocus algorithm for a simulated TCR at 15 TECU and a SCR of 3 dB (raw data). The black dots mark for every timestep the location of maximum correlation. The overall maximum is marked with a white dot. Variations depending on the different TEC levels and the multiple start-time positions are also visible. Figure 4.2b) plots the phase measured at the black dots in 4.2a). The extent of the variations depends on the carrier frequency and sampling rate and was found to be $\approx 0.7°$ for this L-band case. While Figure 4.2a) and b) show the results of an ensemble of

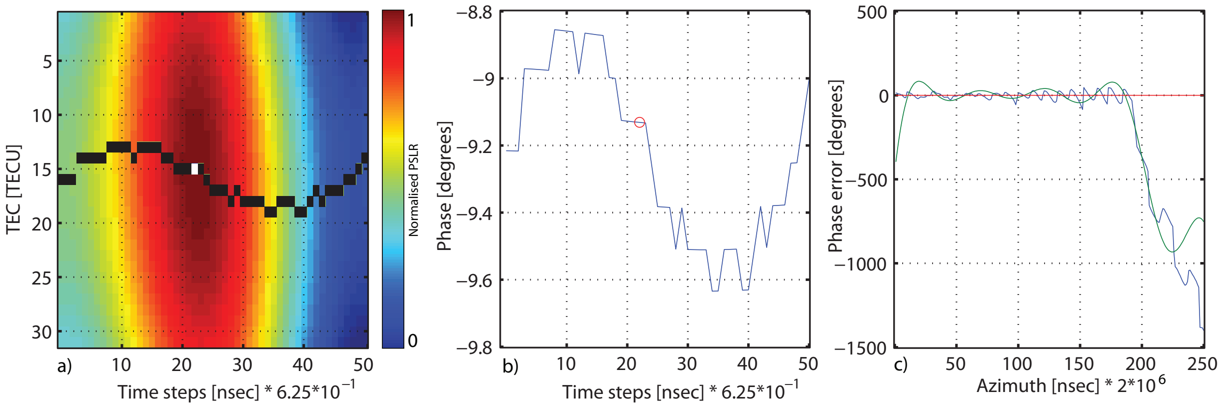

Figure 4.2: a) L-band results of TEC autofocus algorithm with detected PSLR maximum at each time step marked in black- and the overall detected maximum marked as a white dot. The maximum PSLR was measured from simulations based on sets of TEC and modeled path delay used to fit the reference chirp in the matched filter. b) Phase at maximum in correlation and c) Phase error of range compressed target along azimuth. Red line: ideal case (no noise, no disturbing scatterers), blue line: measured phase error, green line: phase error of FFT-filtered range compressed phase distribution. The abscissa units in range- and azimuth direction are set to integer sample intervals.

100 range lines, Figure 4.2c) shows an example of the phase error, measured for each range line, between the range compressed phase of a TCR including noise and multiple targets (blue line) and the ideal phase distribution without noise and other scatterers present (red line). The green line is the phase error that remains after a moving average and FFT filtering are applied. The influence of a strong scatterer is visible at azimuth lines 200 to 250. A set of 10 disturbing point scatterers were simulated and randomly distributed in an area of 500 to 1500 m (in range, azimuth around the point target) with amplitudes between 25 to 75 percent of the point target.

The correlation peaks when both chirps best match each other at the desired TEC level at the time

$$\begin{aligned} t_{\mathrm{peak}} &= \frac{T_{p\_\mathrm{iono}}}{2} + t_{\mathrm{shift\_min\_u/d}} + \frac{2R_{\mathrm{sat}}}{c} \\ &= \frac{T_p}{2} + \frac{K}{c} \cdot \mathrm{TEC}\left(\frac{1}{(f_c - f_0)^2} - \frac{1}{(f_c + f_0)^2}\right) + \\ &\quad + t_{\mathrm{shift\_min\_u/d}} + \frac{2R_{\mathrm{sat}}}{c}. \end{aligned} \tag{4.13}$$

where R_{sat} denotes the range distance from the satellite to the target and $\frac{2R_{\mathrm{sat}}}{c}$ therefore describes the round-trip delay. Eq. 4.13 shows that the location of the target peak is independent of the chirp form. Estimation accuracy of t_{peak} depends on the length of the sampled time steps. Extraction of the peak in the range compressed data is done using complex FFT oversampling (factor of 50) to obtain sub-sample accuracy. To increase the

SCR, a set of 100 range lines around the TCR are focused. The range-dependent phase and the local frequency offset due to the target Doppler are removed. As the target location is sensitive to chirp rate alterations, the range of closest approach for the TCR is calculated individually for every iteration step.

The phase distribution of the TCR over azimuth is interpolated with fast Fourier transform (FFT) zero padding. The range distance at closest approach is used as a reference value during range migration compensation (RMC). The range compressed phase distribution of the simulated TCR data over azimuth was smoothed using a moving average filter and a fourier interpolation to improve RMC. The removal of range-dependent phase relative to the closest approach (RMC) of the range line is performed by a linear phase multiplication in the frequency domain as

$$p_{\text{shifted}}(t) = \text{FFT}\{p_f(t)\} \cdot e^{j4\pi(\frac{f_r \Delta R}{c})}, \tag{4.14}$$

where ΔR is the range distance between closest approach and the peak of the range compressed TCR at the a azimuth position. $p_f(t)$ is the signal after removing the Doppler frequency, and f_r is the range frequency.

4.3.2 TCR Simulation Results

The feasibility of the presented technique depends mainly on the SCR within the surveyed TCR area. Simulations were carried out over a range of three noise levels under variable ionospheric conditions, including randomly distributed disturbing scatterers in the area of the examined TCR. All simulations include FR contributions appropriate to the corresponding TEC levels and a DC offset with a magnitude of the noise amplitude. The magnetic field model necessary for FR estimation was calculated using the IGRF10 model described in section 4.2.2. Magnetic field values typical at mid-latitudes over the northern hemisphere were used. Each configuration was simulated 50 times to enable approximation of the expected mean and standard deviation of the retrieved TEC levels. To increase the SCR, a limited number of 100 range lines around the range of closest approach of the TCR were focused also in azimuth.

Table 4.2 shows the L-band simulation results at 1.25, 2.5 and 3 dB SCR within the raw data. The TEC levels vary between 5, 15 and 25 TECU. As expected, the variability of the TEC estimates is reduced given higher SCR or increased TEC levels. Similar behavior albeit with larger variations was observed in P-band simulations, mainly due to the comparably low number of chirp samples - summary results are shown in Table 4.3. For the P-band simulations, the oversampling rate and the number of time steps within an interval $dt = \frac{1}{f_s}$ were increased to enable more direct comparison with the L-band simulation settings.

It becomes clear that both systems should generally be suitable for TEC estimation using strong targets. For both systems, the variability is reduced at higher TEC levels. The example simulating 5 TECU is an exception, due to the 0 TEC iteration boundary.

L-band						
SCR	**1.25 dB**		**2.5 dB**		**3 dB**	
TEC simulated	∅TEC	σ_Ω	∅TEC	σ_Ω	∅TEC	σ_Ω
5 [TECU]	8.2	7.3	9.4	4.2	4.3	3.0
15 [TECU]	16.1	7.9	16.3	6.6	15.8	6.1
25 [TECU]	22.1	7.1	22.9	6.0	23.1	4.9

Table 4.2: TEC estimation using simulated L-band SAR data containing one TCR. ∅TEC denotes the mean extracted TEC in [TECU] over 50 independent simulations. σ_Ω is the corresponding standard deviation of the TEC estimates.

P-band						
SCR	**1.25 dB**		**2.5 dB**		**3 dB**	
TEC simulated	∅TEC	σ_Ω	∅TEC	σ_Ω	∅TEC	σ_Ω
5 [TECU]	8.4	6.5	8.3	7.5	4.4	5.9
15 [TECU]	11.3	14.2	13.4	13	10.1	13.3
25 [TECU]	24.0	12.1	23.9	8.9	21.1	9.4

Table 4.3: TEC estimation using simulated P-band SAR data containing one TCR. ∅TEC denotes the mean extracted TEC in [TECU] over 50 independent simulations. σ_Ω is the corresponding standard deviation of the TEC estimates.

Smaller deviations were achieved when the method was applied to a larger number of selected strong scatterers within a scene. The feasibility of the autofocus technique for TEC estimation depends on the reliability requirements of the desired TEC data and improves with an increased number of chirp samples at the same carrier frequency. As seen in Table 4.2, simulations show that estimation of TEC seems feasible with a standard deviation of ≈ 6 TECU for PALSAR-type sensor configurations.

4.4 Potential of TEC Estimation from Up- and Down Chirp Calibration Bursts

In this section, the aim is to improve the limited accuracy expected from the previous method by adding a more direct retrieval method at the system level. In the former simulations, the initial chirp rate provided in the system specifications was iteratively adapted to derive a received pulse where both chirps match optimally. In the following, a burst of alternating up- and down chirps is used to help separate the TEC from their resulting phase differences. This technique estimates TEC from alternating up- and down chirps using the whole bandwidth. In contrast to earlier simulations, this method measures

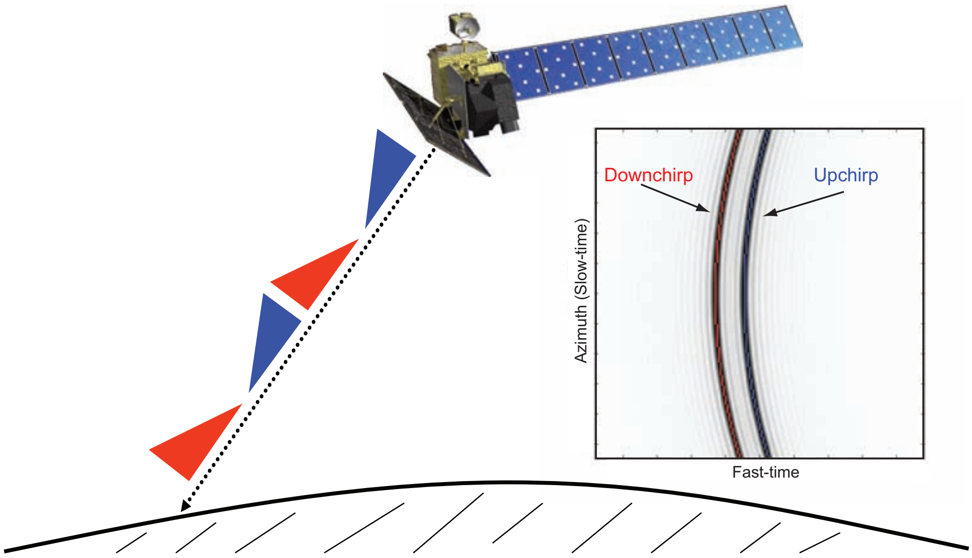

Figure 4.3: Sketch of alternating chirp technique. Satellite transmits alternating up- and down chirps. On the right: Ideally range compressed chirp pulses dependent on the start frequency *of the chirp for a TCR under active ionospheric conditions.*

the differences in path delay that both chirps undergo within the same ionospheric state, making use of the ionosphere's dispersive behavior and resulting in a phase difference of the compressed target. Figure 4.3 shows a sketch of an alternate chirp approach, where a satellite interleaves up- and down chirps. Assuming ideal range compression, the path delays of the wave front, *dependent on the start frequencies* of the chirp, are visualized on the right. The resulting differences in path delay depend mainly on the chirp carrier frequency and the chirp bandwidth. Comparable observations might be achieved from split bandwidth arrangements without switching between up- and down chirps.

The up- and down chirp's starting-frequencies naturally differ by the chirp bandwidth. As shown in Eq. 4.11 and Table 4.1, a phase advance changes the measured chirp rate of the received pulse. This can cause a filter mismatch that is approximately equal in magnitude for both up/down-chirps. While the decreased chirp rate of the down chirp causes an increased chirp length, the pulse length of the up chirp is reduced. Compared to the peak correlation location under vacuum conditions, the up chirp is shifted to precede this position (see Fig. 4.1).

The TEC can then be estimated using the difference between both range compressed phase distributions, i.e. $\Delta\phi_{\mathrm{up\_down}}$ [rad] by applying the time delay difference evaluated between the starting frequency and the group delay of the envelope (Eq. 4.10 (second part), Eq. 4.11)

$$\mathrm{TEC} = \frac{\Delta\phi_{\mathrm{up\_down}} \cdot c}{4\pi f_c \cdot K} \cdot \frac{(f_c - f_0)^2 \cdot (f_c + f_0)^2}{(f_c + f_0)^2 - (f_c - f_0)^2}. \tag{4.15}$$

Fig. 4.4a) shows an example of the amplitude and the phase in Fig. 4.4b) of a simulated

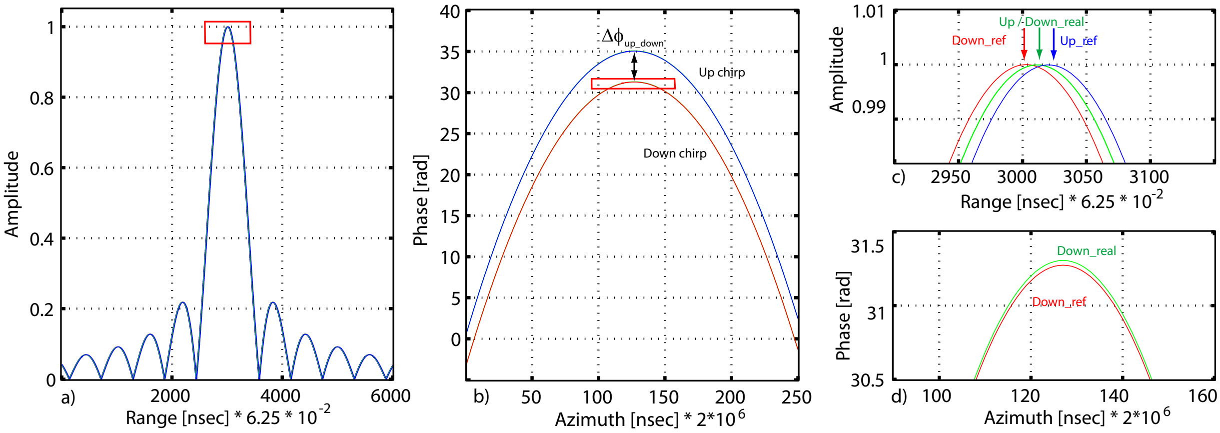

Figure 4.4: a) L-band range compressed up- and down chirps after passing through an ionosphere modelled at a state of 15 TECU along the signal path (of a TCR). The red line simulates a down chirp, the blue line an up chirp. The blue and red lines were simulated considering only a constant ionospheric path delay based on the starting frequency of the chirp (ref = rigid shift without frequency dependency). The green line also considers the frequency-dependent path delays within the chirp (real). a) Range compressed pulses, b) phase distribution of the chirp pulses c) and d) are close-ups of the plot areas indicated in a) and b). The abscissa units in range- and azimuth direction are set to integer sample intervals.

TCR at L-band after range compression. Fig. 4.4c) and Fig. 4.4d) show magnified versions of Fig. 4.4a) and Fig. 4.4b).

The green line corresponds to the simulations including the path delay differences within the chirp. To better visualize and compare the phase error caused by the filter mismatch, the blue and red lines in Fig. 4.4a) to d) show the simulation results produced when one includes only the path delay corresponding to the *start frequency* of the chirp, neglecting path delay differences *within the chirp*. In Fig. 4.4d), one sees that the down chirp is compressed to a point slightly before the up chirp. Adding the change in pulse duration shifts the down chirp half of the change in pulse length towards the up chirp, and vice versa. Both pulses overlap at the position of the expected group delay (green line). As the pulses are already in baseband, this shift has only a small effect on the phase of the chirps (seen from Fig. 4.4d)). Table 4.4 shows the estimated phase differences between the mean up- and down chirp phase of a focused TCR. The results were additionally calculated for a typical X-band sensor configuration (TerraSAR-X, B=300 MHz). As expected, sensitivity is higher in the P-band configuration. But due to the higher chirp bandwidth, sensitivity at X-band remains high enough to theoretically be able to extract the ionospheric state at 1 TECU levels. Technical realisation would require further investigation.

System:	**P-band**	**L-band**	**X-band**
f_c [GHz]	0.435	1.27	9.65
B [MHz]	6	28	300
$K_{\mathrm{NORM}} \cdot \frac{B}{f_c^2}$	1.83	1	0.19
TEC [TECU]	$\Delta\phi_{\mathrm{up\_down}}$	$\Delta\phi_{\mathrm{up\_down}}$	$\Delta\phi_{\mathrm{up\_down}}$
1	61.3°	33.6°	6.2°
5	306.7°	168.0°	31.2°
15	920.3°	503.9°	93.5°

Table 4.4: Sensitivity of P, L, and X-band sensor's using the up- and down chirp technique at 1, 5, and 15 TECU. K_{NORM} *estimated at L-band for 1 TECU was used for normalisation.*

4.5 Discussion and Conclusions

With ESA's candidate Earth explorer BIOMASS carrying a P-band SAR as its payload, the need to estimate the ionospheric state before an acquisition is imperative. One suitable method could be by sending a burst of quad-pol pulses that enable measurement of FR along the signal path. This paper shows two alternative methods that make use of the frequency-dependent path delay that a chirp undergoes while passing through the ionosphere. These techniques estimate the local TEC along the signal path and can be single-pol measurements. Estimation of FR from TEC measurements additionally requires knowledge of the magnetic field.

The first method shown uses an autofocus technique that optimises the reference chirp to be used for range compression, maximising the PSLR where the ionospheric effects on the recovered chirp's shape are best modeled. Estimation of TEC using this method requires strong contrast within the scene - limiting applicability in areas such as forest. Simulations show that extraction of TEC from one strong TCR appears feasible when the SCR (of the raw data) is above 2.5 dB. Feasibility of the autofocus technique for estimating TEC depends mainly on the resolution requirements of the desired TEC data and the number of chirp samples. Simulations of L-band sensor configurations showed that estimation of TEC seems feasible with a standard deviation of 6 TECU. Additional simulations at higher TEC levels showed improved accuracy, but still can not compare with TEC results from the dense GPS networks over North America or Europe. One advantage of the method is that the measurements from the radar data estimate the TEC directly along the observation path with directly relevant spatial and temporal resolution. Improvements to SCR could be made by combining the information from a set of strong scatterers within a scene. As this method would be much more time consuming and less suitable for operational use, the systematic alternate up/down pulse methodology would be favored where possible.

Phase differences in the L-band simulations were as high as 30°/TECU. TEC estimation at 1 TECU levels then becomes possible without requiring specific reference targets. Delimitation of the achievable accuracies is currently being investigated. No hardware-changes on the satellite-module should be necessary [28]. A second matched filter as well as pulse generation could be added / modified through software revisions.

Consideration of this technique should include as an option recording the whole scene using the alternating chirp method. As the shapes of the pulses are different, future applications might consider increasing the PRF, as pulses could overlap more closely [26]. For calibration, one could also use a quad-pol calibration burst. Measurement of TEC and Faraday rotation in a calibration burst additionally enables estimation of the geomagnetic field. As scintillations mainly come from electron density irregularities in the E- and F-region and one can reasonably assume a linearly varying geomagnetic field within the space of an acquisition, the FR data from a quad-pol acquisition could be transferred straightforwardly into a corresponding high resolution TEC map.

In addition to DC offset, disturbing targets and varying noise levels, the simulations enable modelling of the frequency-dependent FR. As FR changes the orientation angle of the radar wave, a single polarised antenna would see a very small frequency-dependent amplitude modulation of the chirp signal, not expected to significantly reduce the sensitivity of the TEC estimation techniques. The simulated DC offset was removed by subtracting the mean without noticeably corrupting the results. A first test and validation of the alternating chirp technique could be realized by building a transponder that switches between up and down chirp replicas. Sensitivity tests using simulations show that also TerraSAR-X acquisitions would be suitable for analysis.

Acknowledgments

We would like to thank B. Rommen and B. Rastburg-Arbesser of ESA-ESTEC for their scientific input and financial support during the initial stages of the software development.

References

[1] E. J. M. Rignot, R. Zimmermann, and J. J. van Zyl, “Spaceborne applications of P band imaging radars for measuring forest biomass,” *IEEE Trans. Geosci. Remote Sens.*, vol. 33, no. 5, pp. 1162–1169, Sept. 1995.

[2] M. Jehle, M. Rüegg, D. Small, E. Meier, and D. Nüesch, “Estimation of Ionospheric TEC and Faraday Rotation for L-band SAR,” *Proc. SPIE*, vol. 5979, pp. 252–260, Oct. 2005.

[3] Z.-W. Xu, J. Wu, and Z.-S. Wu, “A Survey of Ionospheric Effects on Space-Based Radar,” *Waves Random Media*, vol. 14, no. 12, pp. 189–272, Apr. 2004.

[4] Z.-W. Xu, J. Wu, and Z.-S. Wu, “Potential Effects of the Ionosphere on Space-Based SAR Imaging,” *IEEE Trans. on Antennas and Propagation*, vol. 56, no. 7, pp. 1968–1975, July 2008.

[5] F. Meyer, R. Bamler, N. Jakowski, and T. Fritz, “The Potential of Low-Frequency SAR Systems for Mapping Ionospheric TEC Distributions,” *IEEE Geosci. Remote Sens. Lett.*, vol. 3, no. 4, pp. 560–564, Oct. 2006.

[6] S. H. Bickel and R. H. T. Bates, “Effects of Magneto-Ionic Propagation on the Polarization Scattering Matrix,” *in Proc. IEEE*, vol. 53, no. 8, pp. 1089–1091, Aug. 1965.

[7] E. J. M. Rignot, “Effect of Faraday Rotation on L-Band Interferometric and Polarimetric Synthetic-Aperture Radar Data,” *IEEE Trans. Geosci. Remote Sens.*, vol. 38, no. 1, pp. 383–390, Jan. 2000.

[8] W. B. Gail, “Effect of Faraday Rotation on Polarimetric SAR,” *IEEE Trans. Aerosp. Electron. Syst.*, vol. 34, no. 1, pp. 301–307, Jan. 1998.

[9] P. A. Wright, S. Quegan, N. S. Wheadon, and C. D. Hall, “Faraday Rotation Effects on L-Band Spaceborne Data,” *IEEE Trans. Geosci. Remote Sens.*, vol. 41, no. 12, pp. 2735–2744, Dec. 2003.

[10] R.-Y. Qi and Y.-Q. Jin, “Analysis of the Effects of Faraday Rotation on Spaceborne Polarimetric SAR Observations at P-Band,” *IEEE Trans. Geosci. Remote Sens.*, vol. 45, no. 5, pp. 1115–1122, May 2007.

[11] A. Freeman and S. S. Saatchi, “On the Detection of Faraday Rotation in Linearly Polarized L-Band SAR Backscatter Signatures,” *IEEE Trans. Geosci. Remote Sens.*, vol. 42, no. 8, pp. 1607–1616, Aug. 2006.

[12] A. Freeman, “Calibration of Linearly Polarized Polarimatric SAR Data Subject to Faraday Rotation,” *IEEE Trans. Geosci. Remote Sens.*, vol. 42, no. 8, pp. 1617–1624, Aug. 2004.

[13] M. Jehle, M. Rüegg, L. Zuberbühler, D. Small, and E. Meier, “Measurement of Ionospheric Faraday Rotation in Simulated and Real Spaceborne SAR Data,” *IEEE Trans. Geosci. Remote Sens.*, vol. 47, no. 5, pp. 1512–1523, May 2009.

[14] W. B. Gail, “A Simplified Calibration Technique for Polarimetric Radars,” in *Proc. IGARSS*, vol. 2, Tokyo, Japan, Aug. 1993, pp. 377–379.

[15] R. Touzi and M. Shimada, “On the Use of Symmetric Scatterers for Calibration and Validation of PALSAR Polarimetric Modes,” in *Proc. IGARSS*, vol. 3, Anchorage, AK, USA, Sept. 2004, pp. 1835–1837.

[16] D. H. Hoekman and M. J. Quiriones, “Land Cover Type and Biomass Classification Using AirSAR Data for Evaluation of Monitoring Scenarios in the Colombian Amazon,” *IEEE Trans. Geosci. Remote Sens.*, vol. 38, no. 2, pp. 685–696, Mar. 2000.

[17] B. Hallberg, G. Smith, A. Olofsson, and L. M. H. Ulander, “Performance Simulation of Spaceborne P-Band SAR for Global Biomass Retrieval,” in *Proc. IGARSS*, vol. 1, Anchorage, AK, USA, Sept. 2004, pp. 503–506.

[18] J. Nicoll, F. Meyer, and M. Jehle, “Prediction and Detection of Faraday Rotation in ALOS PALSAR Data,” in *Proc. IGARSS*, Barcelona, Spain, 2007, pp. 5210–5213.

[19] F. J. Meyer and J. B. Nicoll, “Prediction, Detection, and Correction of Faraday Rotation in Full-Polarimetric L-Band SAR Data,” *IEEE Trans. Geosci. Remote Sens.*, vol. 46, no. 10, pp. 3076–3086, Oct. 2008.

[20] P. C. Dubois-Fernandez, J.-C. Souyris, S. Angelliaume, and F. Garestier, “The Compact Polarimetry Alternative for Spaceborne SAR at Low Frequency,” *IEEE Trans. Geosci. Remote Sens.*, vol. 46, no. 10, pp. 3208–3222, Oct. 2008.

[21] S. Schaer, “Mapping and Predicting the Earth’s Ionosphere Using the Global Positioning System,” *Geodätisch-geophysikalische Arbeiten in der Schweiz*, vol. 59, 1999.

[22] U. Hugentobler, M. Meindl, G. Beutler, H. Bock, R. Dach, A. Jäggi, C. Urschl, L. Mervart, M. Rothacher, S. Schaer, E. Brockmann, D. Ineichen, A. Wiget, U. Wild, G. Weber, H. Habrich, and C. Boucher, “CODE IGS Analysis Center Technical Report 2003/2004,” Astronomical Institute, University of Bern,” Annual Technical Report, 2004, last accessed Apr., 2009. [Online]. Available: http://www.aiub.unibe.ch/content/research/gnss/publications/

[23] S. Macmillan and S. Maus, "International Geomagnetic Reference Field—The Tenth Generation," *Earth Planets Space*, vol. 57, no. 12, Dec. 2005.

[24] R. F. Hanssen, *Radar Interferometry.* Kluwer Academic Publishers, 2001, vol. 2.

[25] I. G. Cumming and F. H. Wong, *Digital Processing of Synthetic Aperture Radar Data, Algorithms and Implementation.* Boston: Artech House, 2005.

[26] G. H. Millman and C. D. Bell, "Ionospheric Dispersion of an FM Electromagnetic Pulse," *IEEE Trans. on Antennas and Propagation*, pp. 152–155, Jan. 1971.

[27] P. H. Eichel, D. C. Ghiglia, and C. V. Jakowatz, "Speckle processing method for synthetic-aperture-radar phase correction," *Opt. Lett.*, vol. 14, no. 1, pp. 1–3, 1989.

[28] U. Stein and M. Younis, "Suppression of range ambiguities in synthetic aperture radar systems." *Proc. EUROCON*, vol. 2, pp. 417–421, Sept. 2003.

Chapter 5

Conclusions

In the following, the results are briefly summarized and possible directions for future research in the area of atmospheric investigations with SAR are discussed. The bibliographical references within this chapter point to the bibliographical references in Chapter 1.

5.1 Summary of Results

5.1.1 Tropospheric Path Delay

The correction of atmospheric path delays in high-resolution spaceborne SAR systems has become increasingly important with continuing improvements to the resolution of SAR systems surveying the Earth. Atmospheric path delays must be taken into account in order to achieve geolocation accuracies better than 1 meter. Models correcting tropospheric path delays within operational SAR processing typically estimate the contributions based on an average amount. In regions with mountainous topography, where altitude differences within a scene of over 3000 meters can be found, path delays resulting from the troposphere can differ by up to nearly 1 meter.

In combination with the launch of TerraSAR-X and RSL's calibration and validation activities, a field campaign in the Jungfraujoch region was organised. One aim was to measure the tropospheric path delay differences and to validate the results with on-site DGPS corner reflector measurements.

Within a set of seven TSX stripmap data takes, four corner reflectors (CR) were positioned at two different altitudes but nearly identical ranges.

The difference between high and low altitude CRs was approximately 3000 meters. Analysis and comparison of the SAR data and the DGPS measurements showed that the resulting geolocation accuracy stayed within the requirements but also verified the results of a newly developed tropospheric path delay model. As the model was based on average atmospheric conditions and did not include any weather data, errors were still expected at the cm level. The model might be useful for operational and pixel-based corrections of the tropospheric path delay contributions. Even changes in water vapour concentration between the various data takes could be observed. The nearly constant path delay differences between the reflectors at both altitudes demonstrated the high sensitivity of TerraSAR-X.

5.1.2 TEC and Faraday Rotation from SAR data

Ionospheric propagation effects become significant to radars starting at L-band carrier frequencies (and lower). Signal distortions in terms of FR, frequency-dependent range delay, and interferometric phase bias can have serious implications on quality of SAR imagery. Currently used methods correcting these effects use the frequency-dependent path delay for TEC estimation along the signal path (e.g. GNSS receivers using the L1 and L2 components) or propose the extraction of the FR from quad-pol SAR data.

With the recently launched ALOS satellite operating at L-band, extraction of ionospheric FR from spaceborne SAR data became possible for the first time. Simulation and estimation of FR can be done using measured TEC maps, a magnetic field model and the sensor annotations. This enables users of quad-polarized data to make quick estimates of the FR for an acquired scene. No detailed scene-specific analysis of the SAR data is required.

Simulations as well as measurements from real data showed that azimuth compression is not required: even raw and range compressed data can be used for FR estimation from quad-pol data.

The PALSAR data showed first results of FR angles as they appear in any operational polarimetric SAR system. FR retrievals based on GNSS measurements and the IGRF10 model agreed with extracted angles from raw and focused PALSAR data. To validate the results from a single, closely discussed example, data from multiple quad-polarized PALSAR scenes between -10 and 50° latitude at diverse ionospheric activity levels were examined. Making use of a polarimetric SAR offers much more than a single FR value: it can provide FR and TEC over a complete scene and at high resolution.

With a view to the growing demand for the estimation of the ionospheric state before or during a SAR data take, two alternative methods were presented that make use of the frequency-dependent path delay that a chirp undergoes when passing through the ionosphere. These techniques estimate the TEC along the signal path and require only single-pol measurements.

The first method shown uses an "TEC autofocus" technique that models the reference chirp used for range compression to minimise its PSLR where the ionospheric effects on the chirp's shape are best modelled. The simulations showed that extraction of TEC from one strong TCR seems feasible when the signal-to-clutter ratio is above 2.5 dB.

The second method provides a possible concept for future sensor configurations that is more sensitive to TEC than TEC autofocus described method. It uses information provided by alternating up- and down chirps within a calibration burst. The TEC is estimated from the phase difference of the two compressed pulse forms that are delayed individually according to their differing starting frequencies. Thus, extraction of TEC would be possible without requiring any reference data. No hardware changes on the satellite-module should be necessary [28]. A second matched filter as well as pulse generation could be added or modified through software revisions.

5.2 Outlook

Estimation and monitoring water vapour from SAR measurements continues to be an interesting topic for further research. In comparison with results from ray-tracer models, the SAR measurements deliver an additional source of measurement data and can provide high resolution maps of integrated water vapour. Inclusion of ray-bending effects using models or measurements and a comparison with the path delay and the corresponding weather data may lead to improved geolocation accuracies. A problem is the low repetition rate of spaceborne SAR sensors, currently making this data source less attractive to meteorologists. Further investigations of the presented approaches, and examination of more datasets would enable delimitation of the estimation accuracy.

Possible future directions for ionospheric research might include generation of a 3D ionospheric model from a tomographic TEC analysis using GNSS network measurements. With possible contributions also come SAR measurements. Another interesting topic could be searching for precursory evidence of an upcoming earthquake. Recent research results indicate that the ionosphere can show anomalies five days prior to an earthquake [17]. Possible techniques to survey and measure such anomalies globally were presented in Chapter 4. However these techniques are based on simulations and need to be refined and verified with measurements. Under well defined conditions outlined in Chapter 4, the sensors ALOS PALSAR and also TerraSAR-X might be suitable for such validation measurements. A transponder switching between up- and down chirps could be used for a validation of the presented techniques. While in this case, one would aim to make use of information from ionospheric effects on signal degradation, further research might establish ways to prevent data from being irrepairably corrupted by the ionosphere. Prerotation of the polarization angle in order to compensate the FR effects or sending a burst of pulses prior to a single-pol SAR acquisition are promising ideas. A spaceborne P-band SAR system could provide a valuable contribution to improving knowledge of the understanding of the terrestrial ecosystem and the global carbon cycle: research activities should further improve models for the correction of ionospheric effects, especially FR, without requiring narrow-swath quad-pol data.

Appendix A

Appendix

In this Appendix, more detailed derivations and explanations of the mathematical basis for the conversions used in Chapter 1 are summarized. The bibliographical references in this chapter also refer to the list at the end of Chapter 1.

A.1 Maxwell's Equations

The complete Maxwell equations within a continuous medium are [5], [21]

$$\begin{aligned} \bigtriangledown \times \vec{H} &= \frac{\partial \vec{D}}{\partial t} + \vec{J} && \text{(A.1)} \\ \bigtriangledown \times \vec{E} &= -\frac{\partial \vec{B}}{\partial t} && \text{(A.2)} \\ \bigtriangledown \cdot \vec{B} &= 0 && \text{(A.3)} \\ \bigtriangledown \cdot \vec{D} &= \rho_{\mathrm{el}}, && \text{(A.4)} \end{aligned}$$

where $\bigtriangledown = (\frac{\partial}{\partial x}, \frac{\partial}{\partial y}, \frac{\partial}{\partial z})$ describes the nabla operator. The expressions e.g. $\bigtriangledown \times \vec{E} = \mathrm{rot}\vec{E}$ and $\bigtriangledown \cdot \vec{B} = \mathrm{div}\vec{B}$ describe the rotation of the electric field vector $\vec{E}$ and the divergence of the magnetic flux density vector $\vec{B}$. $\vec{H}$ describes the magnetic field, $\vec{D}$ the electric displacement, $\vec{J}$ the electric current density and ρ_{el} the free charge density. The field vector variables generally depend on time t and location $s(x, y, z)$. For a homogeneous and isotropic field, the electric displacement, and the propagation speed can be written as

$$\begin{aligned} \vec{D} &= \varepsilon \vec{E} = \varepsilon_0 \varepsilon_r \vec{E} && \text{(A.5)} \\ \vec{B} &= \mu \vec{H} = \mu_0 \mu_r \vec{H} && \text{(A.6)} \\ c &= \frac{1}{\sqrt{\mu\varepsilon}} = \frac{c_0}{\sqrt{\mu_r \varepsilon_r}}, && \text{(A.7)} \end{aligned}$$

where ε_r is the relative permittivity, μ_0 the magnetic constant, and μ_r the relative permeability.

A.2 Derivation of Appleton-Hartree Equation

The equation of motion of an electron within the ionosphere can be written as

$$\begin{aligned} m_e \frac{d\vec{v}}{dt} &= e_{el}\vec{E} + e_{el}\vec{v} \times \vec{B} - m_e \nu \vec{v} \qquad \text{(A.8)} \\ m_e & \quad \text{is the electron mass [kg]} \\ e_{el} & \quad \text{is the charge of an electron [C]} \\ \vec{v} & \quad \text{is the speed of an electron [m/s]} \\ \nu & \quad \text{is the collision frequency [Hz],} \end{aligned}$$

where the first term on the right side describes the Coulomb force, the second is due to the Lorentz force and the last denotes the frictional force caused by the collision of electrons and heavy particles [21]. The velocity can be written as $\vec{v} = \frac{d\vec{s}}{dt}$. The time dependencies in Eq. A.8 are assumed to be only within the electric- and magnetic field. Therefore, any harmonic propagation $X(t)$ depending on time through the factor $e^{j\omega t}$ can be written as

$$X(t) = X \cdot e^{j\omega t} \Rightarrow \quad \frac{dX}{dt} = j\omega \cdot X \cdot e^{j\omega t} \Rightarrow \quad \frac{d}{dt} = j\omega, \quad \frac{d^2}{dt^2} = -\omega^2. \qquad \text{(A.9)}$$

Insertion in Eq. A.8 and writing depending on $\vec{E}$ gives

$$\vec{E} = -\Big(\frac{\omega^2 m_e}{e_{el}} - j\frac{\omega m_e \nu}{e_{el}}\Big)\vec{s} - j\omega\vec{s} \times \vec{B}. \qquad \text{(A.10)}$$

With the definition of the medium polarization $\vec{P}$ within a volume

$$\vec{P} = N_e e_{el} \vec{s}, \qquad \text{(A.11)}$$

where N_e is the electron number density, Eq. A.10 converted to E and multiplied by the electric permittivity ε_0 $[\frac{As}{Vm}]$ can then be written in component form as

$$\begin{aligned} \varepsilon_0 E_x &= -\frac{\omega^2}{\omega_N^2}\Big(1 - j\frac{\nu}{\omega}\Big)P_x + j\gamma_L P_y - j\gamma_T P_z \\ \varepsilon_0 E_y &= -j\gamma_L P_x - \frac{\omega^2}{\omega_N^2}\Big(1 - j\frac{\nu}{\omega}\Big)P_y \\ \varepsilon_0 E_z &= j\gamma_T P_x - \frac{\omega^2}{\omega_N^2}\Big(1 - j\frac{\nu}{\omega}\Big)P_z, \qquad \text{(A.12)} \end{aligned}$$

where

$$\begin{aligned} \omega_N^2 &= \frac{N_e e_{el}^2}{m_e \varepsilon_0} \qquad \text{(A.13)} \\ \omega_{L,T} &= -\frac{B_{L,T} e_{el}}{m_e} \qquad \text{(A.14)} \\ \gamma_{L,T} &= -\omega \cdot \frac{\omega_{L,T}}{\omega_N^2}. \qquad \text{(A.15)} \end{aligned}$$

ω_N is the angular plasma frequency, $\omega_{L,T}$ are the longitudinal and the transverse components of the angular gyrofrequency of the magnetic field. More details on the gyrofrequency of the magnetic field and in plasmas can be found in [22]. From Maxwell's equations the components for a wave propagating in z-direction are derived assuming no variations in the medium in x- and y- directions. Their derivations can therefore be set to zero. From Eq. A.1, Eq. A.2 and Eq. A.9 the electric field components can be derived as

$$\begin{aligned} \frac{dE_x}{dz} &= -j\omega B_y && \text{(A.16)} \\ \frac{dE_y}{dz} &= j\omega B_x && \text{(A.17)} \\ 0 &= B_z && \text{(A.18)} \\ \frac{dH_x}{dz} &= J_y + j\omega\varepsilon_0 E_y && \text{(A.19)} \\ -\frac{dH_y}{dz} &= J_x + j\omega\varepsilon_0 E_x && \text{(A.20)} \\ 0 &= J_z + j\omega\varepsilon_0 E_z. && \text{(A.21)} \end{aligned}$$

Differentiating Eq. A.16 and Eq. A.17 once more after z and using Eq. A.19, Eq. A.20 together with

$$\vec{B} = \mu_0 \vec{H}, \quad \vec{J} = N_e e \vec{v}, \quad \vec{v} = \frac{d\vec{s}}{dt} \Rightarrow \vec{J} = j\omega\vec{P} \tag{A.22}$$

results in

$$\begin{aligned} \frac{d^2E_x}{dz^2} + \frac{\omega^2}{c_0^2}E_x &= -\omega^2\mu_0 P_x && \text{(A.23)} \\ \frac{d^2E_y}{dz^2} + \frac{\omega^2}{c_0^2}E_y &= -\omega^2\mu_0 P_y && \text{(A.24)} \\ \varepsilon_0 E_z &= -P_z. && \text{(A.25)} \end{aligned}$$

Assuming a constant amplitude E_0 in a homogeneous, isotropic medium and a time-dependency after

$$E = E_0 e^{j(\omega t - kz)}, \tag{A.26}$$

where $k = \frac{\omega}{v_{\text{phase}}} = \frac{\omega}{c_0} n_{\text{phase}}$ is the wave number and v_{phase} is the phase velocity (see Chapter 1.3.2). For free space ($n = 1$) propagation $v_{\text{phase}} = c_0$. With $c_0^2 = \frac{1}{\varepsilon_0\mu_0}$ derived under the above mentioned conditions, Eq. A.23 to Eq. A.25 can be written as

$$\begin{aligned} (1-n^2)E_x &= -\frac{P_x}{\varepsilon_0} && \text{(A.27)} \\ (1-n^2)E_y &= -\frac{P_y}{\varepsilon_0} && \text{(A.28)} \\ E_z &= -\frac{P_z}{\varepsilon_0}. && \text{(A.29)} \end{aligned}$$

Combining the results from Maxwell's equations in Eq.Eq. A.29 with the results from the equation of motion in Eq. A.12 reduces to

$$\begin{aligned}
\varepsilon_0 E_x &= -\left\{\frac{\omega^2}{\omega_N^2}\Big(1-j\frac{\nu}{\omega}\Big)+\frac{\gamma_T^2}{1-\frac{\omega^2}{\omega_N^2}\Big[1-j\frac{\nu}{\omega}\Big]}\right\}P_x + j\gamma_L P_y && \text{(A.30)}\\
\varepsilon_0 E_y &= -j\gamma_L P_x - \frac{\omega^2}{\omega_N^2}\Big(1-j\frac{\nu}{\omega}\Big)P_y. && \text{(A.31)}
\end{aligned}$$

Using the components P_x and P_y from Eq. A.27 and Eq. A.28, Eq. A.31 can be written as

$$\begin{aligned}
-j\gamma_L(1-n^2)\varepsilon_0 E_y &= \\
&\varepsilon_0 E_x\Big(1-(1-n^2)\cdot\Big\{\frac{\omega^2}{\omega_N^2}\Big(1-j\frac{\nu}{\omega}\Big)+\frac{\gamma_T^2}{1-\frac{\omega^2}{\omega_N^2}\Big[1-j\frac{\nu}{\omega}\Big]}\Big\}\Big)\\
j\gamma_L(1-n^2)\varepsilon_0 E_x &= \varepsilon_0 E_y\Big\{1-\frac{\omega^2}{\omega_N^2}(1-n^2)(1-j\frac{\nu}{\omega})\Big\}. && \text{(A.32)}
\end{aligned}$$

The ratio of these two equations solved for n^2 is called the Appleton-Hartree dispersion equation:

$$\begin{aligned}
n^2 &= (\mu-j\chi)^2 && \text{(A.33)}\\
&= 1-\frac{1}{\frac{2\omega^2}{\omega_N^2}\big(1-j\frac{\nu}{\omega}\big)+\frac{\gamma_T^2}{1-\frac{\omega^2}{\omega_N^2}[1-j\frac{\nu}{\omega}]}\pm\Big[\frac{\gamma_T^4}{\{1-\frac{\omega^2}{\omega_N^2}[1-j\frac{\nu}{\omega}]\}^2}+4\gamma_L^2\Big]^{1/2}}. && \text{(A.34)}
\end{aligned}$$

A.3 Derivation of the Polarisation Rotation

The electric field component of a linearly polarized wave in y direction can be written using Eq. A.26 as

$$\begin{aligned}
E_x &= 0\\
E_y &= \mathrm{Re}\{E_0\cdot e^{j(wt-kz)}\} = E_0\cos(wt-kz)\\
E_z &= 0\\
k &= \frac{\omega}{v_{\text{phase}}} = \frac{w}{c_0}\cdot n_{\text{phase}}. && \text{(A.35)}
\end{aligned}$$

Eq. A.35 can be expressed as the sum of two separate circularly rotating waves $\vec{E} = \vec{E}^+ + \vec{E}^-$:

$$\begin{aligned}
E_x^+ &= \frac{1}{2}E_0\sin(wt-k^+z) \quad E_x^- = -\frac{1}{2}E_0\sin(wt-k^-z)\\
E_y^+ &= \frac{1}{2}E_0\cos(wt-k^+z) \quad E_y^- = \frac{1}{2}E_0\cos(wt-k^-z)\\
E_z^+ &= 0 \qquad\qquad\qquad\qquad E_z^- = 0, && \text{(A.36)}
\end{aligned}$$

where k^+ and k^- are the wave numbers resulting from the refractivity conditions in Eq. 1.18 each wave experiences. The components can be approximated using the refractive index for $\omega \gg \omega_N \quad (\Rightarrow X \ll 1)$ by

$$\begin{aligned}
k^+ &= \frac{w}{c_0} \cdot \left(\sqrt{1 - \frac{X}{1 - Y_L}} \right) \approx \frac{w}{c_0} \cdot (1 - 0.5(1 + Y_L)X) \\
k^- &= \frac{w}{c_0} \cdot \left(\sqrt{1 - \frac{X}{1 + Y_L}} \right) \approx \frac{w}{c_0} \cdot (1 - 0.5(1 - Y_L)X) \\
k^+ &= \frac{w}{c_0} \cdot (1 - 0.5X - 0.5XY_L) = k_\circ - \Delta k \\
k^- &= \frac{w}{c_0} \cdot (1 - 0.5X + 0.5XY_L) = k_\circ + \Delta k, \qquad \text{(A.37)}
\end{aligned}$$

where $k_\circ$ is the wave number resulting without the presence of a magnetic field, and Δk describes the difference induced when a longitudinal magnetic field component is present. Inserting $k_\circ \pm \Delta k$ in Eq. A.36, Eq. A.36 can be trigonometrically converted and added back together:

$$\begin{aligned}
E_x &= E_0 \cos(wt - k_\circ z) \cos(wt - \Delta kz) \\
E_y &= E_0 \cos(wt - k_\circ z) \sin(wt - \Delta kz) \\
E_z &= 0. \qquad \text{(A.38)}
\end{aligned}$$

The polarization angle of the wave φ can then be estimated by

$$\varphi = \tan^{-1} \left(\frac{E_y}{E_x} \right) = \Delta kz. \qquad \text{(A.39)}$$

A.4 Modelling of Tropospheric Parameters

To adjust the parameters for the receiver's height on the Earth's surface, the following models can be used [19]:

$$\begin{array}{lcll}
\mathrm{T} & = & T' - \beta' \cdot h, & [\mathrm{K}] \\
P_s & = & P' \left(\frac{T}{T'} \right)^{\frac{g}{\beta' R_d}}, & [\mathrm{mbar}] \\
\mathrm{e} & = & e' \left(\frac{T}{T'} \right)^{\frac{(\lambda'+1)g}{\beta' R_d}}, & [\mathrm{mbar}] \\
g_m & = & 9.784(1 - 0.0026 \cos 2\phi - 28 \cdot 10^{-8} h), & [\mathrm{m/s^2}] \\
g & = & 9.81 \quad \text{average acceleration due to Earth gravity} & [\mathrm{m/s^2}] \\
h & = & \text{receiver altitude}, & [\mathrm{m}] \\
\phi & = & \text{receiver latitude} & [\text{degrees}],
\end{array}$$

where the apostrophe ' indicates that the seasonal variation of the parameter according to Eq. 1.31 is applied. T is the modelled temperature, P_s the surface air pressure, e the water vapour pressure, and g_m the local acceleration due to gravity.

A.5 Look-up Table for Model of Above Sea Level Parameters on Earth Ellipsoid

Mean ($\boldsymbol{\xi_{\mathrm{mean}}}$):					
Latitude	P_{mean} [hPa]	T_{mean} [K]	e_{mean} [hPa]	β_{mean} [K/m]	λ_{mean}
0	1010.3	300.5	28.3	$6.16 \cdot 10^{-3}$	2.77
15	1013.25	299.65	26.31	$6.30 \cdot 10^{-3}$	2.77
30	1017.25	294.15	21.79	$6.05 \cdot 10^{-3}$	3.15
45	1015.75	283.15	11.66	$5.58 \cdot 10^{-3}$	2.57
60	1011.75	272.15	6.78	$5.39 \cdot 10^{-3}$	1.81
75	1013.00	263.65	4.11	$4.53 \cdot 10^{-3}$	1.55
90	1015.00	259.8	2.6	$3.88 \cdot 10^{-3}$	1.55
Amplitude ($\boldsymbol{\xi_{\mathrm{amp}}}$):					
Latitude	P_{amp} [hPa]	T_{amp} [K]	e_{amp} [hPa]	β_{amp} [K/m]	λ_{amp}
0	0.00	0.00	0.00	$0.00 \cdot 10^{-3}$	0.00
15	0.00	0.00	0.00	$0.00 \cdot 10^{-3}$	0.00
30	-3.75	7.00	8.85	$0.25 \cdot 10^{-3}$	0.33
45	-2.25	11.00	7.24	$0.32 \cdot 10^{-3}$	0.46
60	-1.75	15.00	5.36	$0.81 \cdot 10^{-3}$	0.74
75	-0.50	14.50	3.39	$0.62 \cdot 10^{-3}$	0.30
90	-0.50	14.50	3.39	$0.62 \cdot 10^{-3}$	0.30

Table A.1: Look-up Table for Above Sea Level Parameters

For latitudes ϕ in steps of 15° the look-up table provides the mean air pressure P_{mean}, mean temperature T_{mean}, mean water vapour pressure e_{mean}, mean temperature lapse rate β_{mean}, and the mean decrease of water vapour λ_{mean}. Each parameter ξ_{mean} is adjusted using a cosine function with an amplitude ξ_{amp} specified in the look-up table to model seasonal variations after Eq. 1.31.

List of Figures

List of Tables

List of Acronyms

AC Azimuth Compressed

AGP Antenna Gain Pattern

ALOS Advanced Land Observing Satellite

ASAR Advanced Synthetic Aperture Radar

AVG Average Reference Height

CODE Center for Orbit Determination in Europe

CR Corner Reflector

dB decibel

DC Direct Current

DGPS Differential GPS

DLR German Aerospace Center

DOY Day Of Year

EIA Equatorial Ionisation Anomaly

ENVISAT Environmental Satellite

ESA European Space Agency

ESTEC European Space Research and Technology Center

FFT Fast Fourier Transform

FR Faraday rotation

GHz Gigahertz

GIM Global Ionospheric Maps

GNSS Global Navigation Satellite System

GPS Global Positioning System

HM Height-dependent Model

IAGA International Association of Geomagnetism and Aeronomy

IGRF International Geomagnetic Reference Field model

INT Interlaken

IONEX IONosphere map EXchange

JAXA Japan Aerospace Exploration Agency

JJ Jungfraujoch

km kilometer

MI Meiringen/Interlaken

MEI Meiringen

MERIS Medium Resolution Imaging Spectrometer

MHz Megahertz

NESZ Noise Equivalent Sigma Zero

NMF Neill Mapping Function

NWP Numerical Weather Prediction

PALSAR Phased Array L-band Synthetic Aperture Radar

PRF Pulse Repetition Frequency

PSLR Peak to Side-lobe Ratio

QPE Quadratic Phase Error

RC Range Compressed

RMC Range Migration Compensation

RT Raytracer

SAR Synthetic Aperture Radar

SCR Signal-to-Clutter Ratio

SLC Single Look Complex

SNR Signal to Noise Ratio

TCR Trihedral Corner Reflector

TEC Total Electron Content

TECU TEC units

TID Traveling Ionospheric Disturbance

TSX TerraSAR-X

UV Ultra Violet

VTEC Vertical Total Electron Content

List of Symbols

A		Amplitude of the received pulse.
B	[1/s]	Chirp bandwidth.
L_a	[dB]	Track attenuation.
M_0		Measured scattering matrix.
M_{hh1}, M_{hh2}		The amplitudes of the chirp at its start respective stop frequencies.
N		Scaled-up refractivity.
N_e	[1/m^3]	Electron number density.
$N_{\mathrm{tropo}}, N_{\mathrm{hyd}}$		Scaled-up refractivity for the troposphere and the hydrostatic component.
$N_{\mathrm{wet}}, N_{\mathrm{liq}}$		Scaled-up refractivity for the wet and the liquid component respectively.
P	[hPa]	Air pressure.
P_0	[hPa]	Surface air pressure.
P_n^m		Schmidt semi-normalized associated Legendre functions of degree n and order m.
$P_{0,\mathrm{mid}}$	[hPa]	Mean estimate of surface air pressure.
P_{amp}	[hPa]	Amplitude of air pressure to model temporal variations.
P_{mean}	[hPa]	Mean value of air pressure.
R	[m]	Reference radius of the Earth.
R_d	$[\frac{\mathrm{J}}{\mathrm{kg \cdot K}}]$	Gas constant.
R_{sat}	[m]	Range distance from satellite to target.
T	[K]	Temperature.
T_0	[K]	Temperature above sea level.
T_a	[K]	Noise temperature.
T_m	[K]	Mean temperature of water vapour.
T_p	[s]	Pulse duration of the transmitted chirp.
T_u	[K]	Environmental temperature.
$T_{0,\mathrm{mid}}$	[K]	Mean estimate of surface temperature.
T_{amp}	[K]	Amplitude of temperature to model temporal variations.
T_{mean}	[K]	Mean value of temperature.
T_{p_iono}	[s]	Pulse duration of a chirp after passing the ionosphere.
U_{st}		Chirp amplitude.

V		Scalar potential.
W	[kg/m^3]	Liquid water content.
$X(t)$		Appendix A.2: Dummy variable for a harmonic propagation.
Y_L	[Tesla]	Longitudinal component of the Earth's magnetic field.
Y_T	[Tesla]	Transverse component of the Earth's magnetic field .
Y_c	[m]	Range to the target.
ΔA		Change in amplitude within chirp.
ΔR	[m]	Range distance between closest approach and the peak of range compressed TCR at azimuth position.
$\Delta Rg._{\text{JJ}}$	[m]	Differences in path delay between measured and vacuum propagation at the JJ station respectively.
$\Delta Rg._{\text{MI}}$	[m]	Differences in path delay between measured and vacuum propagation at the MI station respectively.
$\Delta\Phi_{\text{up\_down}}$	[rad]	Difference between up- and down-chirp phase distributions.
$\Delta\alpha$	[1/s^2]	Change in chirp rate.
$\Delta\phi$	[rad]	Phase advance caused by the ionosphere.
$\Delta\varphi$	[rad]	Phase difference of radar wave after passing through a dispersive medium.
Δk	[1/m]	Change in wave number of electromagnetic wave propagation trough a ionised medium when a longitudinal magnetic field is present compared to without magnetic field component.
Δs	[m]	Difference of propagation path between propagation in vacuum and a medium.
Δt	[s]	Minimal run time of a radar wave through a medium.
Δt_0	[s]	Minimal run time of a radar wave through a medium depending on the refractive index.
Δt_{group}	[s]	Time difference between vacuum propagation and the runtime of the envelope within a medium.
Δt_{iono}	[s]	Time delay of a radar wave traversing the ionosphere.
Δt_{phase}	[s]	Time difference between vacuum propagation and the runtime of a constant phase within a medium.
Δt_{d0}	[s]	Contribution to the frequency-dependent time delay of a chirped pulse.
$\Delta\Omega$	[rad]	Change in Faraday rotation within chirp.
Ω	[rad]	Polarisation rotation of an electromagnetic wave (Faraday rotation).
Ω_1	[rad]	Faraday rotation at start frequency.
Ω_2	[rad]	Faraday rotation at stop frequency.
$\Omega_{2-\text{way}}$	[rad]	Two-way Faraday rotation.
$\Omega_{\varnothing}$	[rad]	Mean Faraday rotation angle.
$\Psi_{\text{JJ,AVG}}$	[m]	Atmospheric path delays from average height model at the JJ station.
$\Psi_{\text{JJ,MI,RT}}$	[m]	Atmospheric path delays at the JJ, MI station or from the

		raytracer model.
$\Psi_{\mathrm{MI,AVG}}$	[m]	Atmospheric path delays from average height model at the MI station.
Ψ_{hyd}	[m]	Hydrostatic component of the tropospheric path delay of a radar wave.
Ψ_{iono}	[m]	Ionospheric path delay.
Ψ_{liq}	[m]	Liquid part of tropospheric path delay of a radar wave.
$\Psi_{\mathrm{tropo,sl}}$	[m]	Slant tropospheric path delay of a radar wave.
$\Psi_{\mathrm{tropo,zenith}}$	[m]	Tropospheric delay in zenith direction.
Ψ_{tropo}	[m]	Tropospheric path delay of a radar wave.
Ψ_{wet}	[m]	Wet component of tropospheric path delay of a radar wave.
α	[1/s^2]	Chirp rate.
α_{inc}	[rad]	Nominal incidence angle.
α_{iono}	[1/s^2]	Chirp rate modified by the ionosphere.
β	[K/m]	Temperature lapse rate.
β_{amp}	[K/m]	Amplitude of temperature lapse rate to model temporal variations.
β_{mean}	[K/m]	Mean value of temperature lapse rate.
β_{mid}	[K/m]	Mean estimate of temperature lapse rate.
δ_z	[rad]	Angle of refraction.
γ	[rad]	Off-nadir angle of the observation geometry.
λ		Chapter 1.3.4 and Chapter 2: Rate of decrease of water vapour.
λ	[m]	Wavelength of the radar wave.
$\lambda_{0,\mathrm{mid}}$		Mean estimate of water vapour rate of decrease.
λ_{amp}		Amplitude of rate of decrease of water vapour to model temporal variations.
λ_{mean}		Mean value of rate of decrease of water vapour.
$\mathbf{N}$		Additive noise matrix.
$\mathbf{R_F}$	[rad]	One-way Faraday rotation matrix.
$\mathbf{R}$		Receive distorsion matrix.
$\mathbf{S}$		Scattering matrix.
$\mathbf{T}$		Transmit distortion matrix.
μ_0	$[\frac{\mathrm{V\cdot s}}{\mathrm{Am}}]$	Magnetic constant.
μ_r	$[\frac{\mathrm{m\cdot kg}}{\mathrm{A^2 s^2}}]$	Relative permeability.
ν	[1/s]	Electron collision frequency.
ω	[rad/s]	Angular frequency of a radar wave.
ω_L	[rad/s]	Longitudinal component of the angular gyrofrequency of the magnetic field.
ω_T	[rad/s]	Transverse component of the angular gyrofrequency of the magnetic field.
ω_N	[rad/s]	Angular plasma frequency.
ϕ	[°]	Latitude.

ϕ_r	[rad]	Phase dispersion.
ϕ_{ph}	[s]	Two-way phase advance.
ψ	[°]	Longitude.
ρ	[kg/m^3]	Air density.
ρ_{el}	[C/m]	Free charge density.
σ_Ω		Standard deviation of mean extracted TEC.
σ_Ω		Standard deviation.
DOY		Day of year.
QPE	[rad]	Quadratic phase error.
QPE$_{\mathrm{peak}}$	[rad]	Quadratic phase error at the peak of the range compressed signal.
TEC	[TECU]	Total electron content.
TEC$_0$	[TECU]	TEC along the line of sight (vacuum conditions).
TEC$_m$	[TECU]	TEC along the propagation path in a medium including ray bending effects.
VTEC	[TECU]	Vertical total electron content.
θ	[°]	Colatitude.
ε_0	$[\frac{\mathrm{A^2s^4}}{\mathrm{m^3kg}}]$	Electric permittivity.
ε_r	$[\frac{\mathrm{As}}{\mathrm{Vm}}]$	Relative permittivity.
ε_{0w}	$[\frac{\mathrm{A^2s^4}}{\mathrm{m^3kg}}]$	Permittivity of water.
$\varnothing$TEC	[TECU]	Mean extracted TEC.
$\varnothing\Delta\Psi_{\mathrm{AVG}}$	[m]	Mean values of path delay differences between the JJ and MI station from the average height model.
$\varnothing\Delta\Psi_{\mathrm{HM}}$	[m]	Mean values of path delay differences between the JJ and MI station from the height-dependent model.
$\varnothing\Delta\Psi_{\mathrm{RT}}$	[m]	Mean values of path delay differences between the JJ and MI station from the ray tracer model.
$\varnothing\Psi_{\mathrm{AVG,iono}}$	[m]	Average one-way ionospheric path delays provided by the TSX annotations.
$\varnothing\Psi_{\mathrm{AVG}}$	[m]	Average scene height.
$\varnothing\Psi_{\mathrm{Meas,iono}}$	[m]	Average one-way ionospheric path delays from measurements.
φ	[rad]	Phase of an electromagnetic wave.
$\varphi_{\mathrm{start}}, \varphi_{\mathrm{stop}}$	[rad]	Phase of an electromagnetic wave before entering and after leaving a dispersive medium.
$\vec{B}$	[Tesla]	Magnetic flux density vector.
$\vec{D}$	[C/m^2]	Electric displacement.
$\vec{E}$	[V/m]	Electric field vector.
$\vec{H}$	[A/m]	Magnetic field vector.
$\vec{J}$	[Tesla]	Electric current density vector.
$\vec{P}$		Polarisation vector.
ξ'		Dummy variable for seasonal estimate of the mean atmospheric parameters P, T, e, β, λ.

ξ_{amp}		Dummy variable for the amplitude of temporal variations of the mean atmospheric parameters P, T, e, β, λ.
ξ_{mean}		Dummy variable for the mean atmospheric parameters P, T, e, β, λ.
c	[m/s]	Speed of light.
c_0	[m/s]	Speed of light in vacuum.
e	[hPa]	Water vapour pressure.
e_0	[hPa]	Water vapour pressure above sea level.
$e_{0,\mathrm{mid}}$	[hPa]	Mean estimate of surface water vapour pressure.
e_{amp}	[hPa]	Amplitude of water vapour pressure to model temporal variations.
e_{mean}	[hPa]	Mean value of water vapour pressure.
e_{el}	[C]	Charge of an electron.
f	[1/s]	Signal frequency.
f_0	[1/s]	Half chirp bandwidth.
f_N	[1/s]	Plasma frequency.
f_c	[1/s]	Center frequency or carrier frequency.
f_r	[1/s]	Range frequency.
f_s	[1/s]	Sampling rate.
f_{start}	[1/s]	Starting frequency of a chirp.
f_{stop}	[1/s]	Stop frequency of a chirp.
g	[m/s^2]	Average acceleration due to Earth gravity.
g_m	[m/s^2]	Acceleration due to local gravity.
g_n^m		Field coefficient to model the magnetic field.
h	[m]	Chapter 3.2.2 and Chapter 4.2.1: Propagation path.
h	[m]	Height.
h_0	[m]	Height of the point of interest.
h_i	[m]	Lower boundary height of the i-th atmospheric layer.
h_n	[m]	Integration height.
h_n^m		Field coefficient to model the magnetic field.
h_s	[m]	Scale height.
k	[1/m]	Wave number of an electromagnetic wave.
k^+	[1/m]	Wave number of circularly rotating electromagnetic wave in positive direction.
k^-	[1/m]	Wave number of circularly rotating electromagnetic wave in negative direction.
k_1, k_2'	[K/hPa]	Refractive constants of the troposphere.
k_3	[K^2/hPa]	Refractive constant of the troposphere.
k_n		Refraction coefficient.
$k_\circ$	[1/m]	Wave number in the ionosphere without the presence of a magnetic field.
m_e	[kg]	Electron mass.
n		Chapter 2.3.1: Number of layers.

n		Chapter 3.3.1: Number of chirp samples.
n		Refractive index of an atmospheric layer.
n_{group}		Group refractive index.
n_{hyd}		Hydrostatic component of the refractive index.
n_{phase}		Phase refractive index.
n_{tropo}		Refractive index of the troposphere.
n_{wet}		Wet component of the refractive index.
n_{liq}		Liquid component of the refractive index.
$p(t)$		Synthetic chirp used for range compression.
p_d	[hPa]	Dry air pressure.
p_f		Received signal after removing the Doppler frequency.
p_w	[hPa]	Partial water vapour pressure.
p_{liq}	[kg/m^3]	Density of liquid water.
p_{shifted}		Range compressed pulse after RMC.
r	[m]	Distance from the center of the Earth.
s		Propagation path of a radar wave.
$s(t)$		Received chirp.
s_0		Propagation path of a radar wave under vacuum conditions.
$s_0(t)$		Chirped pulse form.
s_M		Range compressed return echo in time domain.
s_m		Propagation path of a radar wave within a medium.
s_r, s_t		Pulse form of the received and transmitted chirp.
s_{FR}		Received chirp including FR- and path delay effects.
s_{iono}		Received chirp modified by the ionosphere.
t	[s]	Time.
t_{group}	[s]	Runtime of the envelope of a radar pulse.
t_{phase}	[s]	Runtime of a constant phase within a radar pulse.
$t_{\text{shift\_max}}$	[s]	Frequency dependent time delay of the wave end of a down-chirped pulse caused by the ionosphere.
$t_{\text{shift\_min\_d}}$	[s]	Pulse delay of down-chirp front passing the ionosphere.
$t_{\text{shift\_min\_u}}$	[s]	Pulse delay of up-chirp front passing the ionosphere.
$t_{\text{shift\_min}}$	[s]	Frequency dependent time delay of the wave front of a down-chirped pulse caused by the ionosphere.
t_{vacuum}	[s]	Runtime of a radar pulse under vacuum conditions.
t_{d0}	[s]	Time vector depending on the sensor's sampling rate and the range to the target.
v	[m/s]	Propagation velocity.
v_m	[m/s]	Propagation velocity of a radar wave within a medium.
v_{front}	[m/s]	Velocity of a wave front.
v_{group}	[m/s]	Velocity of the envelope of a radar pulse.
v_{phase}	[m/s]	Velocity of a constant phase within a radar wave.
z	[rad]	Zenith angle.

Curriculum Vitae

Michael JEHLE
*11.08.1973 in Waldshut, Germany
Remote Sensing Laboratories
Geographisches Institut
Winterthurerstr. 190
University of Zürich
Zürich, CH-8057

Phone: +41 44 635 6516
Fax: +41 44 635 6842
`michael.jehle@geo.uzh.ch`
`http://www.geo.uzh.ch/~mjehle`

Education

1984-1993	High school at Hochrhein - Gymnasium in Waldshut, Abitur in May 1993
1993-1995	Alternative national service at the red cross in St. Blasien
October 1995	Start of studies in electrical engineering at the Technical University in Karlsruhe
24. March 1998	Vordiplom (pre-diploma)
25. March 2002	Diploma in electrical engineering and information technology Diploma thesis on the "Development of a radar-based softwaretool for the estimation of dynamical machine parameters", mark 1.0
Apr. 2004 - Oct. 2009 (Expected)	Ph.D. candidate, University of Zürich, Institute of Geography

Work Experience

September 2003 – Present	University of Zürich, Dept. of Geography (Zürich, Switzerland) Worked with Prof. K.I. Itten, Remote Sensing Laboratories. Estimation of tropospheric path delays on SAR systems. Influence of ionospheric effects on radar signal propagation. Evaluation, calibration and development of techniques and methods for the correction of atmospheric effects.
October 2002 – June 2003	Klinikum für Sportorthopädie und Sporttraumatologie, Albert - Ludwigs University (Freiburg, Germany) Worked with Prof. Meyer, section biomechanics. Development of algorithms for the estimation of biometric data.
March 2002 – Sept. 2002	Institute for Very High Frequency Technology and Electronics at the University of Karlsruhe (Karlsruhe, Germany) Worked with Prof. Wiesbeck, IHE. Project for the development of a high frequency radar sensor for short distance measurements.
June 2000 – March 2001	Institute for Very High Frequency Technology and Electronics at the University of Karlsruhe (Karlsruhe, Germany) Worked with Prof. Wiesbeck, IHE. Development, design and measurement of patch antennas. Development of highly efficient algorithms.

Skills

Languages	German, English, French
Computing	MATLAB, C++, FORTRAN, LaTeX, Unix, Visual Studio, MS Office

Scientific Communications

- **Peer reviewed journals**

  Jehle, M., Frey, O., Small, D., & Meier, E. (2009). Measurement of Ionospheric TEC in Spaceborne SAR Data, TGRS, (under review)

Schubert, A., Jehle, M., Small, D., & Meier, E. (2009). Absolute Geolocation Accuracy of TerraSAR-X High-Resolution Products, TGRS, (accepted)

Jehle, M., Perler, D., Small, D., Schubert, A., & Meier, E. (2008). Estimation of Atmospheric Path Delays in TerraSAR-X Data using Models vs. Measurements, Sensors, 8(12), 8479-8491. (published)

Jehle, M., Rüegg, M., Zuberbühler, L., Small, D., & Meier, E. (2009). Measurement of Ionospheric Faraday Rotation in Simulated and Real Spaceborne SAR Data, TGRS, 47(5), 1512-1523. (published)

- **Peer reviewed conference contribution**

  Jehle, M., Rüegg, M., Small, D., Meier, E., & Nüesch, D. (2005). Estimation of Ionospheric TEC and Faraday Rotation for L-Band SAR, Proc. of SPIE, 5979, 2005, 252-260. (published)

- **Conference contributions**

  Schubert, A., Jehle, M., Small, D., & Meier E. (2008). Geometric Validation of TerraSAR-X High-resolution Products, Proc. of TerraSAR-X Science Team Meeting, Oberpfaffenhofen, Germany, Nov. 2008. 6p. (published)

  Small, D., Jehle, M., Schubert, A., & Meier, E. (2008). Accurate Geometric Correction for Normalisation of PALSAR Radiometry, Proc. of the ALOS 2008 Symposium, Rhodes, Greece, Nov. 3-7, 2008. 7p. (published)

  Nicoll, J., Meyer, F., & Jehle, M. (2007). Prediction and Detection of Faraday Rotation in ALOS PALSAR Data, in Proc. IGARSS, Barcelona, Spain, Jul. 2007, 5210-5213. (published)

  Pasquali, P., Monti Guarnieri, A., D'Aria, D., Costa, L., Small, D., Jehle, M., & Rosich, B., (2007). ALOS PALSAR verification processor, in ENVISAT Symposium 2007, (Montreux, Switzerland) 23-27 Apr, 2007, 1-6. (published)

  Nicoll, J., & Jehle, M. (2006). Impact of Faraday rotation on L-band SAR image quality, CEOS 2006, 3-6 Oct., Edinburgh, Scotland (contribution to presentation)

  Jehle, M., Small D., & Meier E. (2006). Comparison of Different TEC Map Estimation Methods, Proc. of 13th Australasian Remote Sensing and Photogrammetry Conference ARSPC, Nov. 2006, 6p. (published)

  Jehle M., Small D., Meier E., & Nüesch D. (2005). Generation of high resolution TEC maps with L-band Synthetic-Aperture Radar, Ionospheric Effects Symposium, Alexandria, Virginia, USA, 3.-5. May 2005. (poster)

  Small, D., Jehle, M., Meier, E., & Nüesch, D. (2004). Radiometric Terrain Correction Incorporating Local Antenna Gain, Proc. of EUSAR 2004, Ulm, Germany, May 25-27, 2004, 929-932. (published)

Jehle, M., Small, D., Meier, E., & Nüesch, D. (2004]). Improved Knowledge of SAR Geometry through Atmospheric Modelling, Proc. of EUSAR 2004, Ulm, Germany, May 25-27, 2004, 909-911. (published)

- **Other communications**

  Jehle, M., Small, D., Schubert, A., & Meier, E. (2008). Geometric Validation of TerraSAR-X High-Resolution Products, Remote Sens. Labs., Univ. Zurich, Zurich, Switzerland, International Foundation HFSJG Activity Report 2008, December 2008, 6p.

  Jehle, M. (2007) ALOS PALSAR Verification Processor Detailed Processing Model (DPM) of the Atmospheric Modelling Module, Remote Sens. Labs., Univ. Zurich, Zurich, Switzerland, Technical Note, September 2007, 24p.

  Jehle, M., Magnard, Ch., & Small, D. (2007). ALOS PALSAR Verification Processor Detail Processing Model (DPM) of the ALOS Precise Orbit Interface Module, Remote Sens. Labs., Univ. Zurich, Zurich, Switzerland, Technical Note, September 2007, 12p.

  Jehle, M. (2007). ALOS PALSAR Verification Processor Software User Manual and Interface Control Document for the Atmospheric Modelling Module, Remote Sens. Labs., Univ. Zurich, Zurich, Switzerland, Technical Note, October 2007, 15p.

  Jehle, M., Rüegg, M., Small, D., & Meier, E. (2007). SAR data for TEC and Faraday rotation, Remote Sens. Labs., Univ. Zurich, Zurich, Switzerland, Final Report, Contract No.20046/06/NL/CO, May 2007, 48p.

  Jehle, M., Zuberbühler, L., Small, D., & Meier, E. (2007). Comparison of estimated Faraday rotation using total electron content maps and the IGRF10 model with values derived from ALOS PALSAR Quad-Pol data, Remote Sens. Labs., Univ. Zurich, Zurich, Switzerland, Technical Note, March 2007, 13p.

  Jehle, M., Small, D., & Meier, E. (2006). Comparison of TEC maps derived from simulations and a GNSS network, Technical Note, Remote Sens. Labs., Univ. Zurich, Zurich, Switzerland, June 2006, 20p.

  Jehle, M. (2005). Einfluss der Atmosphäre auf SAR Daten im C-, X- und L-Band, SAR Signaturen - Jahresbericht 2004/2005, Remote Sens. Labs., Univ. Zurich, Zurich, Switzerland, June 2005, 16p.

  Jehle, M. (2005). Bestimmung des Elektronengehalts (TEC) in der Ionosphäre anhand breitbandiger SAR Daten, Technical Note, Remote Sens. Labs., Univ. Zurich, Zurich, Switzerland, January 2005, 26p.

  Jehle, M., Meier, E., & Nüesch, D. (2004). Resolution-dependent height accuracy of digital terrain models, Technical Note, TX-PGS-TN-3017, Remote Sens. Labs., Univ. Zurich, Zurich, Switzerland, May 2004, 35p.

Jehle, M., Rüegg, M., Small, D., & Meier, E. (2004). Estimation and Correction of Atmospheric Path Delay in Radar Signal Propagation, Remote Sens. Labs., Univ. Zurich, Zurich, Switzerland, Technical Note, TX-PGS-TN-3016, February 2004, 41p.